UNIVERSITÉ DU LUXEMBOURG

PhD-FSTM-2025-083

The Faculty of Science, Technology and Medicine

DISSERTATION

Presented on 25/08/2025 in Esch-sur-Alzette

to obtain the degree of

DOCTEUR DE L'UNIVERSITÉ DU LUXEMBOURG EN SCIENCES DE L'INGÉNIEUR

by

SONA SALEHIAN GHAMSARI

Born on September 13th 1993 in Kashan (Iran)

BRIDGING REMOTE SENSING AND HYDROGEOLOGY: STOCHASTIC MODELING OF ANISOTROPIC HYDRAULIC CONDUCTIVITY FOR AQUIFER CHARACTERIZATION USING INSAR

Dissertation defence committee

Dr. Jack S. Hale, Dissertation Supervisor

Research Scientist, University of Luxembourg

Prof. Roberta Boni, Member

Professor, Istituto Universitario di Studi Superiori

Prof. Arash Lavasan, Chairman

Associate Professor, University of Luxembourg

Dr. Amal Alghamdi, Member

Founder and Consultant, Impact Alpha

Dr. Patrick Matgen, Member

Group Leader, Luxembourg Institute of Science and Technology (LIST)

Prof. Tonie van Dam, Expert

Professor, University of Utah

Declaration

I hereby declare that except where specific reference is made to the work of others, the contents of this dissertation are original and have not been submitted in whole or in part for consideration for any other degree or qualification in this, or any other university. This dissertation is my own work and contains nothing which is the outcome of work done in collaboration with others, except as specified in the text and acknowledgements.

Sona Salehian Ghamsari

Acknowledgements

I would like to express my deepest gratitude to my supervisor, Dr. Jack S. Hale, for his daily guidance and for teaching me invaluable skills throughout my PhD journey. His support, patience, and insights were instrumental in ensuring my success and making this experience both enriching and fulfilling.

I am also sincerely grateful to Prof. Tonie Van Dam for providing me with this research opportunity and for initiating the idea behind this fascinating research topic.

A special thanks to Dr. Patrick Matgen, a member of my CET, for our stimulating discussions. I would also like to thank Prof. Andreas Zilian for his role as the coordinator of the Doctoral Training Unit (DTU) on Data-driven Computational Modelling and Applications (DRIVEN), of which I am proud to be a part.

I am immensely thankful to the FNR-Luxembourg National Research Fund for funding my research under the PRIDE program (PRIDE17/12252781), which made this work possible.

I would also like to extend my appreciation to Natascha, Hamidreza, Guendalina, Damian, Majid, Arnaud, Henry, Sina, Parisa, and Andrey for their friendship, collaboration, and support throughout this journey. Their encouragement and discussions have enriched both my research and my experience as a PhD student.

I am profoundly grateful to my parents, Mohammadreza Salehian Ghamsari and Fatemeh Gilasi, and my sister, Soha Salehian Ghamsari, for their unwavering love, patience, and support.

Last, and above all, thanks to my husband, Amin Khalaji. His belief in me has been my greatest motivation, and I could not have achieved this milestone without him. He was by my side all along in bad and good times. He is the most kind-hearted, caring, loving, and reliable partner.

Thank you all.

Sona Salehian Ghamsari,

Belval, 24 06 2025

Abstract

Managing groundwater resources effectively and sustainably amid growing global demand is a challenging task that requires high-accuracy subsurface models. In many aquifers, preferential flow features such as cracks and fractures introduce anisotropy. This anisotropy can be modeled by incorporating an anisotropic hydraulic conductivity (AHC) tensor into the equations of poroelasticity. This work aims to investigate the potential of interferometric synthetic aperture radar (InSAR) displacement data for inferring information about AHC in an aquifer.

To achieve this, we develop a three-dimensional poroelastic finite element method (FEM) with AHC, replicating key characteristics of the Anderson Junction aquifer in southwestern Utah. Our model implements the essential features of the 1994 Anderson Junction aquifer test, assuming a 24 to 1 hydraulic conductivity ratio along the principal axes, previously estimated using traditional well observation techniques (V. M. Heilweil & Hsieh, 2006).

The results of our FEM poroelastic model demonstrate that anisotropy in the hydraulic conductivity field induces an elliptical surface displacement pattern, which can be detected using InSAR data. However, our simulations indicate that the surface displacement resulting from the original Anderson Junction aquifer test is small to be captured by InSAR. To address this limitation, we propose hypothetical pumping test designs that maximize the utility of InSAR data in characterizing fractured aquifers.

Next, we construct a stochastic prior model of the AHC tensor that respects its symmetry and positive definiteness. This is achieved using a Bayesian model with a mixture of circular von Mises distributions. Finally, we laid the groundwork for Bayesian inversion, and we successfully constructed a NumPyro model that incorporates a Firedrake model and a probabilistic model and derived the corresponding adjoint model.

Furthermore, our stochastic AHC model leverages spectral decomposition to independently encode magnitude and orientation. The results of propagating AHC uncertainty through our aquifer model underscore the critical influence of fracture alignment on aquifer responses, revealing that the model is more stochastically sensitive to directional variations in AHC than to changes in its magnitude.

In the final chapter, we validated the integration between the partial differential equation (PDE) model (Firedrake) and the probabilistic model (JAX/NumPyro) through the Taylor test, which confirmed the correctness of the posterior gradient. In parallel, we solved a non-probabilistic inverse problem using adjoint-based optimization to estimate the AHC tensor from synthetic pressure observations. The results demonstrate that the inverse framework accurately recovers the true AHC tensor, confirming the reliability of our PDE-constrained optimization approach and its potential for future Bayesian inference applications.

Contents

List of Figures

List of Tables

Glossary

AD automatic differentiation. 104, 105, 109, 112

AHC anisotropic hydraulic conductivity. iv, v, ix, xi, xiv, xv, xvi, xx, 2, 3, 4, 5, 7, 8, 10, 11, 12, 13, 20, 36, 37, 38, 39, 40, 59, 61, 62, 63, 70, 75, 76, 78, 79, 80, 81, 82, 83, 88, 89, 90, 93, 94, 95, 96, 97, 98, 99, 101, 103, 104, 105, 106, 107, 108, 109, 112, 113, 116, 117, 118, 119, 120, 121, 125, 126, 127, 128

AIC Akaike information criterion. 87

BC boundary condition. 27

CV cross-validation. 87

DAG directed acyclic graph. xv, 86, 106, 107, 108

DIC deviance information criteria. 87

ELPD expected log pointwise predictive density. xix, 91

FEM finite element method. iv, vii, xvi, 12, 17, 18, 19, 21, 57, 108, 125

GNSS global navigation satellite system. 48

GPS global positioning system. 1, 5, 7, 38, 75, 127

HMC Hamiltonian Monte Carlo. 87, 104

HPC high-performance computing. 94

i. i. d. independent and identically distributed. 85, 86, 89

IHC isotropy hydraulic conductivity. xiv, 8, 39, 59, 61, 62

InSAR interferometric synthetic aperture radar. iv, viii, xi, xv, 1, 3, 5, 7, 8, 9, 10, 11, 12, 36, 37, 38, 39, 40, 46, 48, 57, 63, 65, 66, 69, 70, 75, 76, 78, 79, 80, 81, 82, 83, 99, 101, 125, 126, 127

LOOCV Leave-one-out cross-validation. 10, 79, 87, 90

LOS line of sight. xi, xiv, xv, xvi, 3, 5, 6, 8, 10, 12, 13, 39, 40, 46, 48, 49, 63, 65, 66, 67, 68, 69, 70, 79, 80, 82, 89, 94, 96, 97, 98, 99, 100, 101, 126, 127

MCMC Markov Chain Monte Carlo. xvi, 3, 9, 10, 90, 108, 123, 128

ML machine learning. 104

MLE maximum likelihood estimation. 9, 78, 88

NUTS No-U-Turn Sampler. 87, 90, 101, 104

PDE partial differential equation. v, ix, 10, 12, 13, 14, 17, 27, 75, 103, 104, 105, 106, 107, 109, 111, 112, 113, 115, 117, 118, 119, 121, 123, 126, 128

PDF probability density function. 86, 93

PSIS Pareto-smoothed importance sampling. 10

SAR synthetic aperture radar. xi, 5, 6, 48, 49, 66, 69

SPD symmetric positive definite. xv, 10, 11, 13, 79, 80, 82, 113, 128

SVGD Stein variational gradient descent. 123

UFL unified form language. 104, 117

USGS US seological survey. 40

VI variational inference. 9, 10, 78

Chapter 1

Introduction

Groundwater supplies nearly half of the drinking and irrigation water. This vital resource is under increasing pressure due to population growth and human-driven climate change. Overexploitation poses a serious challenge to groundwater sustainability (Basu & Van Meter, 2014; Caretta et al., 2022)—years of excessive pumping can lower the water table (V. M. Heilweil & Hsieh, 2006; Burbey et al., 2006), leading to land subsidence (Galloway & Burbey, 2011). If left unchecked, this phenomenon can cause the ground to sink, roads and buildings to crack, and fissures to form, resulting in costly and irreversible damage.

To ensure the sustainable use of groundwater, we need to monitor and manage it effectively. This requires integrating multiple data sources—including geological, hydrological, and regional datasets—into comprehensive aquifer models. The more data we assimilate into the model, the better our predictions, enabling decision-makers to develop informed strategies for groundwater management (Singh, 2014; Amitrano et al., 2014).

Entering the PhD, I had a background in remote sensing. Under the co-supervision of Prof. Tonie van Dam and Dr. Jack S. Hale, I was inspired to explore scientific questions at the intersection of remote sensing, modeling, and inverse problems. Consequently, my PhD research builds toward the integration of remote sensing data, such as interferometric synthetic aperture radar (InSAR) and global positioning system (GPS), into aquifer models for the estimation of aquifer properties.

1.1 Bayesian inverse modeling of aquifer systems

Estimating subsurface properties, such as anisotropic hydraulic conductivity (AHC), is essential for understanding groundwater flow and associated deformation. Several methods are available for this purpose, including direct field measurements, geophysical surveys, and inverse modeling. Among these, inverse modeling offers a powerful mathematical framework for inferring unknown parameters by leveraging observed system responses—such as surface displacement derived from remote sensing data.

Several studies have applied inverse modeling techniques to estimate subsurface properties (Lochbühler et al., 2013; Hinnell et al., 2010; Oliver et al., 2008; Carrera et al., 2005). For instance, Hinnell et al. (2010) performed joint inversion of hydrological and geophysical data to enhance the estimation of hydraulic conductivity. Similarly, Oliver et al. (2008) estimated reservoir properties such as permeability and porosity using inverse modeling approaches, with an emphasis on Bayesian methods to effectively quantify uncertainty. As argued by Tarantola (2005), the Bayesian framework is particularly well-suited for solving inverse problems, as it systematically incorporates prior information, updates it through the likelihood function based on observed data, and yields a posterior distribution that represents uncertainty in the estimated parameters.

Bayesian theory provides a probabilistic framework for updating our knowledge or beliefs about a system in light of observed data. At the heart of this approach lies **Bayes' theorem**, which enables the combination of prior knowledge with new observation to infer the probability distribution of unknown parameters.

Bayes' theorem is mathematically defined as

$$P(\theta \mid \mathcal{D}) = \frac{P(\mathcal{D} \mid \theta)P(\theta)}{P(\mathcal{D})}, \tag{1.1}$$

where θ denotes the model parameters, $\mathcal{D}$ represents the observed data, $P(\theta)$ is the prior distribution reflecting our initial beliefs about the parameters, $P(\mathcal{D} \mid \theta)$ is the likelihood function indicating how likely the observed data are given the parameters, and $P(\theta \mid \mathcal{D})$ is the posterior distribution that captures updated beliefs after considering the data. The term $P(\mathcal{D})$ is the marginal likelihood or evidence, serving as a normalization constant.

Bayesian inference is especially useful for complex or ill-posed problems, such as those

involving uncertainty quantification or parameter estimation. In hydrogeology, for instance, Bayesian methods are recently used to estimate aquifer properties like hydraulic conductivity by incorporating both prior geological information and observational data such as surface displacements or groundwater levels (e.g., Alghamdi (2020); Iglesias et al. (2014); Fienen et al. (2004); Teixeira Parente et al. (2019)).

In a Bayesian inverse problem, the process begins with the development of a forward model—such as a poroelastic finite element model—that predicts surface deformation and pressure field for a given AHC tensor. To proceed with Bayesian inversion, a prior distribution is defined to encode geological or structural knowledge about AHC, and a likelihood function is formulated to quantify the agreement between the simulated and observed data.

By combining the prior and likelihood through Bayes' theorem Eq. (1.1), we obtain the posterior distribution, which represents updated knowledge of the parameters conditioned on the data. This posterior can be explored using computational methods such as Markov Chain Monte Carlo (MCMC), which provide a robust means of sampling from complex, high-dimensional distributions.

Although a full Bayesian inversion framework is not implemented in this work, several key steps toward such an approach have been achieved. First, we developed a large-scale poroelastic forward model to investigate the conditions under which InSAR observations provide meaningful information for inferring AHC. Second, we constructed a comprehensive hierarchical prior model for AHC, which enabled forward uncertainty propagation and analysis of line of sight (LOS) surface deformation. Third, a differentiable programming abstraction was introduced to couple the PDE model with the probabilistic model, paving the way for gradient-based optimization and Bayesian inference in a unified framework. Finally, as a proof of concept, we carried out a deterministic inversion in a 2D flow setting using well pressure data, demonstrating the feasibility of characterizing AHC.

1.2 Forward modeling

Various theoretical models exist to simulate this response, such as the aquitard drainage model, the poroelasticity model and the poroviscosity model (Guzy & Malinowska, 2020),

all relying on the fundamental relationships between groundwater head, flow direction, water pressure, and aquifer compaction. Aquitard drainage and poroelasticity models are two key approaches for analyzing aquifer compaction and surface subsidence due to groundwater pumping. These methods incorporate physical, hydrogeological, and geomechanical properties of the rock matrix, along with fluid flow dynamics, to better understand subsurface deformation (Guzy & Malinowska, 2020).

The aquitard drainage model was developed by Riley (Riley, 1970), who applied Terzaghi's (Karl Terzaghi, 1967) quantitative theory of one-dimensional vertical compaction. This model is grounded in conventional groundwater flow theory and incorporates two key consolidation principles: the effective stress principle and the relationship between hydraulic pressure, intergranular stress, and water flow within the rock matrix. While the aquitard drainage model has been widely used and is suitable for many hydrogeologic settings, more complex and realistic aquifer systems often require the use of numerical poroelasticity models for improved accuracy and representation of coupled flow-deformation processes (Helm, 1986; Harbaugh et al., 2000; Hoffmann et al., 2003; Harbaugh, 2005).

The poroelasticity theory, introduced by Biot (Biot, 1941), describes the interaction between groundwater flow, the porous rock matrix, and solid grains. It explains how changes in pore pressure and fluid content affect deformation and stress within the solid structure. We use aquifer pumping tests as groundwater discharge in the aquifer model. During the test, pumping induces a drop in pore pressure, leading to a three-dimensional deformation of the aquifer system.

1.3 Anisotropic hydraulic conductivity (AHC) in a fractured aquifer

AHC describes the variation in a material's ability to transmit water in different directions. Many aquifers exhibit anisotropic flow due to geological features such as fractures and faults. In fractured aquifers, fluid conductivity is typically higher along the direction of fractures (Berre et al., 2019). This anisotropy can be effectively modeled at the

macroscale by incorporating an AHC tensor into the poroelasticity equations.

At the macroscale, the AHC of a homogenized aquifer system is linked to the statistical properties of flow features at the microscale. Several factors influence AHC, including fracture orientation, length, spacing, hydraulic aperture, and the size and distribution of fracture apertures (Ren et al., 2015).

However, detailed information about fracture characteristics is often unavailable, and gathering such data is both costly and time-consuming. To address this, it is essential to account for AHC uncertainty in aquifer modeling. One of the simplest and most accessible sources of prior information on AHC is rose diagrams (V. Heilweil et al., 2000), which provide a statistical representation of fracture orientations.

1.4 Why InSAR?

InSAR is a powerful technique for measuring ground surface displacement. It offers wide-area coverage, cost-effectiveness, and frequent observations, making it an increasingly popular tool in hydrogeological studies (Galloway & Hoffmann, 2007; Guzy & Malinowska, 2020). The technique works by sending radar waves from the satellite to Earth's surface in the direction of LOS and measuring the backscattered signal. The side-looking geometry of synthetic aperture radar (SAR) imaging is shown in Fig. 1.1.

By comparing two radar images taken at different times, InSAR generates an interferogram that, through phase unwrapping and height computation from the phase difference, can detect even subtle changes in surface elevation with millimeter-level precision (Manunta et al., 2019; Duan et al., 2020).

Since groundwater flow influences surface height, InSAR can be used to track subsidence and uplift caused by changes in the water table (Gambolati & Teatini, 2015). This data can help estimate storage coefficients and hydraulic conductivity (Bonì et al., 2020; X. Hu et al., 2018; Bonì et al., 2016; Chaussard et al., 2014), determine the structural boundaries of aquifer systems (Chaussard et al., 2014; Haghighi & Motagh, 2019; X. Hu & Bürgmann, 2020), and monitor the temporal evolution of groundwater-induced surface displacement (Zhou et al., 2018; L. Guo et al., 2019; Bonì et al., 2017).

GPS also provides highly precise observations of surface displacements, comparable to

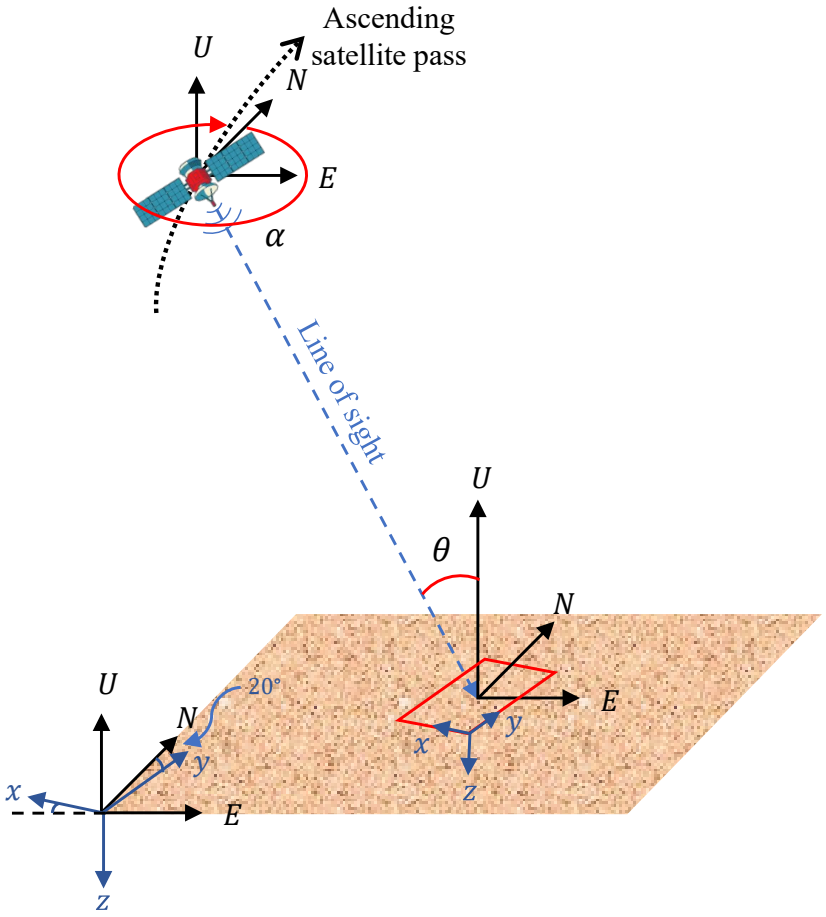

Figure 1.1: Geometry of SAR imaging, showcasing the side-looking acquisition geometry in the direction of the LOS.

InSAR in accuracy. Another key advantage of these geodetic techniques for groundwater monitoring is their ability to generate time-series data that tracks surface displacement over time. However, while GPS offers continuous time-series data with high temporal resolution, InSAR provides dense spatial coverage that would otherwise require an extensive network of GPS stations.

In our problem, analyzing these temporal changes provides valuable insights into how groundwater extraction influences land subsidence and aquifer behavior over time. Incorporating remote sensing time-series data into aquifer models is expected to enhance groundwater estimations, ultimately leading to better groundwater management strategies.

1.5 Literature gaps

The influence of AHC on aquifer behavior has long been recognized, beginning with the foundational work of Papadopulos (1965). He developed a method to determine hydraulic conductivity in homogeneous anisotropic aquifers by analyzing water table level change at a minimum of three observation wells placed around an aquifer pumping test. Later, V. M. Heilweil & Hsieh (2006) and Burbey (2006) show that AHC could be inferred using only two observation wells, provided they were aligned with the principal axes of anisotropy.

The role of AHC has also been explored in the context of geodesy. Burbey et al. (2006) and Burbey (2006) proposed that the elliptical vertical displacement patterns detected by GPS stations surrounding a pumping test in Nevada were a direct result of anisotropic fluid flow interacting with the aquifer formation layer. Numerical simulations conducted by Burbey (2006) using poroelasticity theory further supported this hypothesis, demonstrating that a AHC ratio of 3:1 produces surface deformation with a distinct elliptical shape. Burbey did not incorporate InSAR wide-area displacement data in his calibration process. Furthermore, his approach relied on a deterministic model and did not use probabilistic modeling frameworks.

The integration of remote sensing techniques into groundwater studies has further advanced this field. Galloway & Hoffmann (2007) demonstrated that InSAR data can

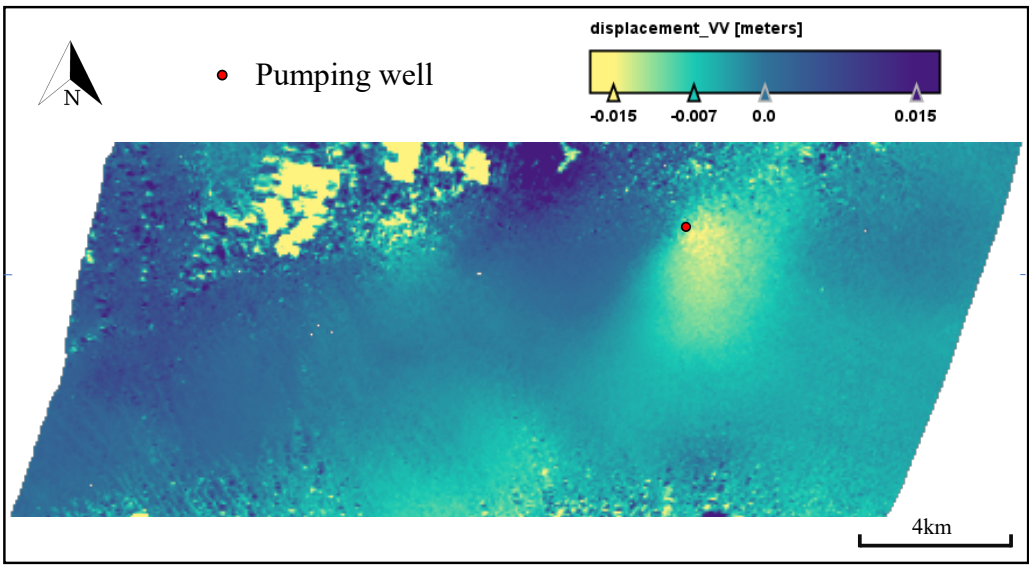

Figure 1.2: InSAR-observed LOS deformation between May 4, 2003 and October 26, 2003, during the Nevada aquifer pumping test performed by Burbey et al. (2006). This dataset was used by Alghamdi (2020) to estimate hydraulic conductivity within a Bayesian framework. The red dot shows the location of the pumping well. Water was pumped for 62 d at a rate of $0.189\,\mathrm{m^3\,s^{-1}}$. Note the distinctive elliptical subsidence bowl to the south east of the pumping well which was attributed to AHC in Burbey et al. (2006)

.

be used to calibrate numerical models of groundwater-induced deformation, while Galloway & Burbey (2011) provided a comprehensive review of remote sensing applications for subsidence monitoring. More recently, Hesse & Stadler (2014) introduced scalable computational methods to assimilate InSAR data into a poroelastic finite element model within a Bayesian framework, assuming spatially varying but isotropic hydraulic conductivity.

Building upon these developments, Alghamdi (2020); Alghamdi et al. (2020, 2021) applied InSAR data from the Nevada test site of Burbey et al. (2006) to a poroelastic model with spatially varying isotropy hydraulic conductivity (IHC). However, the original study by Burbey et al. (2006) indicated that the site's hydraulic behavior is likely to be highly anisotropic due to geological fracturing. This raises concerns that the isotropic model used in Alghamdi (2020) may be insufficient for fully capturing the site's anisotropic properties. Moreover, the elliptical surface deformation observed in InSAR data, shown in Fig. 1.2, can provide further evidence of anisotropic behavior, aligning with the conclusions of Burbey (2006).

Recent advancements in integrating aquifer hydraulic conductivity, surface displacement data, and inverse modeling have led to the development of scalable computational frameworks for inferring subsurface properties. While these studies (Hesse & Stadler, 2014; Alghamdi et al., 2020, 2021, 2024) have leveraged InSAR data for Bayesian inversion (Tarantola, 2005; Fernández-Martínez et al., 2013) using a log-Gaussian process prior model, they have primarily focused on estimating heterogeneous *isotropic* lateral hydraulic conductivity fields.

In Bayesian inference, the choice of prior significantly impacts the final posterior estimates, making it crucial that prior assumptions align with geological reality. However, when observations—such as geomechanical testing, remote sensing, and outcrop mapping—indicate anisotropy (Pollard & Fletcher, 2005), the isotropic prior used in (Alghamdi et al., 2020, 2021, 2024) may lead to misleading interpretations. In contrast, V. M. Heilweil & Hsieh (2006) used the Anderson Junction aquifer pumping test to identify flow direction by analyzing fracture outcrop data presented in a rose diagram (Sanderson & Peacock, 2020), leveraging the relationship between small-scale fractures and large-scale hydraulic anisotropy.

The increasing use of circular random variables in geosciences reflects the need to model directional data, such as fracture orientations (Adler & Thovert, 2013; Lark et al., 2014; Rad et al., 2022). These variables, constrained to the unit circle, require specialized statistical tools (Mardia & Jupp, 1999; Ley & Verdebout, 2018). At Anderson Junction, fracture orientations exhibit multimodal, which necessitate advanced models like von Mises mixture distributions, as first proposed by (Lark et al., 2014) in structural geology. This approach extends the earlier unimodal formulation of (Davis, 2002), providing a more robust representation of multimodal directional data. While V. M. Heilweil & Hsieh (2006) considered anisotropy in the fractured Anderson Junction aquifer, they did not capture the uncertainty or multimodal characteristics of fracture orientations.

Both Lark et al. (2014) and Taghia et al. (2014) used mixtures of von Mises distributions in their studies—focusing on geological structures and on signal processing and brain imaging, respectively. For posterior inference, Lark et al. (2014) employed maximum likelihood estimation (MLE), while Taghia et al. (2014) employed variational inference (VI) rather than MCMC. MLE estimates parameters by maximizing the likelihood without

incorporating prior information, which risks overfitting and poor uncertainty quantification. VI, while computationally efficient, may struggle with complex distributions (Blei et al., 2017a). In contrast, given enough time and samples, MCMC can explore complex and correlated distributions, though it is computationally expensive (Neal, 2012).

For model selection—where each method presents trade-offs in flexibility, complexity, and uncertainty estimation—Leave-one-out cross-validation (LOOCV)(Mao et al., 2014), particularly in its efficient Pareto-smoothed importance sampling (PSIS)-LOOCV form(Vehtari et al., 2015, 2017), offers a robust alternative focused on predictive performance.

The poroelastic partial differential equation (PDE) model governing groundwater flow and deformation requires an AHC tensor that is symmetric positive definite (SPD) (e.g. (Guilleminot & Soize, 2012; Soize, 2000; Schwartzman, 2006)) to ensure mathematical well-posedness (Aris, 2012). Because of this symmetry, the secondary principal direction is constrained to be orthogonal to the primary direction. Unlike Shivanand et al. (2024), who employed a unimodal SPD model, we require an extended multimodal SPD model. This extension allows for a more flexible and accurate representation of AHC in geological systems with complex directional behaviors.

1.6 Contributions

The main contributions of this thesis are summarized below.

1. We construct a three-dimensional poroelastic model Chapter 3 that explicitly incorporates AHC to analyze the relationship between surface displacement and groundwater extraction at Anderson Junction in southwestern Utah. Leveraging the proposed model, we compute InSAR LOS displacements, which are critical for calibrating theoretical predictions with remotely sensed observations (Alghamdi, 2020).

2. Our model shows an elliptical surface displacement pattern driven by the underlying anisotropy in the fluid problem. This finding shows InSAR data can serve as a viable tool for inferring AHC properties in aquifer systems by predicting surface displacements induced by controlled pumping scenarios.

3. Under the hypothesis of our model, the four-day pumping in the Anderson Junction test was insufficient to generate surface displacements detectable via InSAR, we conduct simulations under varied pumping rates, durations, and AHC ratios to identify conditions where using InSAR observations to infer information about AHC would be feasible. Additionally, we propose practical guidelines for designing future pumping tests within the constraints of InSAR acquisition.

4. To address the uncertainty in AHC, we introduce a stochastic model for the AHC tensor tailored to inverse problem using InSAR in Anderson Junction (V. M. Heilweil & Hsieh, 2006). Our central hypothesis is that InSAR measurements contain valuable information for characterizing AHC, and that incorporating this data into Bayesian inverse modeling can improve hydrological predictions in anisotropic aquifers like Anderson Junction.

5. We develop a Bayesian model designed to handle multimodal directional geological data. Extending the multimodal Bayesian circular framework of Taghia et al. (2014) for structural data, we calibrate our model against fracture outcrop data from Anderson Junction (V. M. Heilweil & Hsieh, 2006) to construct a probabilistic representation of the principal direction of the AHC tensor. Our approach uses a mixture of circular von Mises distributions with unknown parameters, weighted using a Dirichlet distribution (Bishop, 2006, Chapter 9).

6. We extend a flexible stochastic prior model for the AHC tensor that respects its inherent symmetry and positive definiteness. Our method for constructing a random AHC tensor proceeds as follows:

   (a) A Bayesian mixture model of circular von Mises distributions is fitted to fracture outcrop data to characterize the directional component of AHC.

   (b) A Bayesian model of two independent log-normal distributions is used to estimate hydraulic conductivity magnitudes in the principal directions.

   (c) These stochastic components are integrated into an extended multimodal symmetric positive definite (SPD) tensor model following the framework of Shivanand et al. (2024).

This flexibility allows us to define two conceptual states of belief about the study region. The resulting uncertainty in AHC is then propagated through a partial differential equation-based conceptual model of the test site. Our findings demonstrate that the proposed methodology provides a versatile approach for capturing the effects of uncertain AHC on surface displacements measurable by InSAR.

7. We developed a differentiable programming abstraction that bridges the Firedrake PDE solver and the JAX-based probabilistic programming library NumPyro, enabling gradient-based optimization and Bayesian inference within a unified framework. This coupling was made possible through custom integration using `jax.pure_callback()` and `jax.custom_jvp`, allowing gradients to propagate correctly through both PDE solvers and probabilistic models. We validated this integration using the Taylor test to confirm the correctness of gradient computations within the coupled workflow.

1.7 Thesis outline

In Chapter 2, we revisit the three-field formulation of Biot's poroelasticity theory, which serves as the foundation for constructing a conceptual model of the Anderson Junction pumping test in Chapter 3. We provide a detailed description of our proposed model, which explicitly incorporates the AHC tensor. Additionally, we discuss the principles of poroelasticity, the finite element method (FEM), and the discretization process in both space and time. Further explanation on boundary conditions and mesh generation are also presented to ensure a clear understanding of the model setup.

Chapter 3 presents a comprehensive version of the Anderson Junction conceptual model, designed to compute surface displacements based on known pumping rates and evaluate the potential of InSAR data for inferring AHC in aquifer systems. We provide an overview of the Anderson Junction study area and the aquifer test. We also present an introduction to the InSAR technique, followed by details of the transformation of three-dimensional deformations into InSAR LOS observations. Additionally, we describe our proposed model in depth and discuss the outcomes of our simulations.

In Chapter 4, we develop a flexible stochastic prior model for the AHC tensor that

preserves its inherent symmetry and positive definiteness, making it a suitable prior for Bayesian assimilation. We introduce a Bayesian model that employs a mixture of circular von Mises distributions to capture the rotation angle from fracture outcrop data. To represent the magnitude of the hydraulic conductivity tensor, we present a Bayesian model consisting of two independent log-normal distributions to incorporate existing estimates of hydraulic conductivity in the principal directions. These stochastic models are then integrated into a version of the SPD model to generate random AHC tensors. Finally, we calculate summary statistics of the LOS surface displacement using Monte Carlo simulations and present the results, along with a summary of our research findings.

In Chapter 5, we integrate a PDE model with a probabilistic model, marking a critical step toward fully automated Bayesian inversion. We develop a differentiable programming interface that couples the Firedrake PDE solver with the NumPyro probabilistic programming library, enabling gradient-based inference through custom JAX-compatible callbacks. The correctness of the posterior gradient is verified using the Taylor test. In addition to the probabilistic framework, we formulate and solve a non-probabilistic inverse problem using adjoint-based optimization to estimate AHC tensors. Synthetic pressure observations are generated via a physically consistent method in Firedrake, and the estimated AHC tensor closely reproduces these observations. Finally, we discuss how this foundational framework supports future extensions toward full Bayesian inversion and more complex multiphysics models.

Finally, Chapter 6 outlines the main conclusions and limitations of this thesis and explores potential avenues for future research.

1.8 Research dissemination

My project has led to the following scientific contributions.

Scientific writings

Peer-reviewed journal article:

- Sona Salehian Ghamsari, Tonie van Dam, Jack S. Hale (2025). "Can the anisotropic hydraulic conductivity of an aquifer be determined using surface displacement data? A case study". *Applied Computing and Geosciences*, Volume 26, June 2025, 100242. 10.1016/j.acags.2025.100242

Submitted pre-prints:

- Sona Salehian Ghamsari, Tonie van Dam, Jack S. Hale. "A random model of anisotropic hydraulic conductivity tailored to the InSAR-based analysis of aquifers". In: (2025). https://hdl.handle.net/10993/65440

In preparation:

- Sona Salehian Ghamsari, Tonie van Dam, Jack S. Hale. "Automatic differentiation of models involving machine learning and PDE components".

Conferences

Presentations as speaker:

- Sona Salehian Ghamsari, Tonie van Dam, Jack S. Hale. (2025) "Towards assimilating inSAR data into a model of a highly anisotropic aquifer system". International Symposium on Computational Sensing, Luxembourg, Luxembourg. https://hdl.handle.net/10993/65254

- Sona Salehian Ghamsari, Guendalina Palmirotta, Tonie van Dam, Jack S. Hale. (2024). "Using random circular models to simulate stochastic anisotropic flow in aquifer systems with FEniCSx". FEniCS Conference 2024, Oslo, Norway. https://hdl.handle.net/10993/62049

- Sona Salehian Ghamsari, Tonie van Dam, Jack S. Hale. (2023). "Towards assimilating SAR data into an anisotropic model of an underground aquifer". The European Geosciences Union (EGU) General Assembly 2023, Vienna, Austria. https://hdl.handle.net/10993/54446

- Sona Salehian Ghamsari. (2022), “InSAR for climate change”, Doctoral Programme in Computational Sciences (DPCS) Workshop, Belval, Luxembourg. https://hdl.handle.net/10993/54536

Poster:

- Sona Salehian Ghamsari, Guendalina Palmirotta, Tonie van Dam, Jack S. Hale. (2024). “Using random circular models in aquifer flow simulation”. DPCSS PhD Day. https://hdl.handle.net/10993/62053

Outreach:

- Sona Salehian Ghamsari. (2024). "Engineering Innovations - Sona Salehian Ghamsari". Filming an interview with Dr.Shini to present my research to public audiences. University of Luxembourg, Luxembourg. https://www.youtube.com/watch?v=Gqd5qMfSodc

Open science

- Sona Salehian Ghamsari and Jack S. Hale. Supplementary material for “Can the anisotropic hydraulic conductivity of an aquifer be determined using surface displacement data? A case study”. 2025. 10.5281/zenodo.10890121
- Sona Salehian Ghamsari and Jack S. Hale. Supplementary material for “A random model of anisotropic hydraulic conductivity tailored to the InSAR-based analysis of aquifers”. 2025. 10.5281/zenodo.14170026

Chapter 2

Finite element method of three-field formulation of Biot's poroelasticity theory

The content of this chapter is based on part of the following paper.

Salehian Ghamsari, S., van Dam, T., and Hale, J. S. (2025). Can the anisotropic hydraulic conductivity of an aquifer be determined using surface displacement data? A case study. *Applied Computing and Geosciences*, Volume 26, June 2025, 100242. 10.1016/j.acags.2025.100242

Authorship statement

Sona Salehian Ghamsari: Data curation, Methodology, Software, Formal analysis, Investigation, Writing - Original Draft, Validation, Visualization. Tonie van Dam: Conceptualization, Writing - Review & Editing, Funding acquisition, Supervision. Jack S. Hale: Conceptualization, Methodology, Software, Investigation, Writing - Review & Editing, Funding acquisition, Project administration, Supervision.

In this chapter, we present the forward model and the scientific foundations necessary for understanding it. As outlined in the previous chapter, we adopt a finite element poroelasticity model to simulate the aquifer system. We begin by introducing the theory of poroelasticity and Biot's equations. We then describe the FEM as a numerical tool for solving the governing PDEs and detail the discretization of Biot's equations within the

FEM framework. Finally, we validate our implementation using the classical Terzaghi consolidation problem to demonstrate the model's accuracy and reliability.

2.1 Poroelasticity theory

Poroelasticity describes the coupled behavior of fluid flow and mechanical deformation in porous materials, such as soils, aquifers, and biological tissues. It combines fluid mechanics (Darcy's law) and solid mechanics (elasticity theory) to explain how a porous medium deforms in response to fluid pressure changes. When fluid moves through the pores, it exerts pressure on the solid framework and pushes outward or pulls inward, causing the solid skeleton to expand or shrink.

When pressure is applied or removed, the system does not instantly reach equilibrium. Fluid moves slowly through the pores, causing delayed deformation (time-dependent response). This is why land subsidence due to groundwater pumping may continue even after pumping stops.

Poroelasticity theory has numerous real-world applications in geosciences. Extracting groundwater lowers pore pressure, which leads to the compaction of aquifers and land subsidence, as observed in locations such as Mexico City, California, and Shanghai. Similarly, storing water in reservoirs increases pressure, causing deformation of the underlying rock, as discussed in studies like Gupta (2002). The removal of hydrocarbons also reduces pressure, which can result in subsidence or even induce seismic activity, as shown in Huang & Ghassemi (2015).

2.2 Biot's poroelasticity model

In this section, we recall a three-field formulation of Biot's poroelasticity theory that we will use to construct a conceptual model of the Anderson Junction pumping test in Section 3.4.

In the three-field formulation of poroelasticity, the coupled behavior of a saturated porous medium is governed by three equations: fluid mass conservation, mechanical equilibrium, and Darcy's law. The mass conservation equation accounts for changes in fluid

content due to both pore pressure variation and deformation of the solid skeleton, ensuring that fluid is neither created nor lost. The equilibrium equation enforces mechanical balance by relating the total stress—which includes contributions from both elastic deformation and pore pressure—to external body forces. Finally, Darcy's law links fluid flux to the pressure gradient, describing how pore fluid moves through the medium under pressure-driven flow. Together, these equations model the complex interplay between fluid movement and solid deformation within the poroelastic framework.

We use the following three-field formulation of Biot's poroelasticity theory Ferronato et al. (2010); Alghamdi (2020). To discretize the following equations, we use a three-field finite element formulation adapted from Ferronato et al. (2010). We leave details of the FEM discretization to Section 2.3. The full solver is given as supplementary material in Salehian Ghamsari & Hale (2025). Precise specification of the domains and their boundaries, boundary and initial conditions and parameter values for the Anderson Junction site will be given in Section 3.4.

Given a domain $\Omega \subset \mathbb{R}^3$ with boundary Γ and outward-pointing normal n, find the fluid-pore pressure $p : \Omega \times (0, T] \to \mathbb{R}$, deformation $u : \Omega \times (0, T] \to \mathbb{R}^3$ and fluid flux $q : \Omega \times (0, T] \to \mathbb{R}^3$ such that

$$(S_\varepsilon p + \alpha \nabla \cdot u)_t + \nabla \cdot q = f_p \text{ on } \Omega \times (0, T], \tag{2.1a}$$

$$-\nabla \cdot \bar{\sigma}(u, p) = f_u \text{ on } \Omega \times (0, T], \tag{2.1b}$$

$$q + k\nabla p = 0 \text{ on } \Omega \times (0, T], \tag{2.1c}$$

with notations and units summarized in Table 2.1, plus boundary conditions

$$u = u_d \text{ on } \Gamma_u^d \times (0, T], \tag{2.1d}$$

$$\bar{\sigma} \cdot n = g_u \text{ on } \Gamma_u^n \times (0, T], \tag{2.1e}$$

$$p = p_d \text{ on } \Gamma_p^d \times (0, T], \tag{2.1f}$$

$$q \cdot n = g_p \text{ on } \Gamma_p^n \times (0, T], \tag{2.1g}$$

where the boundary Γ has been partitioned into disjoint parts for both the solid problem

Symbol	Description	Units
$()_t$	time derivative	s^{-1}
∇	gradient operator	m^{-1}
$\nabla\cdot$	divergence operator	m^{-1}
Tr	trace operator	dimensionless
$(\cdot)^T$	transpose operator	dimensionless
p	fluid pore pressure	Pa
u	elastic deformation	m
q	volumetric fluid flux	$\mathrm{m\,s}^{-1}$
f_p	fluid source density	s^{-1}
g_p	boundary fluid flux	$\mathrm{m\,s}^{-1}$
f_u	body force density	$\mathrm{N\,m}^{-3}$
g_u	traction	Pa
σ	stress tensor	Pa
$\bar{\sigma}$	Biot stress tensor	Pa
I	identity tensor	dimensionless
α	Biot coefficient	dimensionless
S_ε	drained storage coefficient	Pa^{-1}
k	hydraulic conductivity tensor	$\mathrm{m^3\,s\,kg}^{-1}$
μ_s	drained shear modulus	Pa
λ	second Lamé parameter	Pa

Table 2.1: Table of main notations and units used in the three-field formulation of Biot's poroelasticity theory.

$\Gamma = \Gamma_u^d \cup \Gamma_u^n$ and the fluid problem $\Gamma = \Gamma_p^d \cup \Gamma_p^n$, plus initial conditions

$$p(x,0) = p^0 \text{ on } \Omega, \tag{2.1h}$$

$$u(x,0) = u^0 \text{ on } \Omega, \tag{2.1i}$$

$$q(x,0) = q^0 \text{ on } \Omega. \tag{2.1j}$$

The AHC is modeled as a second-rank tensor. When the principal axis of hydraulic conductivity are aligned with the global coordinate system (x, y, z) this tensor can be represented as a diagonal matrix with entries k_{xx}, k_{yy} and k_{zz}

$$k = \begin{bmatrix} k_{xx} & 0 & 0 \\ 0 & k_{yy} & 0 \\ 0 & 0 & k_{zz} \end{bmatrix}.$$

The stress tensor is given for isotropic linear elasticity by Hooke's law

$$\varepsilon = \frac{1}{2}\left(\nabla u + (\nabla u)^T\right), \tag{2.2a}$$

$$\sigma = 2\mu_s \varepsilon + \lambda(\mathrm{Tr}\,\varepsilon) I, \tag{2.2b}$$

and the Biot stress tensor as

$$\bar{\sigma} = \sigma - \alpha p I, \tag{2.3}$$

with notations also described in Table 2.1.

2.3 Finite element discretization of Biot's poroelasticity model

In this section, we present an overview of the finite element method (FEM) and recall the three-field FEM discretization of Biot's theory, which broadly follows the original development in Ferronato et al. (2010).

2.3.1 FEM overview

The Finite Element Method (FEM) is a widely used numerical technique for solving partial differential equations (PDEs) across various fields, including structural mechanics, fluid dynamics, and geomechanics (Zienkiewicz et al., 2005; Hughes, 2012).

The FEM process begins by reformulating the governing PDEs into their weak (integral) form, which captures the physical behavior of the system at the element level—such as equilibrium equations in structural analysis (Bathe, 2006). Appropriate boundary conditions, such as prescribed displacements, pressures, or fluxes, are then applied to represent the physical constraints of the problem.

Next, the problem domain is discretized into a mesh composed of smaller subdomains known as elements. The weak form equations are solved locally within each element and subsequently assembled into a global system of equations that represents the behavior of the entire domain. This global system is then solved—typically using matrix-based numerical solvers—to compute the coefficients of the finite element basis functions (e.g.,

displacements or pressures), which in certain cases (such as first-order Lagrange elements) correspond directly to values at the mesh nodes (Zienkiewicz et al., 2005).

FEM is highly versatile, capable of handling complex geometries, heterogeneous material properties, and varied boundary conditions. The accuracy of the FEM solution depends on the type and quality of elements, as well as the mesh density. Finer meshes can yield more accurate results but require increased computational resources (Zienkiewicz et al., 2005; Reddy, 2019).

2.3.2 Notation

We recall the aquifer problem domain $\Omega \subset \mathbb{R}^3$ and its boundary Γ with outwards pointing normal n. For any subset ω of $\bar{\Omega} := \Omega \cup \Gamma$ we denote $L^2(\omega)$ as the usual Sobolev space of square integrable functions on ω, and $(\cdot,\cdot)_\omega$ the associated inner product, which for two arguments $f, g \in L^2(\omega)$ can be written

$$(f,g)_{L^2(\omega)} = \int_\omega fg \, \mathrm{d}x. \tag{2.4}$$

For brevity, we introduce the compact notation $(\cdot,\cdot)_\omega := (\cdot,\cdot)_{L^2(\omega)}$ and $(\cdot,\cdot) := (\cdot,\cdot)_{L^2(\Omega)}$. We can similarly denote $H^1(\omega)$ as the usual Sobolev space of square integrable functions with weak derivatives in $L^2(\omega)$ with associated inner product $(\cdot,\cdot)_{H^1(\omega)}$ defined as

$$(f,g)_{H^1(\omega)} = \int_\omega fg + \nabla f \nabla g \, \mathrm{d}x, \tag{2.5}$$

where ∇ is the usual gradient of a scalar function.

Finally, we introduce the slightly less standard Sobolev space $H(\mathrm{div};\omega)$ as the space of Sobolev space of vector-valued square integrable functions with square integrable divergence on ω

$$H(\mathrm{div};\omega) = \{f : f \in (L^2(\omega))^3 \ , \ \mathrm{div}\, f \in L^2(\omega)\}, \tag{2.6}$$

where the div operator is acting on a vector-valued function f with components (f_1, f_2, f_3)

can be written as

$$\operatorname{div} f := \nabla \cdot f := \frac{\partial f_1}{\partial x_1} + \frac{\partial f_2}{\partial x_2} + \frac{\partial f_3}{\partial x_3}. \tag{2.7}$$

2.3.3 Weak formulation

First, we need to define a function space for each field variable. To simplify what follows, but without loss of generality, we make the following regularity assumptions in space for the pressure

$$\mathcal{P} = \{p : \Omega \times [0,T] \to \mathbb{R} \mid p \in L^2(\Omega)\}, \tag{2.8a}$$

$$\mathcal{U} = \{u : \Omega \times [0,T] \to \mathbb{R}^3 \mid u \in (H^1(\Omega))^3,\ u = u_d \text{ on } \Gamma_u^d\}, \tag{2.8b}$$

$$\mathcal{Q} = \{q : \Omega \times [0,T] \to \mathbb{R}^3 \mid q \in H(\operatorname{div};\Omega),\ q \cdot n = g_p \text{ on } \Gamma_p^n\}. \tag{2.8c}$$

Additional sufficient regularity assumptions in time are also required, which we ignore for simplicity.

To derive the weak form of the system Eq. (2.1), we multiply them by test functions $\tilde{p} \in \mathcal{P}$, $\tilde{u} \in \mathcal{U}_0$, and $\tilde{q} \in \mathcal{Q}_0$, respectively, where

$$\mathcal{U}_0 = \{u \in \mathcal{U} \mid u_d = 0\}, \tag{2.9a}$$

$$\mathcal{Q}_0 = \{q \in \mathcal{Q} \mid g = 0\}, \tag{2.9b}$$

and then integrate over the domain Ω before applying any necessary integration by parts results to obtain a weak form that satisfies the required regularity assumptions.

Starting this process with Eq. (2.1a) we straightforwardly obtain

$$((S_\varepsilon p + \alpha \nabla \cdot u)_t, \tilde{p})_\Omega + (\nabla \cdot q, \tilde{p})_\Omega = (f_p, \tilde{p})_\Omega, \quad \forall \tilde{p} \in \mathcal{P}. \tag{2.10}$$

Continuing with Eq. (2.1b), we obtain

$$(-\nabla \cdot \bar{\sigma}, \tilde{u})_\Omega = (f, \tilde{u})_\Omega \quad \forall \tilde{u} \in \mathcal{U}_0, \tag{2.11}$$

and then using integration by parts gives for all $\tilde{u} \in \mathcal{U}_0$

$$(\nabla \cdot \bar{\sigma}, \tilde{u})_\Omega = -(\bar{\sigma}, \nabla \tilde{u})_\Omega + (\bar{\sigma} n, \tilde{u})_\Gamma \quad \forall \tilde{u} \in \mathcal{U}_0. \tag{2.12}$$

Splitting the integral on the boundary into its two constituent parts

$$(\bar{\sigma} n, \tilde{u})_\Gamma = (\bar{\sigma} n, \tilde{u})_{\Gamma_u^d} + (\bar{\sigma} n, \tilde{u})_{\Gamma_u^n}, \tag{2.13}$$

and, using the definition of the space $\mathcal{U}_0$ and the knowledge that $\bar{\sigma} n = g_u$ on Γ_u^n, allows us to write

$$(\bar{\sigma}, \nabla \tilde{u})_\Omega = (f, \tilde{u})_\Omega + (g_u, \tilde{u})_{\Gamma_u^n}, \quad \forall \tilde{u} \in \mathcal{U}_0. \tag{2.14}$$

Finally, for equation Eq. (2.1c) we obtain

$$(\nabla p, \tilde{q})_\Omega = -(k^{-1} q, \tilde{q})_\Omega, \quad \forall \tilde{q} \in \mathcal{Q}_0, \tag{2.15}$$

where k^{-1} denotes the inverse of k, and applying integration by parts on the term on the left hand side of Eq. (2.15) gives

$$-(\nabla \cdot \tilde{q}, p)_\Omega + (p, \tilde{q} \cdot n)_\Gamma = -(k^{-1} q, \tilde{q}), \quad \forall \tilde{q} \in \mathcal{Q}_0. \tag{2.16}$$

Splitting the integral on the boundary into its two constituent parts

$$(p, \tilde{q} \cdot n)_\Gamma = (p, \tilde{q} \cdot n)_{\Gamma_p^d} + (p, \tilde{q} \cdot n)_{\Gamma_p^n}, \tag{2.17}$$

and using the definition of the space $\mathcal{Q}_0$ and the knowledge that $q \cdot n = g$ on Γ_p^n and $p = p_d$ on Γ_p^d

$$-(k^{-1} q, \tilde{q})_\Omega + (p, \nabla \cdot \tilde{q})_\Omega = (p_d, \tilde{q} \cdot n)_{\Gamma_p^d}, \quad \forall \tilde{q} \in \mathcal{Q}_0. \tag{2.18}$$

In summary, the final variational problem is to find $p \in \mathcal{P}$, $u \in \mathcal{U}$, and $q \in \mathcal{Q}$ that

satisfy the equations

$$((S_\varepsilon p + \alpha \nabla \cdot u)_t, \tilde{p})_\Omega + (\nabla \cdot q, \tilde{p})_\Omega = (f_p, \tilde{p})_\Omega, \tag{2.19a}$$

$$(\bar{\sigma}(u,p), \nabla \tilde{u})_\Omega = (f, \tilde{u})_\Omega + (g_u, \tilde{u})_{\Gamma_u^n}, \tag{2.19b}$$

$$-(k^{-1}q, \tilde{q})_\Omega + (p, \nabla \cdot \tilde{q})_\Omega = (p_d, \tilde{q} \cdot n)_{\Gamma_p^d}. \tag{2.19c}$$

for all test functions $\tilde{p} \in \mathcal{P}$, $\tilde{u} \in \mathcal{U}_0$, and $\tilde{q} \in \mathcal{Q}_0$. We emphasize that in this three-field formulation the flux boundary condition Eq. (2.1g) is built strongly into the space $\mathcal{Q}$ and the pressure boundary condition Eq. (2.1f) occurs weakly in Eq. (2.19c). By contrast, in the classical two-field formulation the flux boundary condition occurs weakly and the pressure boundary condition is built strongly into a space $\mathcal{P}$ with stronger H^1-regularity requirements.

2.3.4 Discretization in time

For discretizing Eq. (2.19) in time, we use a first-order backwards Euler method, see e.g. Langtangen & Logg (2016) for full details.

Consider $M+1$ time steps $0 = t^0 < t^1 < t^2 < \ldots < t^M = T$ uniformly spaced on the interval $[0, T]$ giving a constant timestep $\Delta t = \Delta t^n = t^{n+1} - t^n$ for $n \in 0, \ldots, M-1$. The first-order backwards Euler scheme approximates the time derivative on the displacement u and pressure p as

$$(p^{n+1})_t \approx \frac{p^{n+1} - p^n}{\Delta t}, \quad \forall n \in 0, \ldots, M-1, \tag{2.20a}$$

$$(u^{n+1})_t \approx \frac{u^{n+1} - u^n}{\Delta t}, \quad \forall n \in 0, \ldots, M-1. \tag{2.20b}$$

Following standard arguments, and after some minor rearrangements, the discrete time version of Eq. (2.19) can be written: For $n = 0, \ldots, M-1$ find $p^{n+1} \in \mathcal{P}$, $u^{n+1} \in \mathcal{U}$, and

$q^{n+1} \in \mathcal{Q}$ such that

$$(S_\varepsilon p^{n+1} + \alpha \nabla \cdot u^{n+1} + \Delta t \nabla \cdot q^{n+1}, \tilde{p}) = (\Delta t f_p^{n+1} + S_\varepsilon p^n + \alpha \nabla \cdot u^n, \tilde{p}), \tag{2.21a}$$

$$-(\bar{\sigma}(u^{n+1}, p^{n+1}), \nabla \tilde{u}) = -(f_u^{n+1}, \tilde{u}) - (g_u^{n+1}, \tilde{u})_{\Gamma_u^n}, \tag{2.21b}$$

$$-(\Delta t\, k^{-1} q^{n+1}, \tilde{q}) + (\Delta t\, p^{n+1}, \nabla \cdot \tilde{q}) = (\Delta t p_d^{n+1}, \tilde{q} \cdot n)_{\Gamma_p^d}, \tag{2.21c}$$

for all test functions $\tilde{p} \in \mathcal{P}$, $\tilde{u} \in \mathcal{U}_0$, and $\tilde{q} \in \mathcal{Q}_0$. Note that Eq. (2.21c) has been multiplied by Δt to maintain symmetry with the term $(\Delta t \nabla \cdot q^{n+1}, \tilde{p})$ in Eq. (2.21a).

2.3.5 Discretization in space

For spatial discretization, we employ the mass-conservative three-field finite element formulation (Ferronato et al., 2010) ensuring conservation of mass within the numerical model. The implementation of the finite element formulation (Brenner & Scott, 2008) was carried out using DOLFINx, a finite element computing library (Baratta et al., 2023).

We are guided by Ferronato et al. (2010); Haagenson et al. (2020) in choosing finite element spaces in which the field variables p, u and q are approximated. Specifically, we approximate the pressure $p_h \in \mathcal{P}_h \subset \mathcal{P}$ by zero-order discontinuous Lagrange finite elements, the displacements $u_h \in \mathcal{U}_h \subset \mathcal{U}$ vector-valued first-order continuous Lagrange finite elements, and the flux $q_h \in \mathcal{Q}_h \subset \mathcal{Q}$ the vector-valued Brezzi–Douglas–Marini (BDM) elements (Brezzi et al., 1985) of lowest order which naturally discretize $H(\mathrm{div}; \Omega)$. This formulation is known to be inf-sup stable according to the stability theory of finite element methods (Brenner & Scott, 2008), to guarantee discrete mass conversation (Ferronato et al., 2010), and to be free from spurious pressure oscillations that can cause numerical issues in two-field pressure-displacement formulations of Biot's theory (Ferronato et al., 2010). We note that Ferronato et al. (2010); Alghamdi (2020) use a lowest-order Raviart-Thomas (RT) type space for the flux which has slightly weaker interpolation results than the BDM space used here.

2.3.6 Boundary conditions

In this problem, we need to define both solid and fluid boundary conditions to properly capture the coupled poroelastic behavior of the aquifer system. The solid boundary conditions govern the behavior of mechanical deformation of the system, while the fluid boundary conditions control the constraints on groundwater flow.

Dirichlet and Neumann boundary condition (BC) are two fundamental types of boundary conditions used in solving partial differential equations (PDEs). In our PDE-based model, we apply these boundary conditions based on their physical relevance. The Dirichlet boundary condition specifies the function's value on the boundary, which is useful for enforcing fixed displacements in the solid problem or maintaining fixed hydraulic pressure in the fluid problem. The Neumann boundary condition, on the other hand, defines the derivative (or flux) of a function at the boundary, representing external forces (e.g., stress) in the solid domain or prescribed fluid flow rates in the fluid domain.

2.3.7 Mesh generation

Mesh generation is a crucial step in finite element analysis, where a complex geometry is discretized into smaller, simpler elements over which Biot's equations can be numerically solved. For this purpose, we use Gmsh (Geuzaine & Remacle, 2009), an open-source mesh generation tool that enables the definition of geometry, assignment of physical regions (e.g., boundaries and material zones), and creation of high-quality meshes.

In modeling the aquifer system, the resulting 3D mesh conforms to the conceptual model of the multilayered subsurface. It incorporates variable element sizes across different locations and layers to allocate higher spatial resolution where it is most needed. While finer elements increase spatial resolution and accuracy, they also lead to higher computational costs. Therefore, mesh refinement is selectively applied—for example, near the pumping well—to accurately capture localized pressure gradients and deformation effects with reduced numerical error.

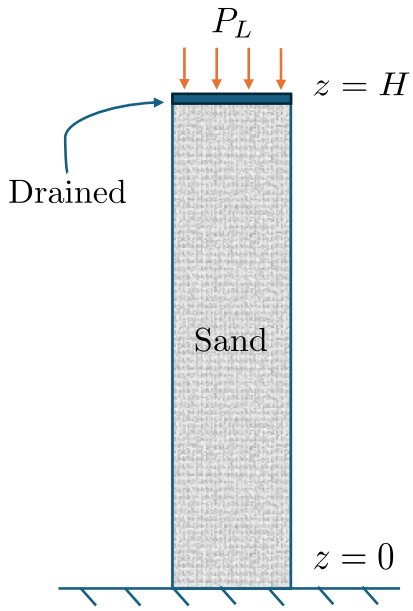

Figure 2.1: Schematic of Terzaghi's one-dimensional consolidation problem, represented by a column of height H. A downward load P_L is applied at time $t = 0$.

2.4 Validation using Terzaghi's consolidation problem

In this section, we first present the theory behind Terzaghi's consolidation problem along with its analytical solution. We then compare the classical Terzaghi model with the more general Biot poroelasticity model. Following this, we describe how the Terzaghi problem can be implemented in three dimensions using Biot's equations. Finally, we validate our numerical implementation by comparing the 3D poroelastic finite element solution with Terzaghi's analytical solution.

2.4.1 Terzaghi's one-dimensional consolidation theory

Terzaghi's consolidation model (Terzaghi, 1925) is a classical analytical solution describing the dissipation of excess pore pressure (increase in pore pressure above the initial pressure) in a saturated soil layer under loading P_L. The model assumes vertical flow and deformation only, with drainage allowed at the top boundary (see Fig. 2.1). The governing equation is a one-dimensional diffusion equation. Given a domain $\Omega_T := [0, H] \subset \mathbb{R}$

with boundary Γ_T find the fluid pressure $p_T : \Omega_T \times (0, T] \to \mathbb{R}$ such that

$$\frac{\partial p_T}{\partial t} = c_v \frac{\partial^2 p_T}{\partial z^2}, \tag{2.22}$$

where c_v $\mathrm{m}^2\,\mathrm{s}^{-1}$ is the coefficient of consolidation (see Table 2.2), with boundary conditoins

$$p_T = p_d = 0 \text{ on } \Gamma_p^d (\coloneqq z = H) \times (0, T], \tag{2.23}$$

$$-k \nabla p_T \cdot n = g_p = 0 \text{ on } \Gamma_p^n (\coloneqq z = 0) \times (0, T], \tag{2.24}$$

and initial conditions

$$p_T(z, 0) = p_T^0 \text{ on } \Omega_T. \tag{2.25}$$

This equation, as a diffusion-type PDE, illustrates how pressure dissipates over time due to drainage, which leads to soil consolidation.

Although Terzaghi's original formulation does not explicitly provide a displacement equation, vertical deformation $u_T(z, t)$ is governed by changes in pressure through the effective stress principle:

$$\sigma' = \sigma - p_T(z, t), \tag{2.26}$$

assuming a constant stress $\sigma = -P_L$ applied at $t = 0$, the vertical strain ε_z is given by

$$\varepsilon_z = \frac{\partial u}{\partial z} = m_v(\sigma - p_T(z, t)), \tag{2.27}$$

where m_v is the coefficient of volume compressibility (see Table 2.2) and deformation $u_T : \Omega_T \times (0, T] \to \mathbb{R}$ is obtained by integrating the strain over the domain

$$u_T(z, t) = \int_0^z \varepsilon_z(z, t)\, dz. \tag{2.28}$$

2.4.2 Analytical solution

The analytical solution to Terzaghi's equations is expressed as:

$$p_T(z,t) = \frac{4}{\pi} p_T^0 \sum_{n=0}^{\infty} \frac{1}{2n+1} \sin\left(\frac{(2n+1)\pi z}{2H}\right) \exp\left(-\frac{(2n+1)^2 \pi^2 c_v t}{4H^2}\right), \tag{2.29}$$

where p_{T0} is the initial pressure

$$p_T^0 = \frac{\alpha M}{K_u + 4\mu_s/3} P_L, \tag{2.30}$$

and other parameters are in Table 2.2.

Description	Symbol	Unit	Value
Column height (length)	H	m	15.0
Prescribed distributed load	P_L	Pa	10^4
Hydraulic conductivity of sand	k	$\mathrm{m^3\,s\,kg^{-1}}$	1.02×10^{-9}
First Lamé parameter	λ	Pa	4×10^7
Shear modulus	μ_s	Pa	4×10^7
Biot coefficient	α	-	1.0
Biot modulus	M	Pa	2.3×10^{-10}
Specific weight of water	ρg	$\mathrm{N\,m^{-3}}$	9807
Undrained bulk modulus	K_u	Pa	$\lambda + 2\mu_s/3 + \alpha^2 M$
Vertical uniaxial compressibility	c_M	$\mathrm{Pa^{-1}}$	$(\lambda + 2\mu_s)^{-1}$
Coefficient of volume compressibility	m_v	$\mathrm{Pa^{-1}}$	$M^{-1} + \alpha^2 c_M$
Coefficient of consolidation	c_v	$\mathrm{m^2\,s^{-1}}$	k/m_v
Drained storage coefficient	S_ε	$\mathrm{Pa^{-1}}$	$1/M$

Table 2.2: Parameters in Terzaghi's consolidation formulation. The upper section lists the principal values, while the lower section presents model parameters along with their relationships to other parameters.

The vertical displacement $u_T(z,t)$ is given by

$$u_T(z,t) = u_T^0(z) + c_M p_T^0 \Bigg[(H - z) - \frac{8H}{\pi^2} \sum_{n=0}^{\infty} \frac{1}{(2n+1)^2} \cos\left(\frac{(2n+1)\pi z}{2H}\right) \exp\left(\frac{-(2n+1)^2 \pi^2 c_v t}{4H^2}\right) \Bigg], \tag{2.31}$$

where

$$u_T^0(z) = \frac{1}{K_u + 4\mu_s/3} P_L (H - z), \tag{2.32}$$

and other parameters are in Table 2.2.

2.4.3 Relation to Biot's poroelasticity theory

Terzaghi's model is a simplified, one-dimensional case of Biot's more general poroelastic theory. While Terzaghi considers only vertical deformation and fluid flow, Biot's framework models the full coupling of stress and pressure in porous media across one, two, or three dimensions.

Feature	Terzaghi Model	Biot Model
Dimensionality	1D	1D, 2D, or 3D
Governing equations	Diffusion equation	Coupled elasticity + Darcy's law
Material behavior	Linear elastic, compressible	Fully tensorial elastic behavior
Flow direction	Vertical only	Multidirectional
Coupling	No coupling	Full stress–pressure coupling
Solution type	Analytical	Numerical (e.g., FEM)

Table 2.3: Comparison between Terzaghi and Biot poroelasticity models

2.4.4 3D implementation of the Terzaghi problem

Although Terzaghi's model is formulated in 1D, a similar model can be implemented in 3D to validate numerical poroelastic solvers. By designing the computational setup to enforce effectively one-dimensional behavior, we can replicate the analytical conditions numerically.

We use the three-field Biot's equations Eq. (2.1) to implement Terzaghi problem. The domain consists of a tall, narrow box with 1m $\times$ 1m $\times$ Hm dimension (see Fig. 2.2), discretized with a structured mesh refined in the vertical direction. A uniform initial pressure is applied throughout the domain. Drainage is permitted at the top surface, while the lateral surfaces are constrained to prevent horizontal displacement and lateral fluid flow. Boundary conditions are presented in Table 2.4.

The system is then solved using a poroelastic finite element solver to track time-dependent pressure dissipation and vertical deformation. Table 2.2 presents the model parameters that are used in the numerical simulation and analytical solution.

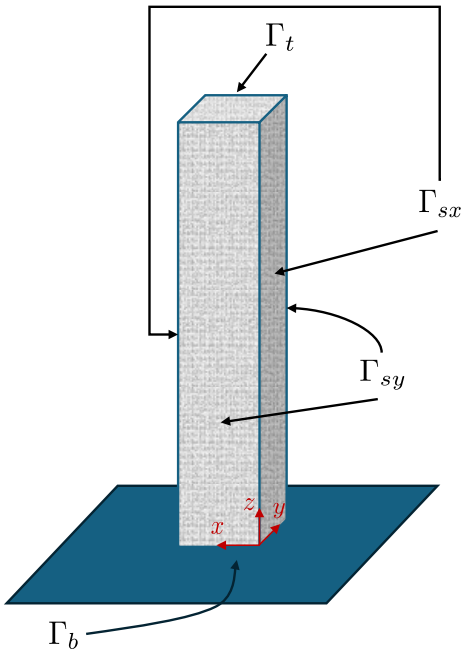

Figure 2.2: 3D representation of Terzaghi's problem using a box domain with $1\text{m} \times 1\text{m} \times H\text{m}$ and defined boundaries.

	Boundary condition	Boundary
Fluid problem (q, p)	$q \cdot n = 0$	$\Gamma_b \cup \Gamma_{sx} \cup \Gamma_{sy}$
	$p = 0$	Γ_t
Solid problem (u)	$u = 0$	Γ_b
	$u_x = 0$	Γ_{sx}
	$u_y = 0$	Γ_{sy}
	$\sigma \cdot n = g_u = (0, 0, -P_L)$	Γ_t

Table 2.4: Boundary conditions of fluid and solid problem of 3D Terzaghi consolidation problem.

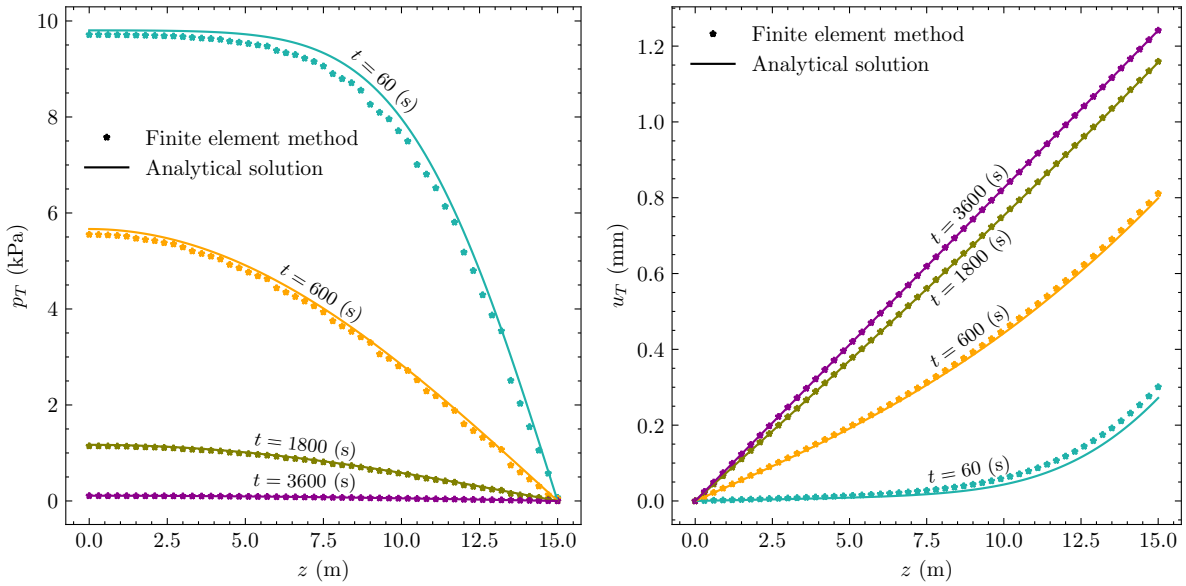

(a) Analytical and numerical solutions for the pressure.

(b) Analytical and numerical solutions for the vertical displacement.

Figure 2.3: Comparison of analytical and numerical solutions of pressure and vertical deformation in the Terzaghi consolidation problem. The jump behavior observed in the numerical pressure results arises from the use of an L^2 function space for the pressure field, which does not enforce continuity between adjacent elements.

2.4.5 Model validation

To validate our numerical implementation, we compare the 3D finite element solution of the Terzaghi problem against its 1D analytical counterpart. We model the 3D Terzaghi problem using Biot's equation so which represents 1D behavior, to be able to compare with the analytical solution.

Figure 2.3 show close agreement between the analytical and numerical results in both vertical displacement and pressure dissipation. This confirms the accuracy of the poroelastic solver in capturing the essential mechanics of consolidation and builds confidence in applying the model to more complex hydrogeological scenarios in the following chapters.

Chapter 3

Can the anisotropic hydraulic conductivity of an aquifer be determined using surface displacement data? A case study

The content of this chapter is based on part of the following paper.

Salehian Ghamsari, S., van Dam, T., and Hale, J. S. (2025). Can the anisotropic hydraulic conductivity of an aquifer be determined using surface displacement data? A case study. *Applied Computing and Geosciences*, Volume 26, June 2025, 100242. 10.1016/j.acags.2025.100242

Authorship statement

Sona Salehian Ghamsari: Data curation, Methodology, Software, Formal analysis, Investigation, Writing - Original Draft, Validation, Visualization. Tonie van Dam: Conceptualization, Writing - Review & Editing, Funding acquisition, Supervision. Jack S. Hale: Conceptualization, Methodology, Software, Investigation, Writing - Review & Editing, Funding acquisition, Project administration, Supervision.

Abstract

Due to geological features such as fractures, some aquifers demonstrate strongly anisotropic hydraulic behavior. The goal of this study is to use a poroelastic model to calculate surface displacements given known pumping rates to predict the potential utility of InSAR data for inferring information about AHC in aquifer systems. To this end, we develop a three-dimensional anisotropic poroelastic model mimicking the main features of the 1994 Anderson Junction aquifer test in southwestern Utah with a 24 to 1 ratio of hydraulic conductivity along the principal axes, previously estimated in the literature using traditional well observation techniques. Under suitable model assumptions, our results show that anisotropy in the hydraulic problem leads to a distinctive elliptical surface displacement pattern centered around the pumping well that could be detected with InSAR. We interpret these results in the context of InSAR acquisition constraints and provide guidelines for designing future pumping tests so that InSAR data can be used to its full potential for improving the characterization of aquifers with anisotropic hydraulic behavior.

3.1 Introduction

Groundwater is a vital resource that provides drinking water to billions of people and supports critical agriculture and industrial activities (Food and Agriculture Organization of the United Nations (FAO), 2022). One of the biggest challenges for sustainability of global groundwater resources is overexploitation (Basu & Van Meter, 2014; Caretta et al., 2022). The consequences of overexploitation include reducing the amount of water available to surface water bodies (Walker et al., 2020), lowering the water table to the extent that it leads to surface subsidence (V. M. Heilweil & Hsieh, 2006; Burbey et al., 2006; Galloway & Burbey, 2011) and saltwater intrusion (Q. Guo et al., 2019). Over-exploitation of groundwater resources is a global issue with the largest impacts in areas with high population densities, rapid urbanization and agricultural intensification (Poland, 1984; Famiglietti et al., 2011; Erkens et al., 2015).

Consequently, there is a need for increased research and monitoring to understand better the complex hydrological processes that govern groundwater systems and contribute data to support effective management strategies. To this end, groundwater modeling and simulation tools have become an increasingly important component in supporting decision-makers to design effective strategies (Singh, 2014; Amitrano et al., 2014). One aspect of ensuring that groundwater simulation tools can produce reasonable predictions is ensuring that all possible data sources are assimilated into the model for e.g. parameter inference. Specifically, in this study, we ask "is there potentially valuable information in InSAR data for inferring AHC in a poroelastic model of an aquifer?". This question forms part of broader research efforts on developing new approaches for assimilating remote sensing data into hydrogeomechanical models of aquifers – however, we do not tackle the data assimilation problem here.

The use of InSAR in hydrogeological research has become increasingly popular due to its high precision in measuring ground surface displacement, wide-area coverage and cost-effectiveness (Guzy & Malinowska, 2020; Galloway & Hoffmann, 2007). InSAR observations of surface uplift and subsidence allow inference of groundwater levels and flow gradients (Gambolati & Teatini, 2015). InSAR observations can be used to determine the structural boundaries of aquifer systems (Chaussard et al., 2014; Haghighi & Motagh, 2019; X. Hu & Bürgmann, 2020), provide the temporal evolution of the ground surface (Zhou et al., 2018; L. Guo et al., 2019; Bonì et al., 2017) and to contribute to estimate storage coefficients and hydraulic conductivity (X. Hu et al., 2018; Bonì et al., 2016; Chaussard et al., 2014). Development of InSAR technology has contributed to the regional hydrogeological models of groundwater flow and land deformation (Galloway & Hoffmann, 2007; Gambolati & Teatini, 2015). Since the accuracy of the InSAR measurement is the most important parameter for the estimation of the aquifer properties (Guzy & Malinowska, 2020) and using InSAR time-series enhances the accuracy of surface displacement estimation (Li et al., 2022), consequently using InSAR time-series would improve the accuracy of estimating aquifer properties.

The pumping of subsurface fluids during an aquifer test causes a drop in pore pressure which leads to a three-dimensional deformation. This response has been simulated using a number of modeling approaches, see e.g. (Guzy & Malinowska, 2020). While conventional

groundwater flow theory in the aquitard drainage model has been widely used (Helm, 1986; Harbaugh et al., 2000; Hoffmann et al., 2003; Harbaugh, 2005) it has been argued that the use of numerical poroelasticity models is necessary for realistic aquifer settings (Hsieh, 1996). The theory of poroelasticity introduced by Biot (1941) describes the interactions between water, the porous matrix of rock and solid grains. This theory explains how changes in pressure and fluid content within the porous matrix can cause deformation and stress among the solid grains, and vice versa. Verruijt (1969) proposed a formulation of Biot's linear theory that is suitable for problems in soil mechanics. In the context of calibrating groundwater flow models with InSAR-derived displacement data, it is necessary to use a model that directly links fluid flow to deformation by including poroelasticity theory.

The underlying cause of AHC in hydrogeology is often a preferential rock fracturing direction that allows for higher fluid conductivity along the direction of fractures (Berre et al., 2019). The recognition of the importance of AHC on the behaviour of aquifer systems dates back to the work of Papadopulos (1965) who presented a method to determine the hydraulic conductivity of a homogeneous anisotropic aquifer from the observation of pressure (head drop) at a minimum of three wells situated at different directions around a constant-rate aquifer extraction test. V. M. Heilweil & Hsieh (2006) demonstrated that AHC could be inferred from two observation wells, if the wells are assumed to be aligned with the principal directions of AHC. The possibility was also mentioned by Burbey (2006).

In the specific context of AHC and geodesy, both Burbey et al. (2006) and Burbey (2006) proposed that the elliptical vertical surface displacement pattern observed from GPS receivers positioned around a Nevada pumping test could be directly related to the interaction between an anisotropy in the fluid flow and rock skeleton. In support of this theory, Burbey (2006) presented computer simulations based on a poroelasticity theory showing elliptical vertical displacement patterns at the Earth's surface under a 3 to 1 AHC ratio. The elliptic pattern in the displacements is driven by the underlying anisotropy in the fluid problem caused by the fractures tedency to provide directional conduits for flow.

Galloway & Hoffmann (2007) showed that InSAR can be used to calibrate numerical

models of groundwater flow and deformation. Galloway & Burbey (2011) conducted a review of various remote sensing techniques and models used for studying subsidence due to groundwater extraction. Hesse & Stadler (2014) proposed scalable computational methods for assimilating InSAR data into a poroelastic finite element model with spatially varying isotropic hydraulic conductivity within a Bayesian framework. Continuing with the line of work developed by Hesse & Stadler (2014), recently Alghamdi (2020); Alghamdi et al. (2020, 2021) assimilated InSAR data from the test site of Burbey et al. (2006) into a spatially-varying IHC poroelastic model. We remark that in the original study of Burbey et al. (2006) it is mentioned that due to the underlying geology (fracturing) the hydraulic behavior of the site is likely to be strongly anisotropic and therefore the isotropic model used in Alghamdi (2020) for calibration using the data from Burbey et al. (2006) may be insufficient to fully capture the anisotropic behaviour of the site. In addition, the elliptical shape observed in the surface displacement measured by the InSAR technique, as shown in (Alghamdi et al., 2020, Figure 1c), may be evidence of anisotropy, as discussed by Burbey (2006). As discussed in Section 1.5, the elliptical shape observed in the surface displacement measured by the InSAR technique, as shown in Fig. 1.2, may be evidence of anisotropy, as discussed by Burbey (2006).

In this study, we develop a three-dimensional linear poroelastic model that includes AHC to gain insight into the relationship between surface displacement and pumping at Anderson Junction in southwestern Utah. The goal is to use our anisotropic model to calculate surface displacements given known pumping rates to predict the potential utility of InSAR data for inferring information about AHC in aquifer systems. We choose this site because V. M. Heilweil & Hsieh (2006) specifically studied the role of anisotropy there, giving estimated AHC ratio of around 24 to 1 determined using two observation wells. Using our model, we predict the InSAR LOS displacements for the region, i.e. the quantity of interest for calibration of the model against theoretical InSAR observations (Alghamdi, 2020).

We show that the duration of four days and rate of the pumping used in the Anderson Junction test was likely insufficient to induce surface displacements that can be measured with InSAR. We then run our model under a number of alternative scenarios, including different pumping rates, pumping lengths and anisotropy ratios to determine when the

displacements would be observable by InSAR. We conclude that there could be pumping regimes in which InSAR data could contain important information about AHC. Finally, we discuss some guidelines for designing future pumping tests in the context of InSAR acquisition constraints.

An outline of this manuscript is as follows. Section 3.2 provides an overview of the Anderson Junction study area and the aquifer test. In Section 2.2, we outline the theoretical foundations by presenting the Biot equations. In Section 3.3, we introduce the InSAR technique and present the transformation of the three-dimensional deformations into InSAR LOS observations. In Section 3.4, we describe our proposed model in detail. The outcomes of our simulations are presented in Section 3.5. Finally, in Section 3.6, we present our conclusions from our study.

3.2 Case study

Our case study is located at Anderson Junction, Utah, USA (see Fig. 3.1), and is based on the pumping test conducted by the US seological survey (USGS) in March and April 1996 (V. M. Heilweil & Hsieh (2006)). In this section, we provide a review of the main geologic and hydrologic features of the site. This information will be used in Section 3.4 to setup a simplified conceptual model of the Anderson Junction site.

3.2.1 Pumping test

The Anderson Junction aquifer pumping test was conducted to determine the Navajo Sandstone's transmissivity and storage properties in the vicinity of Anderson Junction. Full details can be found in the original study (V. Heilweil et al., 2000). The test involved a multiple-well setup, including a pumping well (`(C-40-13)28dcb-2`) and two observation wells (`(C-40-13)28dca-1`, from now on referred to as well A, `(C-40-13)28dcc-1`, from now on referred to as well B). Groundwater was pumped for approximately 4 d at an average rate of $P_r = 6000\,\mathrm{m^3\,d^{-1}} = 0.07\,\mathrm{m^3\,s^{-1}}$ (V. Heilweil et al., 2000). The information about the pumping and observation wells can be found in U.S. Geological Survey (2016).

The aquifer test protocol is depicted in Fig. 3.2. This protocol will be used in the

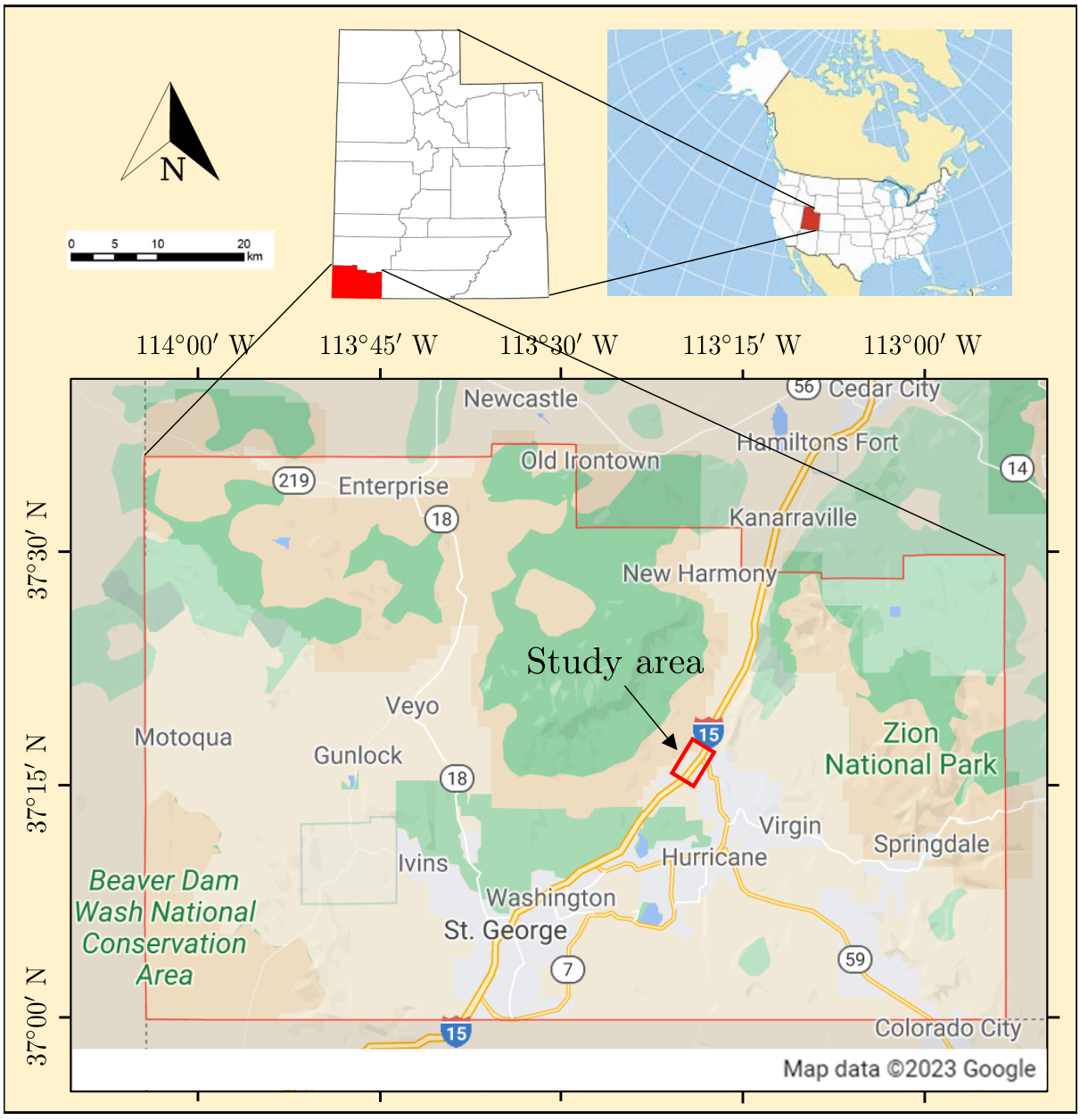

Figure 3.1: Location of the Anderson Junction site in Utah, USA. Lower map data Copyright Google 2023.

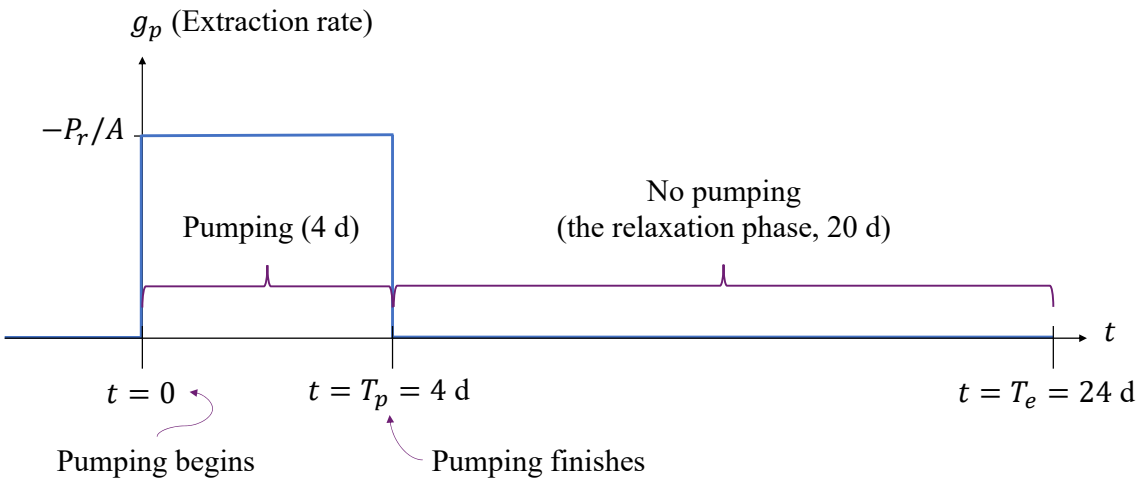

Figure 3.2: Aquifer test protocol. The pumping phase began at $t = 0$ with a constant extraction rate of $g_p = -P_r/A$. The pumping ceased at $t = T_p = 4$ d, followed by a 20-day relaxation phase.

model and will be discussed in more detail in Section 3.4.2 and Fig. 3.8. The pumping began at $t = 0$ d with a constant extraction rate of $g_p = -P_r/A$ m s^{-1}, where A m^2 denotes the area of the pumping boundary. The pumping stopped at $t = T_p = 4$ d and the extraction rate (g_p) returned to zero. Following the four-day pumping phase, the field observations continued for an additional 20 d ($t = T_e = 24$ d) to capture the relaxation phase and to measure transmissivity.

3.2.2 Cross section

The cross-section illustration Fig. 3.3 of the Anderson Junction region provides information that can be used to better understand the layered structure of the aquifer. In Fig. 3.3, the detailed geologic cross-section of Anderson Junction is shown, as documented in Hurlow (1998), while Fig. 3.4 indicates the location of the II' cross-section transect line. The case study area is highlighted by a red rectangle in both figures. Faults are visually depicted as nearly vertical lines in the cross-section.

According to V. M. Heilweil & Hsieh (2006), the Anderson Junction site features a confined aquifer characterized by a 180 m thick deposit of Navajo sandstone. This indicates the presence of upper and lower confining layers in addition to the aquifer layer. The geologic map of Washington County (Hintze, 1980) shows that Anderson Junction's

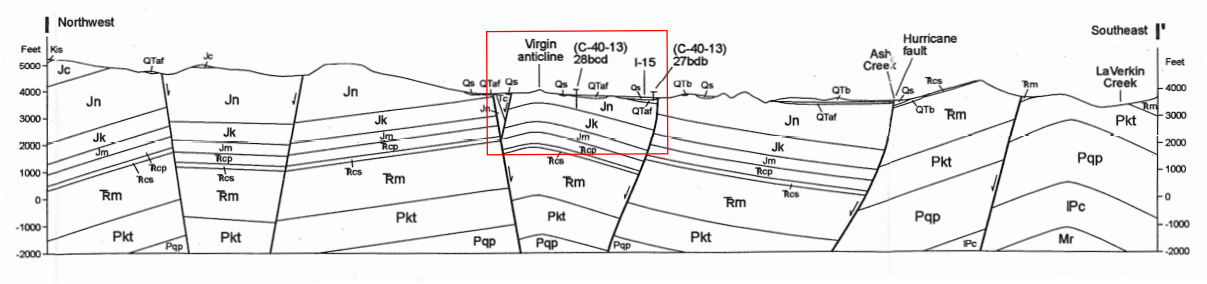

Figure 3.3: Geologic cross-section of Anderson Junction site (Image courtesy of U.S. Geological Survey (Hurlow, 1998) in the U.S. Public Domain.). On the y-axis is elevation in feet with respect to mean sea level. The red rectangle highlights the case study area. The cross-section reveals the geological layers, including the unconsolidated alluvial and colluvial deposits (Qs) on the surface as the upper confining layer, the Navajo sandstone (Jn) as the aquifer layer, and the Kayenta formation (Jk) as the lower confining layer. Faults are depicted as nearly vertical lines.

surface primarily consists of unconsolidated mixed alluvial and colluvial deposits. The geologic cross-section shows that beneath the alluvial and colluvial layer lies the Navajo sandstone, acting as the aquifer layer, thereby making the alluvial and colluvial layer the upper confining layer, while the lower layer corresponds to the Kayenta formation, serving as the lower confining layer.

3.2.3 Fracturing

The Anderson Junction site is strongly characterized by fracturing of the Navajo sandstone, with two fracture clusters: a primary cluster at orientation of 180° to 210°, and secondary cluster at orientation of 90° to 130° with respect to north. Figure 3.5a shows a rose diagram (radial histogram) summarising the relative frequency of fracture trends based on outcrop data.

Comparing the magnitudes of the principal hydraulic conductivities (Fig. 3.5b) computed via the method proposed by V. M. Heilweil & Hsieh (2006) with the fault density summarized in the rose diagram (Fig. 3.5a), we note that the major principal direction of hydraulic conductivity is approximately aligned with the secondary clusters of fracture density. Conversely, the minor principal direction of hydraulic conductivity coincides with the primary clusters of fracture density. It is also important to note that the rose diagram (Fig. 3.5a) summarizes outcrop data acquired at the surface, while the magnitudes of the

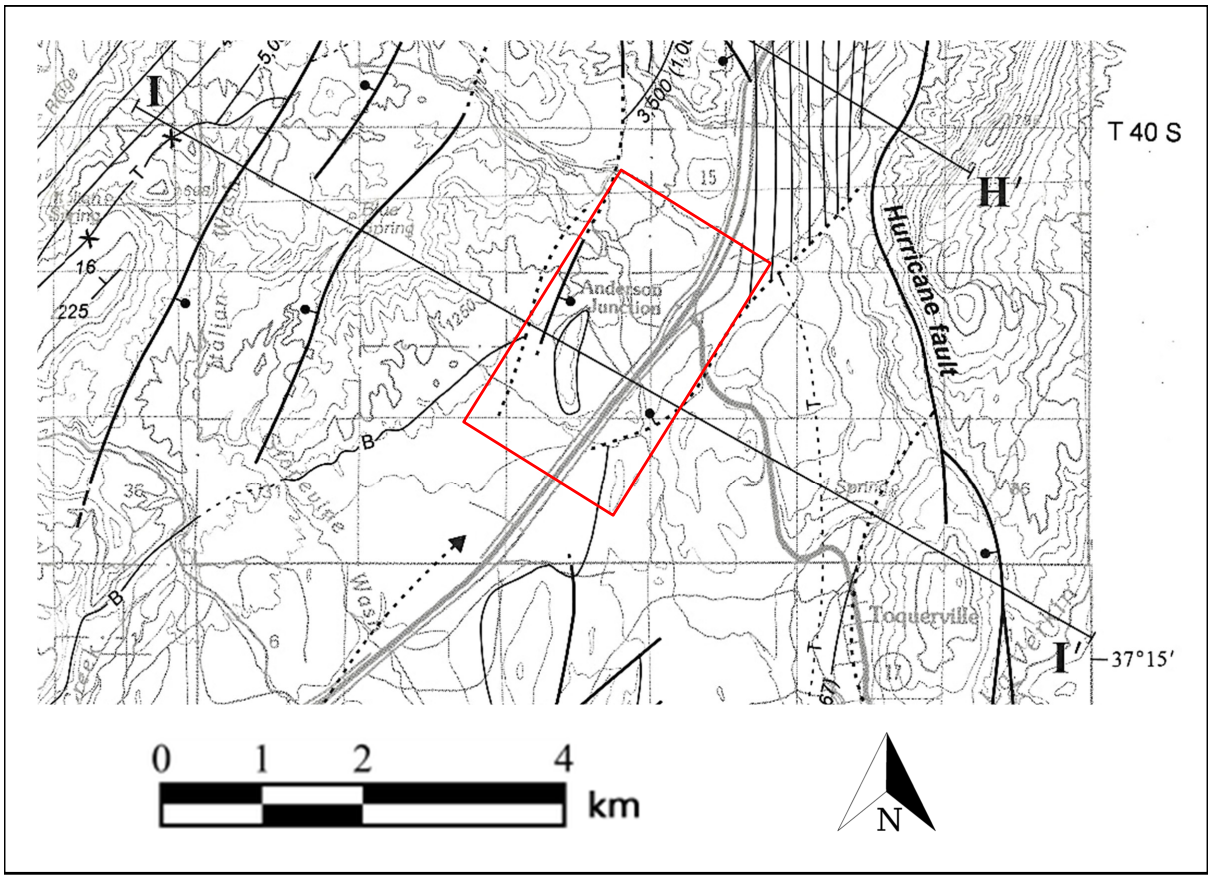

Figure 3.4: Location of the II' cross-section transect line on structure-contour map. The study area is highlighted by a red rectangle. Note that the orientation of the cross-section aligns with the axis of major hydraulic conductivity shown in Fig. 3.5b. (Image courtesy of U.S. Geological Survey (Hurlow, 1998) in the U.S. Public Domain.)

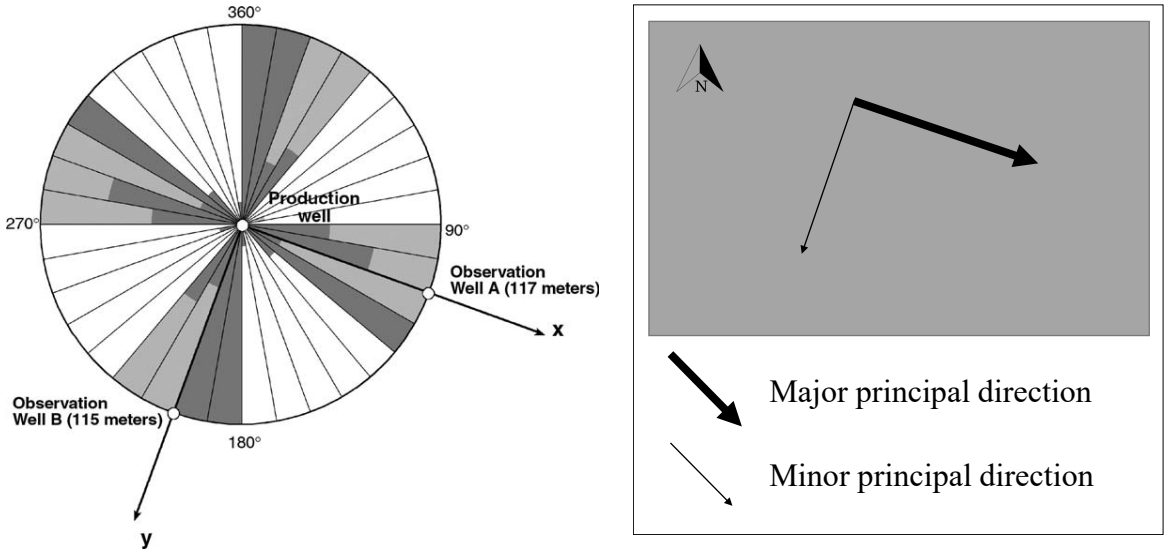

(a) Rose diagram of fracture density

(b) Principal directions of hydraulic conductivity

Figure 3.5: (a). Rose diagram showing fracture orientations (from V. M. Heilweil & Hsieh (2006)) and locations of pumping and observation wells used for the Anderson Junction aquifer test. (b). Principal directions of hydraulic conductivity of the Anderson Junction aquifer system derived from modified Papadopulos method in V. M. Heilweil & Hsieh (2006). Arrows represent major and minor principal directions, indicating that hydraulic conductivity in the major direction is approximately 24 times greater than in the minor direction. Note: Arrow lengths do not signify the scale of hydraulic conductivity.

principal hydraulic conductivities are inferred from pressure drop measurements taken in the aquifer layer.

3.2.4 Faults

Figure 3.6 is a fault map of the study area, with the Anderson Junction site highlighted within a red rectangle. The Navajo Sandstone and Kayenta Formation exhibit dip angles due to tilting associated with the Hurricane Fault. It is estimated that the top of the Navajo Sandstone may lie approximately 610 m below sea level (Hurlow, 1998). Within the Anderson Junction aquifer, several faults act as boundaries to water transport. The Hurricane Fault fully offsets the Kayenta Formation and Navajo Sandstone along its entire length. Additionally, an unnamed series of faults between Anderson Junction and Toquerville partially offsets the Navajo Sandstone and Kayenta Formation in the study area. These faults, along with others whose precise offset cannot be determined, appear to impede groundwater flow perpendicular to their fault planes. The low permeability observed along the fault planes is attributed to the presence of poorly-sorted breccia and clay-rich materials (Hurlow, 1998).

3.3 Precision of InSAR displacement measurements

In this section, we indicate the precision of the InSAR technique in measuring displacement, a critical information in evaluating its suitability for analyzing the Anderson Junction aquifer displacement. Then, we provide an equation to compute LOS displacement from the deformation field predicted by the Biot equations to compare with InSAR precision.

InSAR is a technique used to measure displacements of the Earth's surface over time using phase differences of two SAR images acquired from different satellite positions and at different times. In general, the precision of the determined surface displacements can range from millimeters to centimeters (Bamler & Hartl, 1998). However, the actual precision in practical applications is influenced by spatial-temporal decorrelation and atmospheric delays. In recent years, researchers have actively sought solutions to address

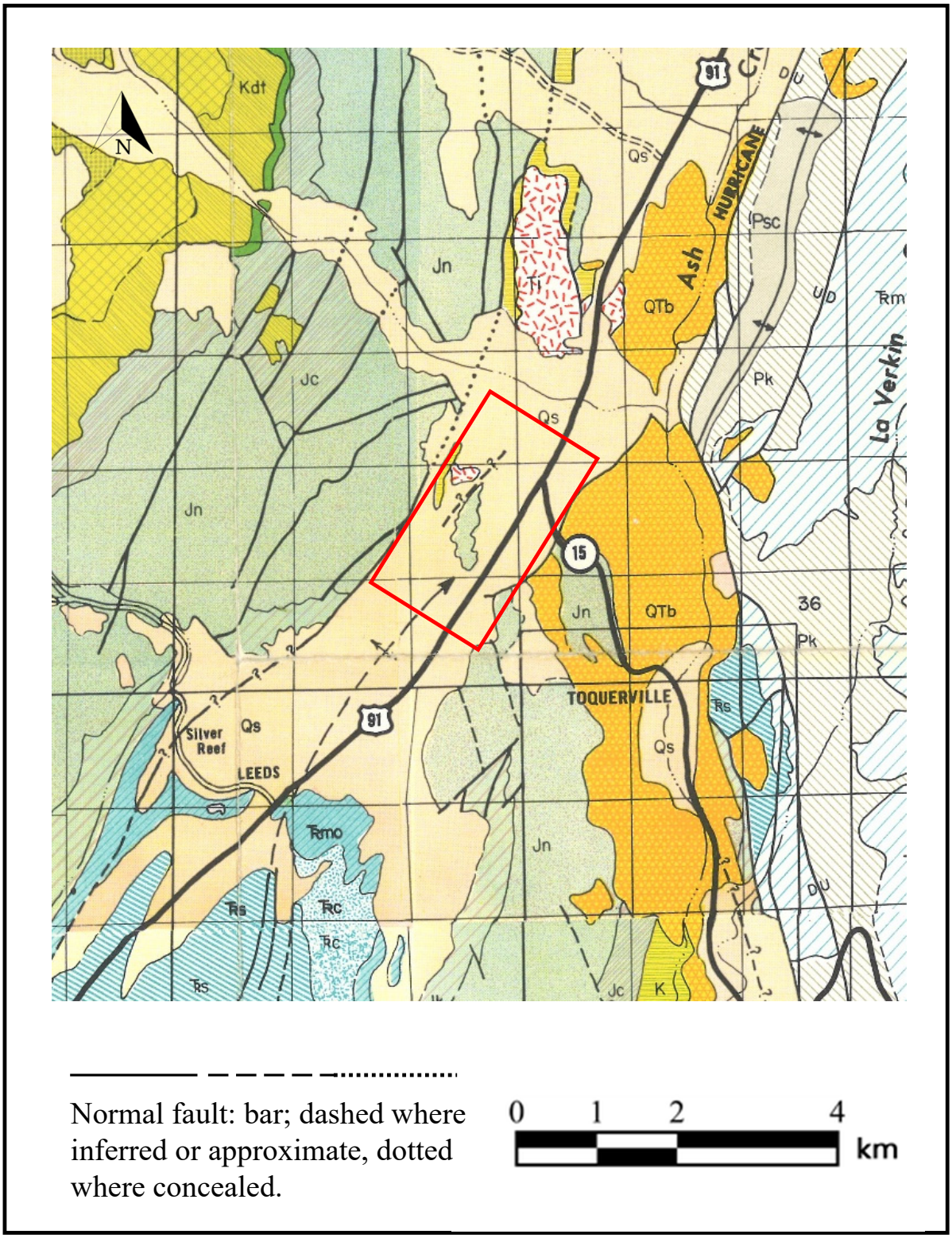

Figure 3.6: Fault map of the Anderson Junction area, indicating the study area within a red rectangle. The map highlights the presence of the Hurricane fault and other faults acting as boundaries around the Anderson Junction aquifer. (Image courtesy of U.S. Geological Survey (Cook, 1960) in the U.S. Public Domain.)

these limitations, leading to the development of a variety of multi-temporal InSAR (MT-InSAR) algorithms (J. Hu et al., 2014).

To assess if the Anderson Junction aquifer test induced detectable surface displacement using the InSAR technique, we need to acquire multiple SAR data during the test period. In 1996, there were four operational SAR satellites: ERS-1, ERS-2, RADARSAT-1, and JERS-1. However, due to the unavailability of proper SAR data in the Anderson Junction area in the aquifer test time (March and April 1996), and considering the brief test duration (4 d) versus the repeat cycle of SAR data in 1996 (approximately 24 d to 35 d), obtaining sufficient data is not possible. So, we can compare the InSAR accuracy with the surface displacement predicted by the proposed model. This is one of our motivations for building the poroelastic model to be able to simulate the aquifer test and measure the surface displacement.

In this study, we explore the surface displacement accuracy of Sentinel-1 as an example. This choice is motivated by its favorable attributes, including an extensive area coverage (global coverage), open data policy (free data), high temporal resolution (6 d), and long projected mission lifespan (2013-present).

Several studies have examined the precision of displacement measurements derived from Sentinel-1 InSAR. These investigations have shown that achieving sub-centimeter precision is possible for individual displacement records within the time series (Cigna et al., 2021). To assess precision, these studies compare Sentinel-1 displacement with various references, including artificial corner reflectors (Quin & Loreaux, 2013), global navigation satellite system (GNSS) measurements (Duan et al., 2020; Bovenga et al., 2013), and geodetic leveling measurements (Raucoules et al., 2009). Notably, comparisons between Sentinel-1 InSAR data and GNSS measurements reveal a precision of less than 5 mm (Manunta et al., 2019) or 8 mm (Duan et al., 2020) for InSAR time series projected along the satellite's LOS. We will use the precision of InSAR displacement measurement to compare with the calculated LOS displacement to check the possibility of using InSAR for the Anderson Junction aquifer test. If the computed LOS is equal to or larger than the InSAR precision, we consider the deformation signal detectable.

3.3.1 Calculating LOS displacement

The SAR data use side-looking images, with radar pulses emitted in the LOS direction, oriented perpendicular to the satellite's direction of motion. The LOS is an imaginary line that connects the antenna to the specific point on the Earth's surface being imaged, inclined at the incidence angle θ. The satellite heading angle α is the direction in which the satellite is pointed or oriented in space and is determined by the orientation of its sensors. The Fig. 1.1 represents the geometry of SAR imaging showing the incidence angle (θ) and heading angle (α). The study area is highlighted by a red rectangle.

Following (Fuhrmann & Garthwaite, 2019) the displacement in the LOS direction u_{LOS} can be calculated from the incidence angle θ and satellite heading angle α as

$$u_{\text{LOS}} = \begin{bmatrix} -\sin\theta\cos\alpha & \sin\theta\sin\alpha & \cos\theta \end{bmatrix} \begin{bmatrix} u_E \\ u_N \\ u_U \end{bmatrix}. \tag{3.1}$$

where u_E, u_N, and u_U are deformation in directions of East, North, and Up, respectively, that can be calculated by transforming the predicted deformation (Section 2.2) in the model coordinate system ($u = (u_x, u_y, u_z)$) to east-north-up (ENU) coordinate system. This transformation involves a rotation of 180° around the y-axis followed by a rotation of approximately 20° around the z-axis. Figure 3.7 depicts the model coordinate system in relation to the ENU reference frame.

Sentinel-1 SAR data offers a powerful and accessible tool for detecting and monitoring surface displacement over diverse landscapes and for various applications. In our calculations, we use Sentinel-1 ascending geometry values. During ascending satellite passes (flight direction NNW), the heading angle (α) is 15°. The incidence angle varies among SAR sensors based on factors like image extent (near-range vs. far-range) and image mode. For specific information on the incidence angle of the Interferometric Wide Swath (IWS) mode in Sentinel-1 data, please refer to European Space Agency (ESA) (2023). In our analysis, we assume an average incidence angle (43.86°) that represents all points in entire image.

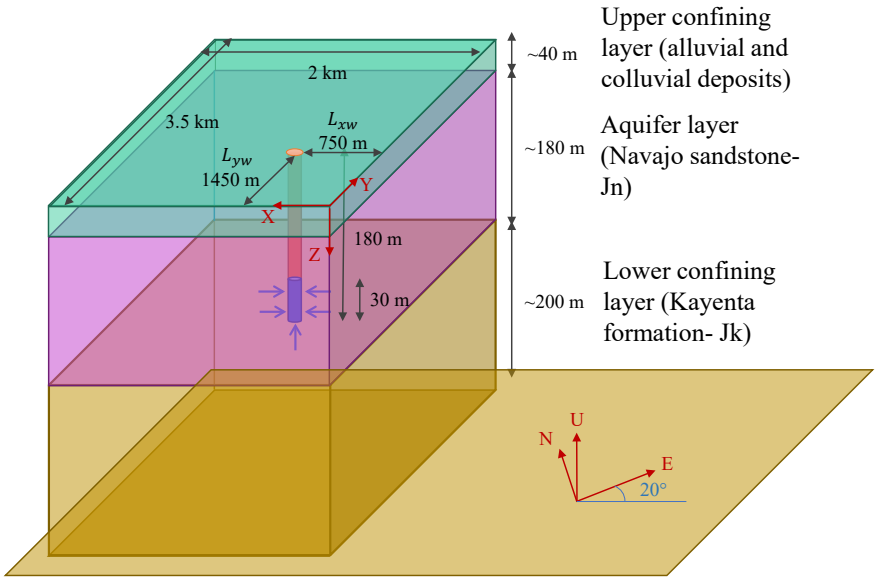

Figure 3.7: Simplified conceptual model of the Anderson Junction aquifer system showcasing the dimensions, names, formations, and thicknesses of the layers within the cross-section. The pumping well is accurately positioned and labeled in the 3D model. The figure also illustrates the model coordinate system in relation to the ENU global coordinate system. The domain is not to scale.

3.4 Conceptual model construction

In this section, we provide an overview of the model parameters and the boundary conditions that have been defined for the problem. We specify the simplifications and other assumptions that we use to model the Anderson Junction aquifer. We also detail the generation of the computational mesh that represents the physical domain, and describe the computational tools used for model implementation.

3.4.1 Aquifer model layers and parameters

Since the Anderson Junction aquifer is confined, two confining layers surround the main aquifer layer. These three layers are illustrated and described in the simplified conceptual model shown in Fig. 3.7.

We simplified the geological complexity by assuming horizontal layers for our aquifer model (Fig. 3.7). Acknowledging variations in the shape and thickness of each layer along the aquifer system, we opted for horizontal layers due to a lack of information about the height of layers throughout the aquifer system. Additionally, the aquifer's width and

Description	Symbol	Unit	Value
Fluid source	f_p	s^{-1}	0.0
Body force	f_u	$\mathrm{N\,m}^{-3}$	0.0
Specific weight of water	ρg	$\mathrm{N\,m}^{-3}$	9807
Pumping rate	P_r	$\mathrm{m}^3\,\mathrm{s}^{-1}$	0.07
Extraction rate	g_p	$\mathrm{m\,s}^{-1}$	1.9×10^{-3}

Table 3.1: Model parameters

Description	Symbol	Unit	Upper conf.	Aquifer	Lower conf.
Porosity	ϕ	-	10%	32%	8%
Biot coefficient	α	-	0.868	0.998	0.858
Specific storage	S_ε	Pa^{-1}	0.8×10^{-10}	1.5×10^{-10}	0.8×10^{-10}
Shear modulus	μ_s	Pa	7.7×10^{9}	5.06×10^{9}	7.9×10^{9}
Lame's first param.	λ	Pa	6.088×10^{9}	3.768×10^{9}	6.156×10^{9}
Hydraulic conductivity xx	k_{xx}	$\mathrm{m}^3\,\mathrm{s\,kg}^{-1}$	5×10^{-12}	1.1×10^{-8}	5×10^{-12}
Hydraulic conductivity yy	k_{yy}	$\mathrm{m}^3\,\mathrm{s\,kg}^{-1}$	5×10^{-12}	4.7×10^{-10}	5×10^{-12}
Hydraulic conductivity zz	k_{zz}	$\mathrm{m}^3\,\mathrm{s\,kg}^{-1}$	5×10^{-12}	5×10^{-7}	5×10^{-12}

Table 3.2: Material parameters of the layers.The Anderson Junction site is an extensional tectonic regime, which usually leads to more vertical than horizontal faults, thereby increasing the value of k_{zz}.

length were estimated based on the map of effective land subsidence due to groundwater depletion Herrera-García et al. (2021).

The simplified conceptual model of the aquifer system (Fig. 3.7), details the areal extent, names, formations, and thicknesses of the layers within the cross-section (Fig. 3.3). The pumping well has a total depth of 180 m, with the casing set at 150 m. The precise position (L_{xw} and L_{yw}) and depth of the pumping well are indicated in the 3D model (Fig. 3.7).

Table 3.1 and Table 3.2 present the model parameters and layer parameters, respectively, that are used in the finite element formulation. Each aquifer parameter is assigned a single value for the entire layer while recognizing the potential variations within the layer.

References to USGS books and maps, particularly (Marston & Heilweil, 2012; V. Heilweil et al., 2000), guided the establishment of boundary conditions in the Anderson Junction aquifer and provided details about the pumping test. Additionally, most of the

parameters of the Biot equations for the aquifer layer were extracted from various regional studies (Torabi et al., 2015; Cheng & Toksöz, 1979; Loope et al., 2020), and sandstone properties studies (Batzle et al., 2007; George et al., 2010; Molina et al., 2017).

The estimate for aquifer hydraulic conductivity was obtained from V. M. Heilweil & Hsieh (2006). In their work, the permeability of the porous medium was calculated, and we used the following equation to calculate hydraulic conductivity.

$$k = \frac{\kappa'}{\rho g}. \tag{3.2}$$

Here, k $\mathrm{m^3\,s\,kg^{-1}}$ is the hydraulic conductivity, κ' $\mathrm{m\,s^{-1}}$ is the specific permeability of the porous medium and ρg $\mathrm{N\,m^{-3}}$ is the fluid's specific weight.

For the confining layer properties we employ porosity-based estimation based on the findings in Dehghani et al. (2018). This method allows the estimation of confining layers properties by integrating approximate porosity data. Specifically, we used (Dehghani et al., 2018, Figure 5) for approximating the Biot coefficient, (Dehghani et al., 2018, Figure 7) for Biot's modulus, (Dehghani et al., 2018, Figure 8b) for Young's modulus, and (Dehghani et al., 2018, Figure 9) for the shear modulus. The average total porosity of the aquifer layer was derived from V. Heilweil et al. (2000). The assumed porosity of the confining layers were derived from studies on sandstone properties. Given that sandstone with low permeability typically exhibits porosity between 7 % and 10 % (Qi et al., 2022; Earle, 2019), we suppose the porosity of the upper confining layer to be 10 %. Additionally, considering the general trend of decreasing porosity and permeability with depth below the land surface (Herod, 2013), we assume the porosity of the lower confining layer to be 8 %. Dehghani et al. (2018) estimated poroelasticity parameters based on porosity, facilitating the estimation of confining layers parameters using these plots.

3.4.2 Boundary conditions

Two sets of boundary conditions are considered in this problem: fluid boundary conditions and solid boundary conditions. These boundary conditions are implemented to sufficiently represent the physical behavior and constraints on the system, i.e. the fluid

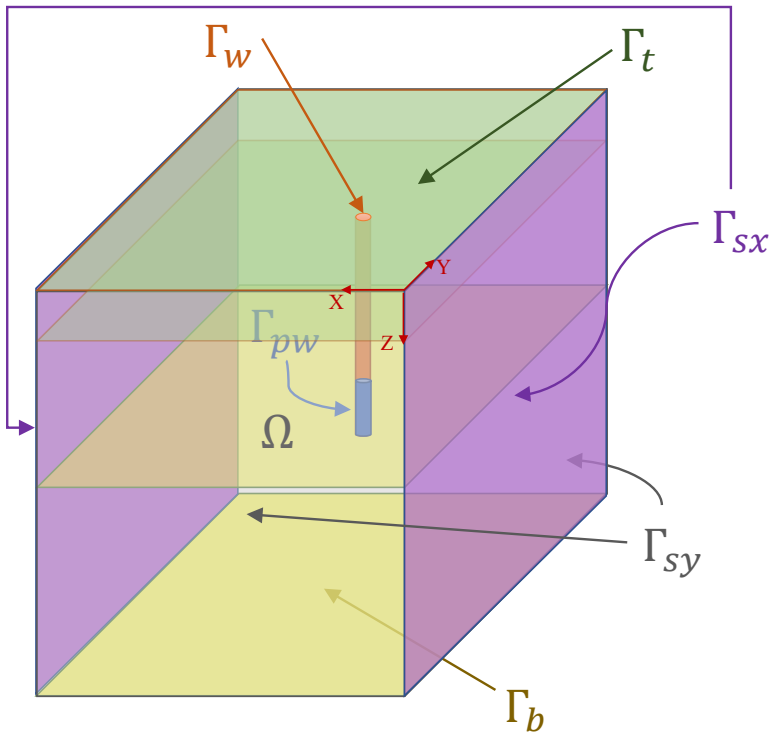

Figure 3.8: Aquifer model illustrating the domain and defined boundaries referenced in the Table 3.3, domain not to scale. Γ_b is the bottom boundary, Γ_t is the top boundary, Γ_{sx} is the two sides with normal facing in the x-direction, Γ_{sy} is two sides with normal facing in the y-direction, Γ_w is the well boundary from the surface until the end of the casing set, and Γ_{pw} is the screened area of the well boundary where water is pumped.

	Boundary condition	Boundary
Fluid problem (q, p)	$q \cdot n = 0$	$\Gamma_b \cup \Gamma_{sx} \cup \Gamma_{sy} \cup \Gamma_t \cup \Gamma_w$
	$q \cdot n = g_p$	Γ_{pw}
Solid problem (u)	$u = 0$	Γ_b
	$u_x = 0$	Γ_{sx}
	$u_y = 0$	Γ_{sy}
	$\sigma \cdot n = 0$	$\Gamma_t \cup \Gamma_{pw}$
	$u \cdot n = 0$	Γ_w

Table 3.3: Boundary conditions of fluid and solid problem. The boundary sets are defined in Fig. 3.8.

flow and deformation processes. Table 3.3 shows the boundary conditions for the state variables u (displacement), p (pressure), and q (flux). The boundaries referenced in the table are defined in Fig. 3.8.

In the study area and during the aquifer test period, precipitation was assumed to be negligible due to prevailing weather conditions. Consequently, we assumed no recharge through the top boundaries Γ_t. Although evapotranspiration as discharge was not low during this period, we considered it insignificant compared to the pumping rate. As a result, the fluid boundary at the top is treated as a no-flux boundary. The boundary conditions for the fluid problem assume no flux on the faces of the model domain Γ_b, Γ_{sx}, Γ_{sy}, and Γ_t) as described above. Additionally, no fluid flux is assumed at all other boundaries, excluding the pumping well boundary Γ_{pw}, where the extraction rate g_p is specified.

Given that the study area is not an urban area, the load on the top boundary Γ_t is considered negligible, so we assume the top boundary is traction-free. Recognizing the minimal displacement in the layers beneath the aquifer system and considering its negligible impact on the surface, we assume there is no displacement on the bottom boundary Γ_b. Therefore, the boundary conditions for the solid problem include: zero displacement at the bottom boundary Γ_b, zero normal displacement at the sides boundary (Γ_{sx}, Γ_{sy}) and well boundary Γ_w, and traction-free boundary conditions at the top surface Γ_t and at the pumping well boundary Γ_{pw}.

Enforcing no normal displacement at well boundary

We briefly describe the method by which we enforce the boundary condition on the normal component of the displacement $u \cdot n = 0$ on the well surface Γ_w as specified in Table 3.3. This boundary condition is recommended as being the most physically justifiable choice in Burbey (2006). By contrast, Alghamdi (2020) did not explicitly include the well surface in their model, instead choosing to model the extraction as a volume forcing using f_p.

Instead of building the boundary condition $u \cdot n = 0$ strongly into the space $\mathcal{U}$, we choose to enforce it weakly using a penalty-free non-symmetric Nitsche-type method proposed in Chouly et al. (2015). Our decision to enforce this condition weakly was made largely to ease the implementation in DOLFINx, where imposing boundary conditions of type $u \cdot n = 0$ strongly in the space is not straightforward.

For simplicity we did not include this more complex boundary condition when developing Eq. (2.21), instead choosing to enforce this by a modification to Eq. (2.21b) here. Following Chouly et al. (2015) we add two terms on the left-hand side of Eq. (2.21b)

$$\begin{aligned} &-(\bar{\sigma}(u^{n+1}, p^{n+1}), \nabla \tilde{u}) \\ &-(\bar{\sigma}(u^{n+1}, p^{n+1}) \cdot n, \tilde{u} \cdot n)_{\Gamma_w} + (\bar{\sigma}(\tilde{u}^{n+1}, \tilde{p}^{n+1}) \cdot n, u \cdot n)_{\Gamma_w} \\ &\qquad = -(f_u^{n+1}, \tilde{u}) - (g_u^{n+1}, \tilde{u})_{\Gamma_u^n}, \quad \forall \tilde{p} \in \mathcal{P}_0, \forall q \in \mathcal{Q}_0. \end{aligned} \tag{3.3}$$

that weakly enforce the condition $u \cdot n = 0$ on Γ_w.

3.4.3 Main modeling assumptions

We briefly discuss the main modeling assumptions and their justification. Our modeling approach is a parsimonious one, prioritising model simplicity over capturing all possible features of the real Anderson Junction site.

As in Burbey (2006), we assume a purely elastic deformation of the skeleton, i.e. no inelastic deformation. This is an acceptable assumption in the context of a single constant pumping cycle (as opposed to cyclic and/or pulsed pumping), however, this elasticity assumption may be invalid if we wanted to simulate subsidence across multiple seasons and using more complex pumping regimes.

We assume that seasonal recharge and evapotranspiration is zero; for this site this is

a valid assumption if the pumping test occurs during the summer months due to the cold semi-arid (steppe) climate (BSk - Köppen type system).

Our boundary condition on the capped well boundary Γ_{pw} is zero normal component of the displacement, which in a cylindrical coordinate system would be equivalent to zero radial displacements. The physicality of this boundary condition is discussed in Burbey (2006); in summary, it is likely that displacements near the well boundary are inaccurate due to localized effects such as sand grains near the well screen not being radially constrained during strong pumping. Consequently, the displacements and flux patterns given by the simulation in the region immediately around the well should be considered as indicative or approximate, rather than precise.

We do not model the fluid flow through fractures in our model explicitly, e.g. Berre et al. (2019), but instead incorporate their dominating effect on the fluid flow through the anisotropic hydraulic conductivity tensor. In the broader context of data assimilation, it is unlikely that SAR or GPS displacement data could be sufficiently informative to constrain information about microstructural features such as individual fracture paths. Further on this point of information content, we remark that Alghamdi (2020) demonstrated that SAR data is not informative about the variability of hydraulic conductivity in the vertical (z) direction. With this limited information content in mind, we also assume that the global anisotropic behaviour of the model is in the fluid problem, allowing us to assume that the solid problem is isotropic. This is the same assumption used in Burbey (2006).

3.4.4 Mesh generation

The geometry of the model was meshed using gmsh (Geuzaine & Remacle, 2009) for finite element analysis. The resulting 3D mesh, as shown in Fig. 3.9, represents the aquifer system's three layers. The element size varies from 6 to 40 m, and the total number of the elements is 368 329. The mesh incorporates different element sizes at different locations and in different layers, this will ensure an appropriate resolution that will improve the accuracy of the model. As we approach the well, the mesh elements become finer, enabling the capture of localized effects with higher precision. Figure 3.9 highlights the relative positions of the pumping and observation wells in the model. The

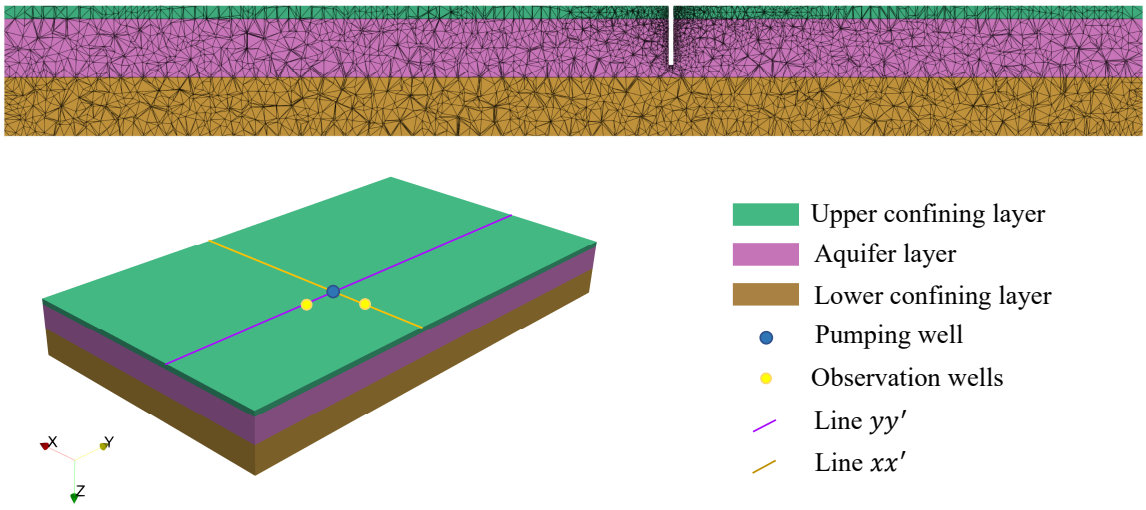

Figure 3.9: Generated 3D mesh of the aquifer system illustrating the three layers and their element sizes. The 2D mesh shown at the top represents a vertical cross-section of the 3D mesh, aligned with the y-axis and intersecting the pumping well. The figure also highlights the positions of the pumping and observation wells, as well as lines xx' and yy'. The xx' line extends from $x = 0\,\text{m}$ to $x = 2000\,\text{m}$, passing through the pumping well and aligned with the x-axis, while the yy' line extends from $y = 0\,\text{m}$ to $y = 3500\,\text{m}$, also passing through the pumping well and aligned with the y-axis.

two lines xx' and yy' will be used later to present the model output graphically.

3.5 Results and discussion

In this section, we report the deformation and flux of our simulations for the Anderson Junction case study. In addition to the constraints from the actual pumping test, we explore higher pumping rate and longer pumping times to determine what conditions would allow for detection of surface displacements using the InSAR technique. We also conduct simulations with different conductivity anisotropy ratios to investigate their effects on surface displacement.

3.5.1 Simulation of the Anderson Junction pumping test

In this section, we simulate the Anderson Junction pumping test using our FEM model outlined in Section 3.4 and the parameters provided in Table 3.1 and Table 3.2 to estimate the deformation u, pressure p and flux q within the aquifer system.

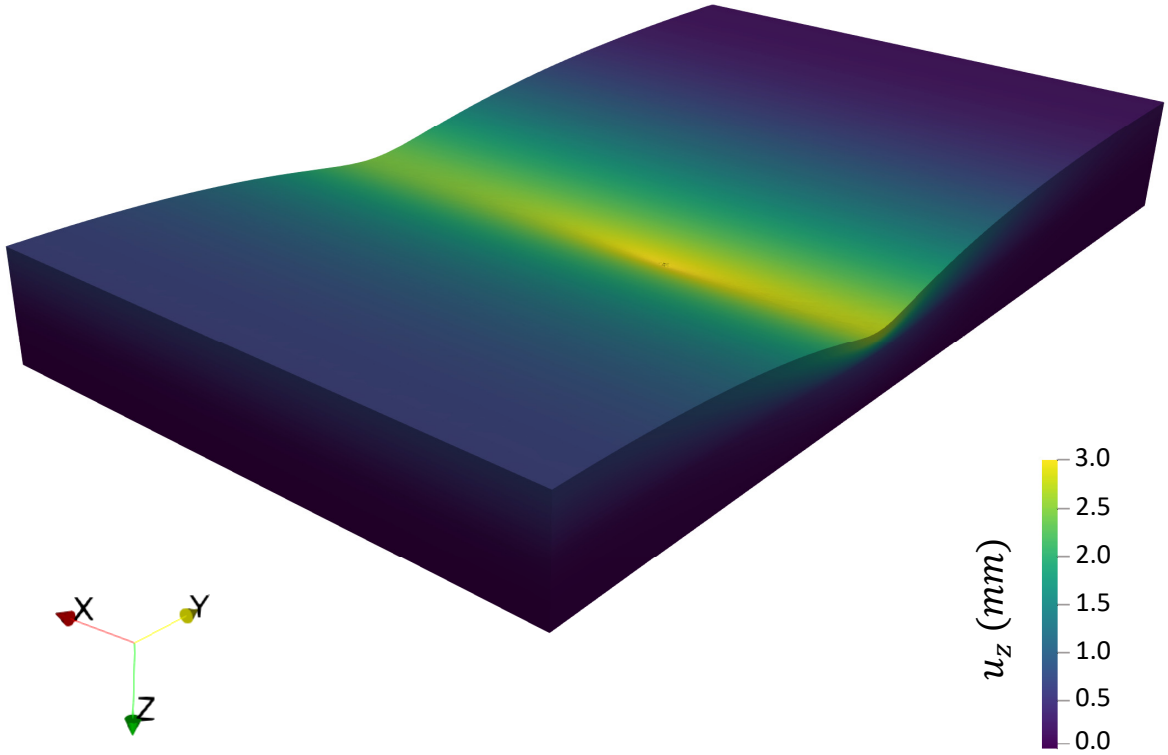

Figure 3.10: Magnified visualization of aquifer displacement after four days of pumping, showcasing the detailed shape of the displacement. The displacement is magnified approximately 70,000 times, allowing for enhanced visualization of the fine-scale features.

Figure 3.10 shows the aquifer displacement after four days of pumping, magnified 70 000 times to visualize the detailed shape of the displacement. The areas close to the pumping well exhibit displacements on the order of 3 mm. The larger vertical displacements in the x direction (versus the y direction) are driven by the higher hydraulic conductivity that we imposed in the x direction. This would allow us to observe the impact of AHC on the surface displacement pattern.

Figure 3.11 shows the flux evolution (from the onset of pumping to the end of observations at 24 d of the experiment) for both the xx' and yy' cross sections across the three layers of the model. The arrows indicate the direction and magnitude of the flow within and among the layers. The higher flux values close to the pumping well are a response to the higher pressure gradient set up by the pumping. The downward arrows near the well in the Fig. 3.11a represent the fluid flux near the well boundary (Γ_w) because of the no normal flux boundary condition applied in this boundary. As the test progresses into the relaxation phase (4 d to 24 d), the magnitude of flux arrows reduces.

3.5.2 The effect of anisotropy ratio on the surface displacement

We begin by conducting simulations with varying anisotropy ratios to explore their impact on the resulting surface displacement. Figure 3.12 presents the surface displacement for three simulated scenarios at three times through the pumping phase. The scenarious are IHC with $k_{xx} = k_{yy} = 0.6 \times k_{yy}^{AJ}$; AHC with a 3:1 anisotropy ratio, similar to the anisotropy observed in Burbey et al. (2006); Burbey (2006), where $k_{xx} = 3 \times 1.7 \times k_{yy}^{AJ}$ and $k_{yy} = 1.7 \times k_{yy}^{AJ}$; and AHC with an anisotropy ratio of about 24:1, representative of the Anderson Junction aquifer, where k_{xx}^{AJ} and k_{yy}^{AJ} are hydraulic conductivity from V. M. Heilweil & Hsieh (2006) (in Table 3.2). We selected the scaling values for k_{xx} and k_{yy} to achieve a similar range of displacements between the scenarios, making comparison easier. The hydraulic conductivity in the z direction remains constant across all scenarios at $k_{zz} = 5 \times 10^{-7}$.

Figure 3.13 presents a comparison of these scenarios along line xx' and line yy' at the end of the pumping period (T_p). As Fig. 3.12 shows, the outcomes of these simulations reveal distinct patterns in surface displacement. The IHC scenario exhibits circular surface

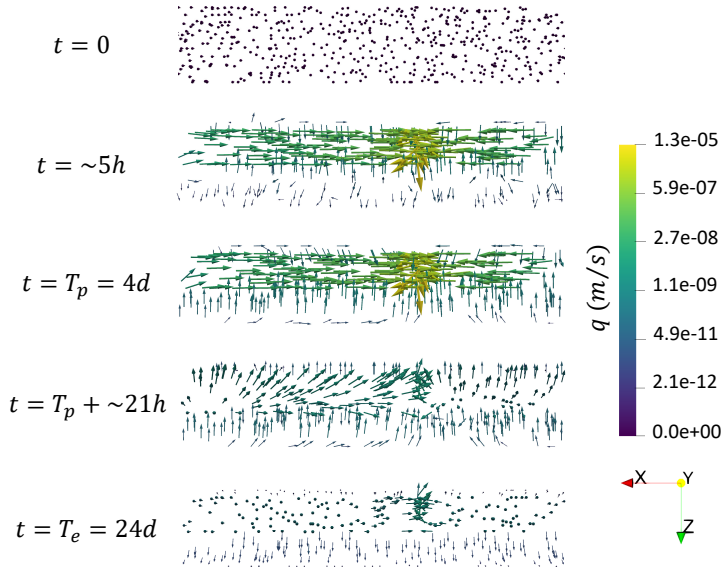

(a) Visualization of the flux on a cross-section intersecting the line xx' with normal pointing in the y-direction.

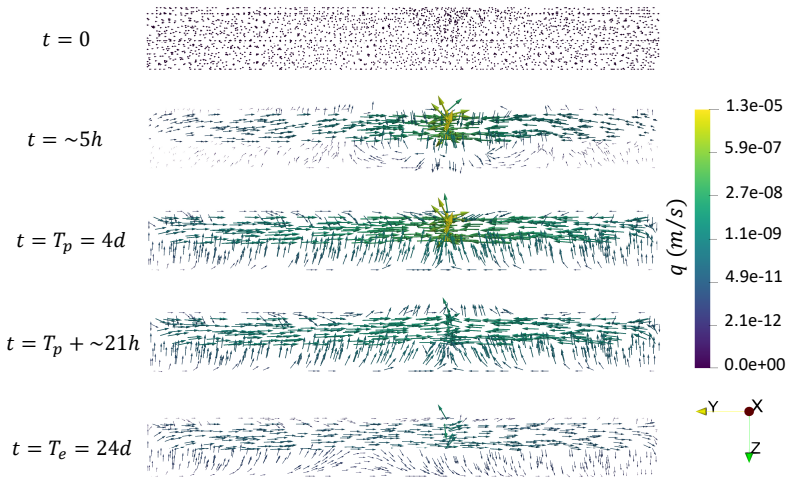

(b) Visualization of the flux on a cross-section intersecting the line yy' with normal pointing in the x-direction.

Figure 3.11: Flux distribution at different times for (a) a cross-section intersecting the line xx' with normal pointing in the y-direction and (b) a cross-section intersecting the line yy' with normal pointing in the x-direction. The figure illustrates the flux generation process across the upper confining layer, aquifer layer, and lower confining layer over 4 days of pumping followed by a 20 day relaxation phase. The magnitude of the arrow represents the logarithm of the flux value and the color bar shows the actual predicted flux.

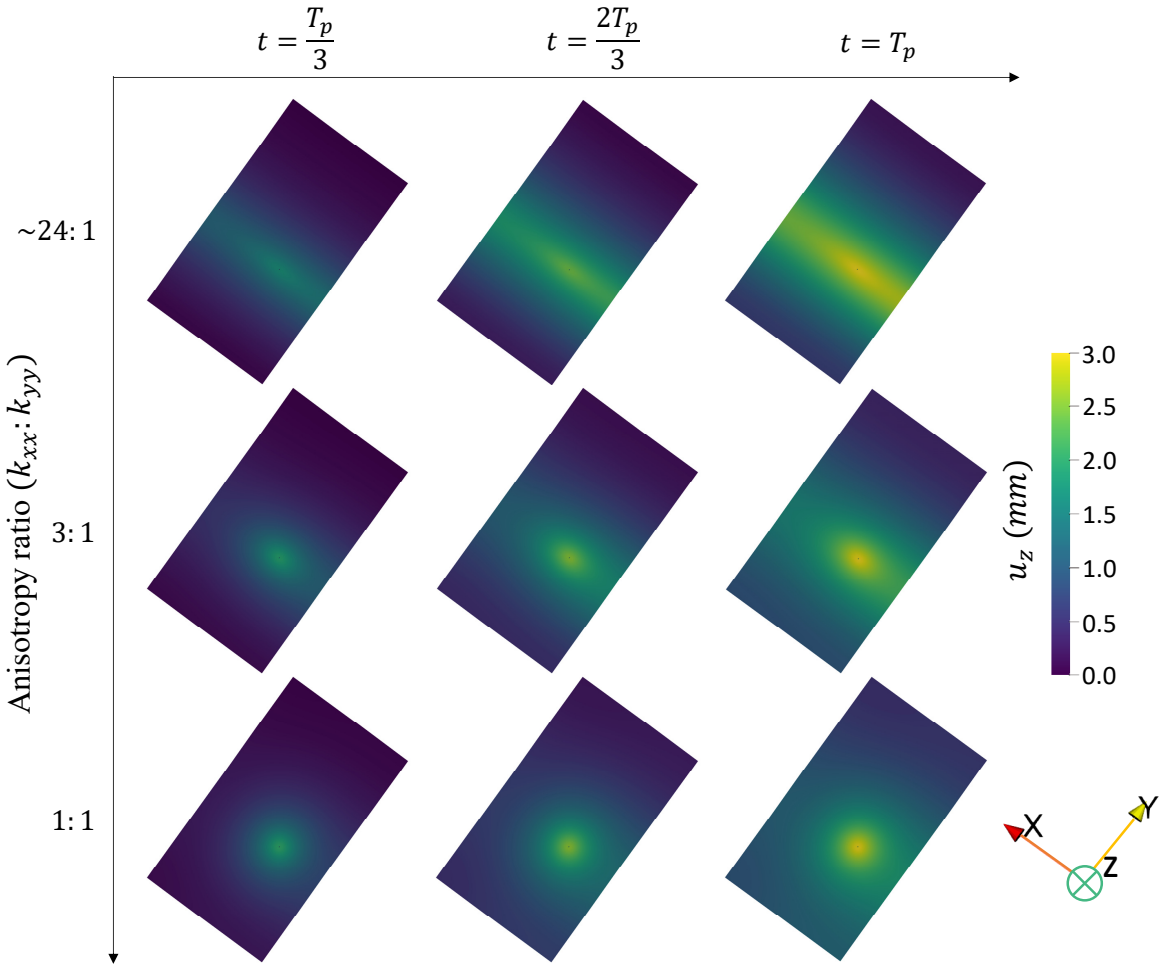

Figure 3.12: Surface displacement for three simulated scenarios: IHC, AHC with a 3:1 anisotropy ratio, and AHC with an anisotropy ratio of approximately 24:1. The images display the surface displacements at three times during the pumping phase.

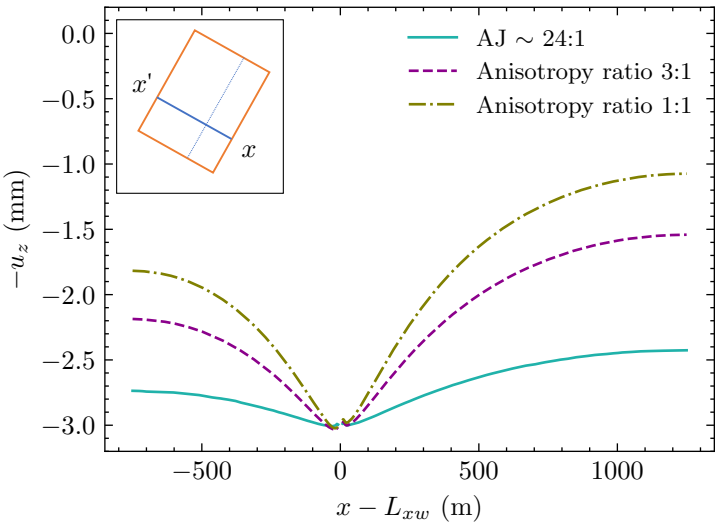

(a) Negative vertical surface displacement along xx'

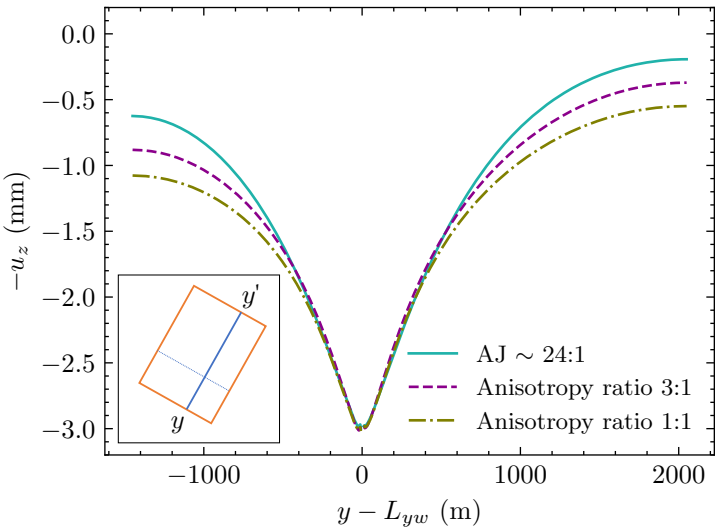

(b) Negative vertical surface displacement along yy'

Figure 3.13: Negative vertical surface displacement ($-u_z$) for three simulated scenarios: IHC, AHC with a 3:1 anisotropy ratio, and AHC with an anisotropy ratio of approximately 24:1. The graph displays the surface displacements along line xx' and line yy' at the end of pumping (T_p).

displacement, indicating a relatively uniform distribution of deformation. In contrast, the AHC simulations demonstrate elliptical surface displacement. Notably, the greater the disparity between the principal hydraulic conductivity values in the x-direction (k_{xx}) and the y-direction (k_{yy}), corresponding to higher anisotropy ratios, the more pronounced the elliptical shape of the surface displacement becomes.

3.5.3 Possibility of using InSAR to determine AHC in aquifers

In this section, we aim to ascertain whether the surface displacement resulting from our model of the Anderson Junction aquifer pumping test can be detected using InSAR. Additionally, we explore the scenario of higher pumping rates or a longer duration of pumping to understand if such conditions could lead to observable surface displacements with InSAR.

As explained in Section 3.3, successful detection of surface displacement using Sentinel-1 InSAR requires displacements exceeding 8 mm along the LOS within a specific region around the well, e.g. an elliptical displacement pattern that demonstrates AHC. Figure 3.14 illustrates the surface displacement along line xx' and yy' at various time points. It is evident that the maximum surface displacement is only 3 mm. Consequently, under our conceptual model assumptions the magnitude of the surface displacements created during the original Anderson Junction test described in V. M. Heilweil & Hsieh (2006) was likely insufficient to be detected by Sentinel-1 InSAR.

Despite this negative result, the model gives us a tool to explore under which scenarios a future test at Anderson Junction could produce a sufficient response detectable by InSAR and containing potentially valuable information for inferring AHC. To this end, we explored three alternative scenarios. For reference in the following discussion, the LOS surface displacement under the original Anderson Junction test conditions is shown in Fig. 3.15.

In the first scenario, *high pumping rate*, shown in Fig. 3.16a we increase the pumping rate to eight times the value used in the original Anderson Junction test, while keeping the pumping duration fixed. The maximum line of sight displacement increased to 18 mm (detectable by InSAR) and the displacement pattern has a strong elliptical character.

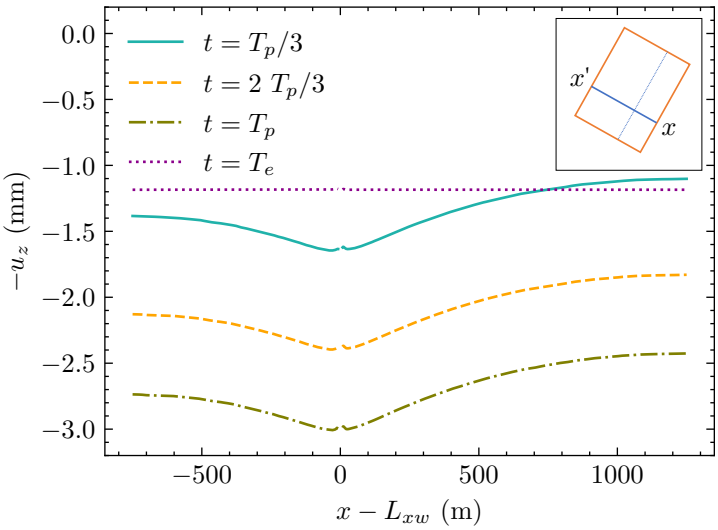

(a) Negative vertical surface displacement along xx'

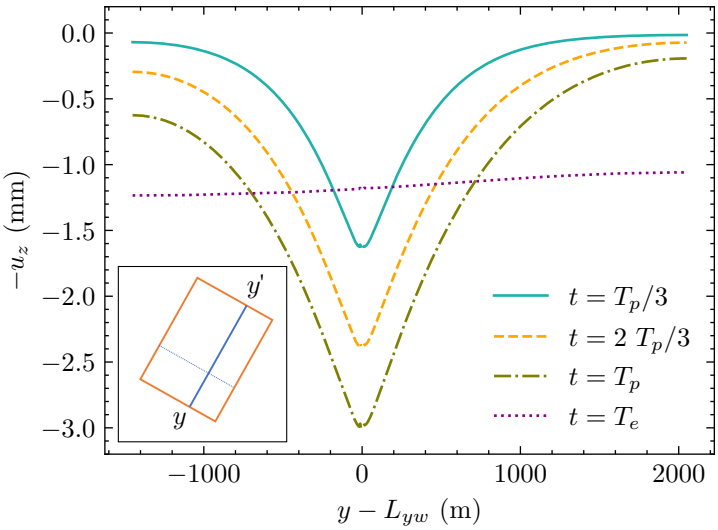

(b) Negative vertical surface displacement along yy'

Figure 3.14: Negative vertical surface displacement along line xx' and line yy' at different time points. The results, obtained using the poroelastic model, demonstrate that the maximum predicted surface displacement during the Anderson Junction aquifer test reaches 3 mm.

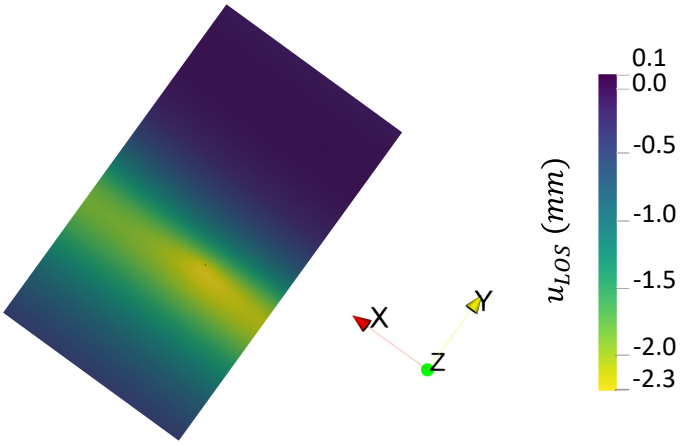

Figure 3.15: Simulated LOS surface displacement at the end of pumping for Anderson Junction test (4 d, P_r). Note the different colorbar scale to Fig. 3.16.

In the second scenario, *long pumping duration*, shown in Fig. 3.16b, we increase the pumping time to 32 d and keep the pumping rate the same as that used in the original Anderson Junction test. The maximum line of sight displacement is significantly lower than the first scenario at 8.6 mm, although still potentially at the threshold for detection by Sentinel-1 InSAR. Additionally, the longer pumping has led to a significantly more diffuse and isotropic displacement response than in the high pumping rate scenario. This can be attributed to the longer pumping having sufficient time to activate the slower diffusion timescale of the fluid problem along the minor axis y.

Finally, we show an *intermediate rate and duration* scenario, shown in Fig. 3.16c with eight days of pumping and four times the pumping rate of the original Anderson Junction test. This scenario is a compromise between the high pumping rate scenario Fig. 3.16a and the long pumping rate scenario Fig. 3.16b. We can see that a strong elliptical LOS displacement pattern is visible and that the maximum displacement at 13.3 mm exceeds the threshold for detection by Sentinel-1 InSAR. Note that by design the total water extracted

$$Q = \int_0^{T_p} \int_{\Gamma_{pw}} g_p \, \mathrm{d}x \, \mathrm{d}t, \tag{3.4}$$

is the same in the three scenarios.

Figure 3.17 presents a comparison of LOS surface displacement for the different scenar-

ios along line xx' and yy'. Notably, the graph shows that along line yy', the high pumping rate causes substantial surface displacement gradients around the pumping well, which could result in sinking and fissure formation (Galloway et al., 1999, p. 132–133) (although, our model cannot predict this type of localized process directly).

We conclude that in terms of maximising the potential information content with respect to inferring possible anisotropy, it is important to strongly perturb the system via the pumping rate to ensure that the anisotropic character is visible *and* to pump a sufficient volume of water such that the LOS surface displacement can be detected by the chosen InSAR technology. However, it is important to note that there are practical limitations to how much we can increase the pumping rate or pumping duration, as they must align with the aquifer's properties, sustainability considerations and engineering considerations, see e.g. (Osborne, 1993) for a discussion.

3.5.4 The required aquifer test features for using InSAR Data

In assessing the potential utility of SAR data for studying an aquifer system undergoing an aquifer test, several key considerations need to be taken into account, including the availability of data, the temporal resolution of SAR mission, and accuracy of surface displacement measurements. The temporal resolution of the SAR data is important in case of acquiring more SAR data around the aquifer test time. We need at least one suitable pair of InSAR data within the aquifer test interval like in Alghamdi (2020) study, although having multiple data points within a longer test interval can enhance the understanding of the aquifer system. Moreover, it is crucial to assess whether the surface displacement caused by the aquifer test is observable through InSAR techniques. Therefore this is one of our motivations to build the proposed model to predict the surface displacement in the Anderson Junction aquifer.

To ensure the feasibility of using SAR data to estimate aquifer properties, three key considerations should be taken into account for the aquifer test:

1. Availability of SAR data: It is essential to confirm the availability of SAR datasets specifically for the time and location of the aquifer test.

2. Adequate test interval: The aquifer test should have a sufficiently long time in-

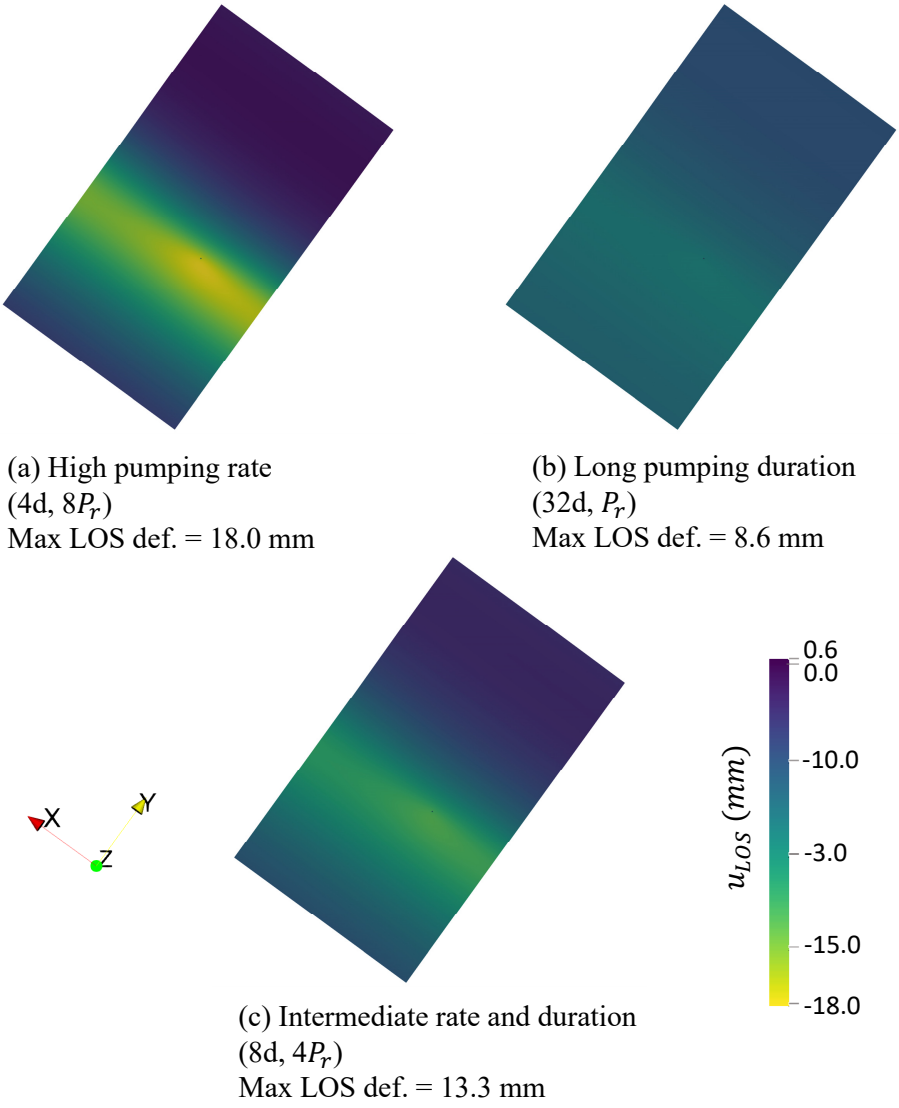

(a) High pumping rate
(4d, $8P_r$)
Max LOS def. = 18.0 mm

(b) Long pumping duration
(32d, P_r)
Max LOS def. = 8.6 mm

(c) Intermediate rate and duration
(8d, $4P_r$)
Max LOS def. = 13.3 mm

Figure 3.16: Simulated LOS surface displacement at the end of pumping for: (a) an 8 times pumping rate compared to the Anderson Junction test. (b) an extended pumping duration of 32 d, replicating the aquifer test characteristics of Anderson Junction (c) an extended intermediate pumping with 4 times rate and 8 d duration. In all cases, the total volume of extracted groundwater is the same. Note the different colorbar scale to Fig. 3.15.

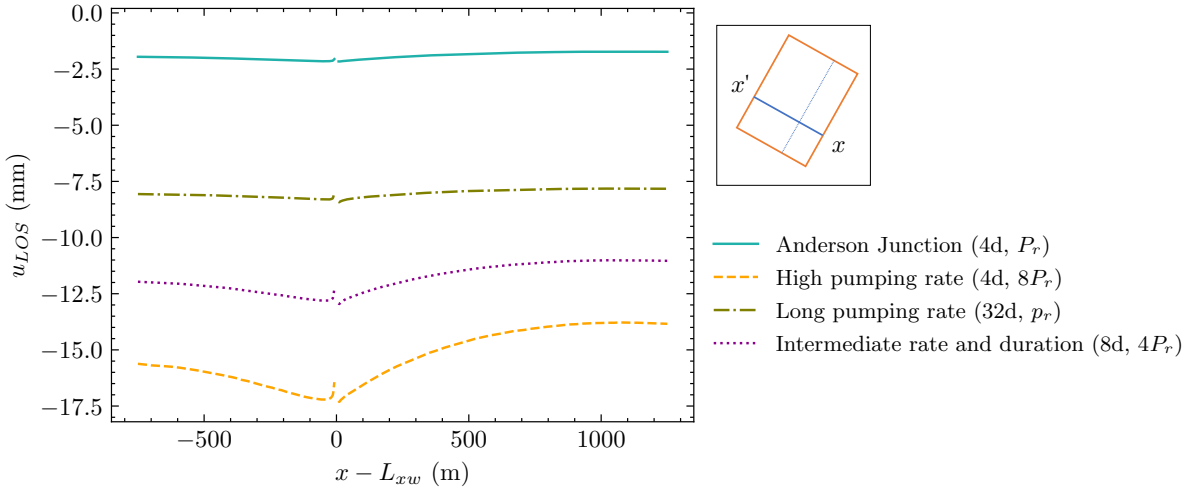

(a) LOS surface displacement along xx'

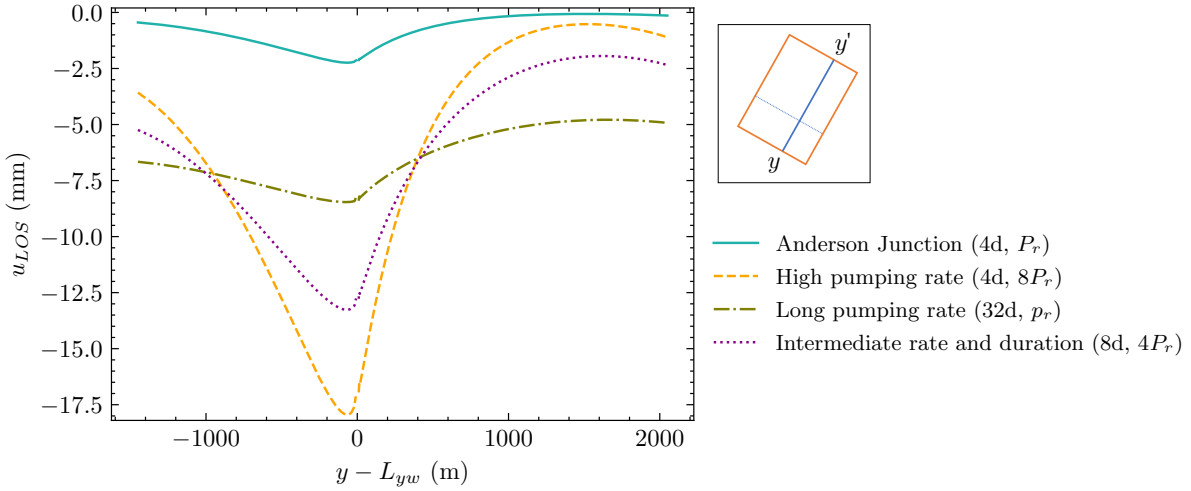

(b) LOS surface displacement along yy'

Figure 3.17: Comparison of LOS surface displacement along line xx' and line yy' at the end of pumping (T_p) for different pumping scenarios. Along yy', excessive pumping leads to significant surface displacement, which could lead to sinking and the formation of fissures near the pumping well (Galloway et al., 1999, p. 132–133).

terval. This allows for the collection of multiple SAR data sets, enabling a more comprehensive study of the aquifer over time.

3. Sufficient LOS displacement: The observed LOS displacement should exceed a minimum threshold, ideally more than 5 mm and preferably 8 mm or more (Cigna et al., 2021) if we want to use Sentinel-1 mission otherwise, we need to check the surface displacement accuracy of the SAR mission. For this purpose, we use the proposed model to predict the LOS surface displacement to compare with the SAR accuracy.

The guideline for conducting an aquifer test involves several key considerations to ensure accurate results and meaningful analysis. One important aspect is determining the appropriate pumping rate for the specific aquifer under investigation. The pumping rate should be selected based on the aquifer's properties, including its transmissivity, storage coefficient, and permeability, among others (Osborne, 1993). It should be set at a level that allows for effective characterization of the aquifer's hydraulic behavior while avoiding excessive drawdown or other undesirable effects.

After selecting the pumping rate, the pumping duration should be carefully chosen to allow for significant and measurable changes in the aquifer, enabling the detection of anisotropic elliptical patterns through InSAR. In addition, we cannot simply pump groundwater indiscriminately; rather, we must carefully consider both the aquifer properties and the project's budget constraints, as extended pumping may increase operational costs.

3.6 Conclusions

We have developed an anisotropic poroelastic finite element model of the Anderson Junction site that is capable of predicting coupled fluid flow and displacements. Our results show that the effective elastic response of the aquifer at the Earth's surface has an anisotropic nature driven by the underlying anisotropy in the fluid problem, even when the elasticity problem is assumed to be isotropic. In the LOS displacement this anisotropy manifests in distinctive elliptical patterns.

Under our model assumptions, the original Anderson Junction aquifer test described

in (V. M. Heilweil & Hsieh, 2006) probably did not exhibit sufficient surface displacement for detection using InSAR. In three alternative scenarios we explored longer and/or stronger pumping rates to explore the potential of using InSAR data to calibrate aquifer models with AHC – in two of these scenarios, Fig. 3.16a and Fig. 3.16c we predict LOS displacement levels necessary for detection by the contemporary Sentinel-1 InSAR mission. We add that the proposed model can be adapted to another aquifer test with a longer and/or stronger pumping rate or another confined aquifer system by changing the properties of the aquifer. It is also recommended to conduct extended pumping duration to gather InSAR data from multiple satellite passes.

Our upcoming research will explore two directions. First, due to uncertainty in the hydraulic conductivity tensor, we want to develop a stochastic model of AHC that respects the underlying material symmetries, e.g. (Cowin & Doty, 2007, Chapter 5). Second, with this stochastic model developed, we plan to assimilate InSAR-derived data into our aquifer model. This entails collecting field and remote sensing data to assess aquifer discharge and recharge dynamics. InSAR will offer valuable insights into surface displacement and underlying aquifer structures. By solving the inverse problem using spatiotemporal data, we aim to estimate aquifer properties following e.g. Alghamdi et al. (2020, 2021). These investigations promise to significantly advance our understanding of aquifer with AHC behavior leading to models with improved predictive power for use in a groundwater management context.

Acknowledgments

We would like to thank Natascha Kuhlmann from the University of Bonn for her assistance in interpreting the geologic maps and providing insights into the geological characteristics of the study area. We would also like to thank Hamid Dehghani from the Luxembourg Institute of Science and Technology (LIST) for his guidance selecting appropriate poroelastic constants.

Funding

This work was funded in whole, or in part, by the Luxembourg National Research Fund (FNR), grant reference PRIDE/17/12252781. For the purposes of open access, and in fulfilment of the obligations arising from the grant agreement, the authors have applied a Creative Commons Attribution 4.0 International (CC BY 4.0) license to any Author Accepted Manuscript version arising from this submission.

Supplementary material

The supplementary material (Salehian Ghamsari & Hale, 2025) includes code, input data and mathematical details of the finite element solver alongside a Docker container to execute the code in. We have also included a video version of Fig. 3.10 showing the deformation of the Anderson Junction simulation.

Code availability section

AHC-Poroelastic-Model

Contact: salehiyan.sona@gmail.com.

Hardware requirements: x86-64 or ARM computer with container runtime e.g. Docker.

Program language: Python

Software required: Python, Paraview with Python interface (pvpython), Docker, DOLFINx.

The source code and Docker image are available for download at (Salehian Ghamsari & Hale, 2025) and at https://github.com/sonaselehian/ahc-poroelastic-model.

Chapter 4

A random model of anisotropic hydraulic conductivity tailored to the InSAR-based analysis of aquifers

The content of this chapter is based on the following paper.

Salehian Ghamsari, S., van Dam, T., and Hale, J. S. (2025). "A random model of anisotropic hydraulic conductivity tailored to the InSAR-based analysis of aquifers" [preprint], `https://hdl.handle.net/10993/65440`

Authorship statement

Sona Salehian Ghamsari: Data curation, Methodology, Software, Formal analysis, Investigation, Writing - Original Draft, Validation, Visualization. Tonie van Dam: Writing - Review & Editing, Funding acquisition, Supervision. Jack S. Hale: Conceptualization, Methodology, Software, Investigation, Writing - Original Draft, Writing - Review & Editing, Funding acquisition, Project administration, Supervision.

Abstract

Sustainable aquifer management depends on reliable predictive models calibrated against diverse sources of data. Poroelastic coupling between fluid flow and surface displacement in an aquifer indicates that precise Interferometric Synthetic Aperture Radar (InSAR) displacement observation can be used to calibrate lateral hydraulic conductivity values within an aquifer. While previous Bayesian inference approaches to this problem have assumed isotropic random models for the hydraulic conductivity, many aquifers are characterized by strong anisotropic hydraulic conductivity (AHC). Consequently, isotropic models are in many cases inadequate. Leveraging a recently proposed Lie group approach for constructing random symmetric positive definite matrices, we propose a new random model for describing AHC in aquifer systems that can incorporate directional information from complex and potentially multi-modal structural geological data. We apply this methodology to describing two conceptual states of uncertainty regarding the 1996 Anderson Junction aquifer pump test where both multi-modal circular fracture outcrop and AHC principal magnitude data is available. After calibration against this data, the induced uncertainty in AHC is propagated through a partial differential equation-based conceptual model of the test. Our results show that the proposed methodology provides a flexible tool for modeling the effect of uncertain anisotropic hydraulic conductivity on InSAR-measurable surface displacements. Complete open source scripts using the DOLFINx finite element solver and numpyro/JAX are given as supplementary material.

4.1 Introduction

Water extracted from aquifers is essential for drinking water, agriculture and industry (Food and Agriculture Organization of the United Nations (FAO), 2022). However over-exploitation presents a major threat to sustainability (Basu & Van Meter, 2014; Caretta et al., 2022), with adverse consequences including land subsidence (V. M. Heilweil & Hsieh, 2006; Burbey et al., 2006; Galloway & Burbey, 2011), reduced water avail-

ability (Walker et al., 2020) and salt water intrusion (Q. Guo et al., 2019). Therefore, water management, supported by predictive computational models calibrated against all available data sources, is an important part of ensuring the future sustainability of the Earth's water resources (Singh, 2014; Amitrano et al., 2014).

In recent years, the remote sensing methodology InSAR has become popular for acquiring data about ground surface displacements due to its wide spatial coverage, cost-effectiveness and non-invasive nature (Massonnet & Feigl, 1998; Tomás et al., 2014). Because the coupling between the solid skeleton of the sedimentary rocks and the fluid flowing through the aquifer's pores, it has been proposed (Burbey et al., 2006; Burbey, 2006; Alghamdi, 2020) that geodetic surface displacement data derived from methodologies such as InSAR and GPS may contain valuable information for inferring the lateral hydraulic conductivity field of an aquifer.

Focusing on work exploring inverse problems and surface displacment data for inferring aquifer hydraulic conductivity, a series of recent papers (Hesse & Stadler, 2014; Alghamdi et al., 2020, 2021, 2024) introduced a scalable Bayesian inversion framework that uses a log–Gaussian process prior model (Tarantola, 2005; Fernández-Martínez et al., 2013) to infer from a heterogeneous *isotropic* hydraulic conductivity field from InSAR displacement data. However, in many aquifers the hydraulic conductivity exhibits anisotropy due to networks of lower scale flow-promoting features such as cracks and faults (Hurlow, 1998; Berre et al., 2019). In the subjective Bayesian approach to inverse problems (Tarantola, 2005) the choice of prior is critical in drawing conclusions from the posterior, after incorporating data via the likelihood. Consequently, the isotropic prior model imposed on the hydraulic conductivity field in Alghamdi et al. (2020, 2021, 2024) may be a unsuitable when field studies indicate that flow at the site is likely anisotropic (Pollard & Fletcher, 2005).

In Salehian Ghamsari, Dam, & Hale (2025) we investigated the link between aquifer AHC and InSAR derived surface displacements by constructing a poroelastic PDE-based model of the Anderson Junction aquifer test, which was determined be strongly anisotropic during a pump test described in V. M. Heilweil & Hsieh (2006). We used forward modeling to determine that site-scale AHC would lead to distinctive elliptical displacement patterns at the surface that, with correct pump test conditions, could be

detected using InSAR. Consequently, our hypothesis is that InSAR data contains valuable information for inferring AHC and that it is necessary to develop random models of AHC tailored for InSAR-based aquifer analysis. To address this gap, in this paper we develop a random model on the AHC tensor that could be used as a prior in a subjective Bayesian inference setting to assimilate InSAR data. In the following paragraphs, we outline the key points of and justification for our development using the Anderson Junction pumping test described in V. M. Heilweil & Hsieh (2006) as a foundational element.

In the original study (V. M. Heilweil & Hsieh, 2006) describing the Anderson Junction aquifer pumping test, the authors proposed a modified Papadopulus method (Papadopulos, 1965) to infer the magnitude of the hydraulic conductivity in the direction of two pressure observation wells *assumed* to be aligned with the principal directions of AHC[1]. V. M. Heilweil & Hsieh (2006) used the predominant fracture azimuths determined from a circular histogram which we reproduce (rose diagram in Fig. 1) to decide where the observation wells should be drilled. The fracture data reveals two nearly-orthogonal primary directions – consequently well A was drilled approximately along the direction of the first principal direction (x direction). Well B was drilled orthogonal to x (y direction), a constraint imposed by the modified Papadopulus method rather than in the statistically determined direction (more on this below). After observing the pressure drop data and calculating the two principal hydraulic conductivities, the major and minor directions were assigned to the x and y directions, respectively.

There are limitations to the analysis of the fracture data in V. M. Heilweil & Hsieh (2006). Firstly, as noted by V. M. Heilweil & Hsieh (2006), the principal direction is inherently uncertain and so if well A is not in fact aligned with the principal direction, then this directional uncertainty will introduce further uncertainty in the inferred principal values of the anisotropic hydraulic conductivity. This fact supports the motivation for developing a random model that can represent uncertainty in the principal direction. Secondly, although V. M. Heilweil & Hsieh (2006) indicate that it is 'neither necessary (nor warranted) to assume which is the major and which is the minor principal direction at the start of the analysis', it is not always the case that there are two or more nearly

[1]In the original Papadopulos (1965) method no assumption is made on the alignment of the wells with respect to the principal directions of AHC thus a minimum of three, rather than two, observation wells are required to uniquely determine the AHC tensor.

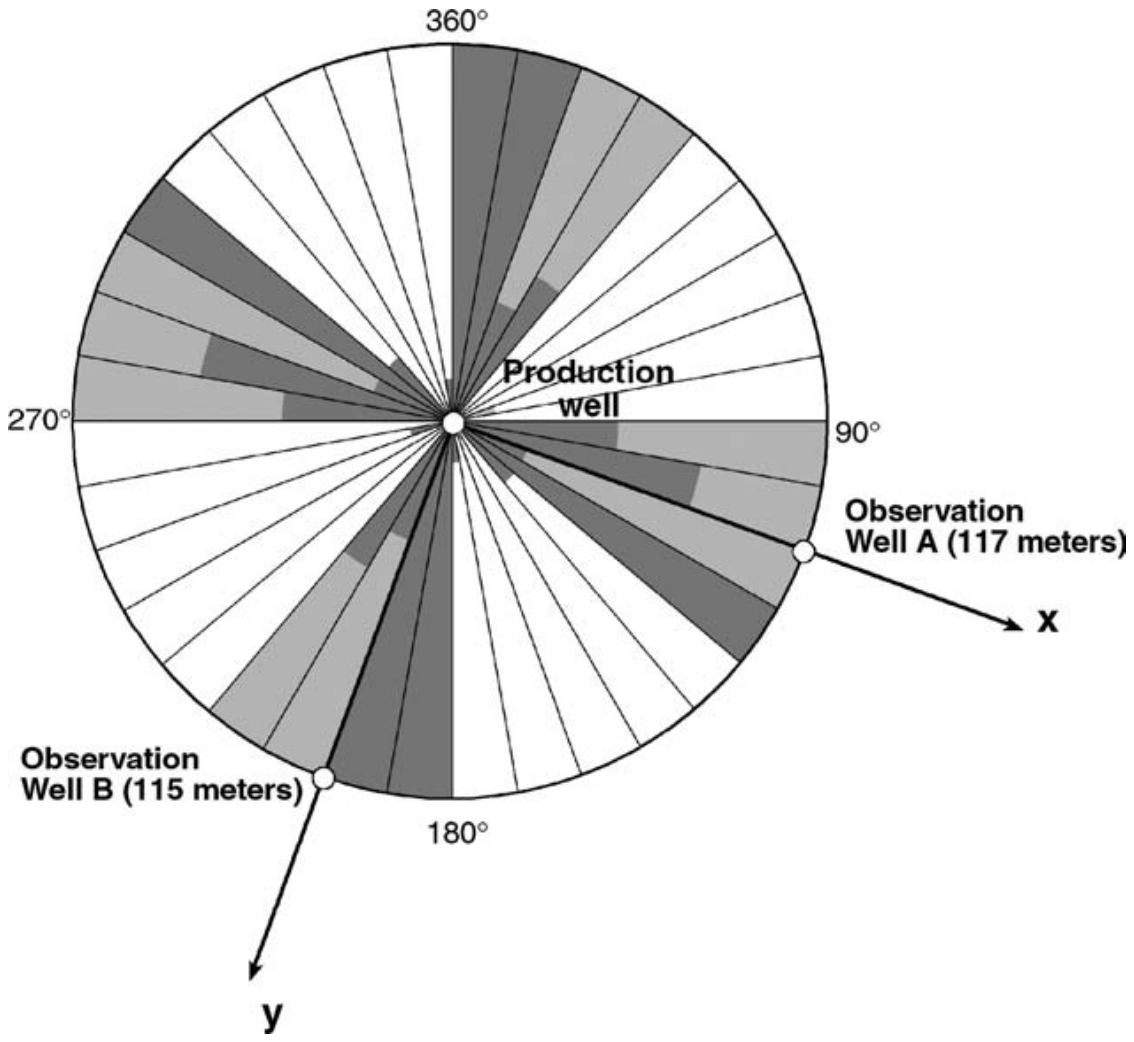

Figure 4.1: Rose diagram (circular histogram) summarising fracture orientations and locations of the observation wells at Anderson Junction. We remark on the two modes along the x and y axis. Figure reproduced from V. M. Heilweil & Hsieh (2006).

orthogonal fracture sets that allows well B to be orthogonal to well A. This observation supports the development of a random model that can represent multi-modal and/or non-orthogonal fracture sets. Finally, we note that when using InSAR to infer AHC for any prior model to be useful it should not be necessary to assume which direction is the major and minor one *a priori*. As we will show here, the proposed random model of AHC can naturally support these diverse states of uncertainty.

The fracture data discussed in the previous paragraphs represent a circular random variable. Circular random variables are increasingly used in the earth sciences to represent directional data (Adler & Thovert, 2013; Lark et al., 2014; Rad et al., 2022). Circular random variables are distributed on the unit circle, characterized by the property that the upper limit is topologically close to the lower limit. This distinctive feature necessitates specialized approaches for all aspects of statistical analysis, see e.g. Mardia & Jupp (1999); Ley & Verdebout (2017) for a full treatment. Examples of circular random variables include gene expression (Taghia et al., 2014) and wind direction data (Rad et al., 2022). Returning to structural geological data (Pollard & Fletcher, 2005), Lark et al. (2014) were the first to propose using a mixture of von Mises distributions (Pewsey & García-Portugués, 2021) within a frequentist MLE framework to capture complex multimodal directional data, and thereby extending the earlier unimodal construction of Davis (2002).

The first contribution of this paper is to develop a Bayesian model for potentially multi-modal directional structured geological data. This model will be calibrated against the fracture data acquired at the Anderson Junction site (V. M. Heilweil & Hsieh, 2006) to produce a random model of the principal direction of the AHC tensor. The proposed model consists of a collection of circular von Mises distributions with unknown means and variances that are then mixed with weights modeled using a Dirichlet distribution (Bishop, 2006, Chapter 9). In contrast to the non-probabilistic analysis of the fracture outcrop data performed in the original study of V. M. Heilweil & Hsieh (2006), our model is capable of capturing uncertainty in the principal direction and the multi-modality present in the original data. Additionally, it is able to represent fracture sets (modes) that are non-orthogonal. Aside from some structural differences that we discuss later, a distinct methodological difference between our work and Taghia et al. (2014) is that we use a Markov chain for posterior exploration, rather than VI (Blei et al., 2017b). Further,

we include an alternative approach for determining model complexity (here, the strict number of mixtures) based on LOOCV (Mao et al., 2014), rather than reversible jump MCMC (Mulder et al., 2020) or ELBO (Taghia et al., 2014).

The poroelastic model of the Anderson Junction pump test described in Salehian Ghamsari, Dam, & Hale (2025) is parameterized by the AHC tensor. For this model to be well-posed, the AHC tensor must be SPD. To convert the stochastic model of the principal direction to an SPD tensor we follow an approach for constructing random SPD second-rank tensors as proposed in (Shivanand et al., 2024). In short, the SPD AHC tensor undergoes spectral decomposition – its positive eigenvalues represent the strength of the hydraulic conductivity along the principal axis, while its orthogonal eigenvectors capture its orientation. The eigenvectors are parameterized by a (random) angle, the eigenvalues by (random) strictly positive reals, and the SPD property of the random AHC tensor is then guaranteed by a rigorous Lie group derivation. Importantly for our application, this construction allows for separate control of magnitude and direction, facilitating the representation of complex anisotropy like that induced by the directional model described in the previous paragraph.

To demonstrate the flexibility of our development, we construct two conceptual states of uncertain AHC based on data from the Anderson Junction site. In the first setting, we assume knowledge of the fracture outcrop data and the magnitude of AHC in the principal directions inferred in V. M. Heilweil & Hsieh (2006) – this allows us to only consider the fracture set mode in the direction of well A. In the second setting, we assume that we do not posses knowledge of the magnitudes of AHC, so the major direction could be in the direction of well A or well B. For the two cases, we calculate summary statistics of the InSAR LOS surface displacement to evaluate the influence of AHC uncertainty. The results indicate that the uncertainty is greatest in regions far from the pumping well and that directional uncertainty leads to potentially complex standard deviation patterns in space and time, underscoring the importance of modeling uncertain AHC on the subsidence response of an aquifer.

In summary, the main contributions of our paper are as follows:

1. We introduce a Bayesian mixture model for the rotation angle representing the complex multi-directional fracture data at Anderson Junction. This extends the

frequentist approach for fitting structural geology data originally described in Lark et al. (2014) to a Bayesian setting.

2. Leveraging the Bayesian rotation angle model we extend the Lie group construction of SPD tensors proposed in Shivanand et al. (2024) to more complex anisotropic settings, including multi-modal principal directions.

3. We show that our AHC model is sufficiently flexible to replicate two conceptual states of knowledge about the Anderson Junction site.

4. We propagate the resulting uncertainty through a poroelastic model of the pump test and show that uncertain AHC leads to a substantial impact on the model's prediction of InSAR LOS displacements.

Although our method is applied to a hydrological problem, the overall approach is relatively general and could be applied to any setting where complex uncertainty in an anisotropic second-rank tensor quantity is present.

This paper is structured as follows: Section 4.2 provides an overview of the Anderson Junction study area, focusing on the aquifer pumping test and fracturing observed in this area. In Section 4.3, we detail the methodology, including the PDE-based forward model, the parametric Bayesian model for fracture outcrop data, the construction of a model for the AHC tensor, and finally the forward uncertainty analysis through the PDE-based forward model. The implementation and results are presented in Section 4.4, before we conclude in Section 4.5.

4.2 Case study

In this section, we restate the main features of the Anderson Junction aquifer pumping test, Utah, USA, see Fig. 3.1 (Hurlow, 1998; V. M. Heilweil & Hsieh, 2006; Salehian Ghamsari, Dam, & Hale, 2025). The test used a pumping well and two observation wells, assumed to be aligned with the principal directions of AHC, to estimate the major and minor hydraulic conductivity of the confined Navajo sandstone aquifer. Groundwater extraction from the pumping well occurred over a period of four days at an average

rate of $0.07\,\mathrm{m}^3\,\mathrm{s}^{-1}$. Salehian Ghamsari, Dam, & Hale (2025) predicted that the vertical surface displacement induced by this pumping would likely be insufficient to be detected using Sentinel-1 InSAR. To address this limitation, we designed a hypothetical scenario where pumping occurred at $0.28\,\mathrm{m}^3\,\mathrm{s}^{-1}$ for 8 days – this rate is used in our numerical experiments in this paper.

Figure 4.1 summarizes the relative frequency of fracture directions (azimuths) in the Navajo Sandstone. The primary fracture cluster (x direction) is oriented towards the east at 90° to 130° and the secondary fracture cluster (y direction) at 180° to 210°. After acquiring pressure drop data at the observation wells, V. M. Heilweil & Hsieh (2006) estimated the hydraulic conductivity in the major principal direction as $k_{xx} = 1.1 \times 10^{-8} \pm 21\%\ \mathrm{m}^3\,\mathrm{s}\,\mathrm{kg}^{-1}$ and in the minor direction $k_{yy} = 4.7 \times 10^{-10} \pm 19\%\ \mathrm{m}^3\,\mathrm{s}\,\mathrm{kg}^{-1}$. Hydraulic conductivity is an intrinsic property of the aquifer, independent of pumping rate. Thus, we use these inferred conductivities in our hypothetical scenario.

4.3 Methodology

In Fig. 4.2, we outline the key elements of our proposed methodology. In this section, we discuss the mathematical aspects of the model. The calibration and application to the Anderson Junction site is left for Section 4.4.

4.3.1 The anisotropic hydraulic conductivity (AHC) tensor

The poroelastic finite element model is detailed in Chapter 2. We replace the AHC tensor k in Eq. (2.1) with $\tilde{k}$, both of which will be defined in detail below. To represent the AHC tensor $\tilde{k}$ using vector and matrix notation, we specify the three-dimensional Euclidean space with mutually orthogonal axes (x, y, z). The x-axis and y-axis are aligned with the directions x and y shown in Fig. 4.1. The z-axis points downward into the earth. Unless otherwise stated, all first- and second-ranked tensor-valued quantities in the paper are written as vectors and matrices, respectively, with respect to this Euclidean space.

We define the space of real-valued symmetric second-rank tensors (matrices) as

$$\mathrm{Sym}(d) := \{k \in \mathbb{R}^{d\times d} \mid k_{ij} = k_{ji}\}, \tag{4.1}$$

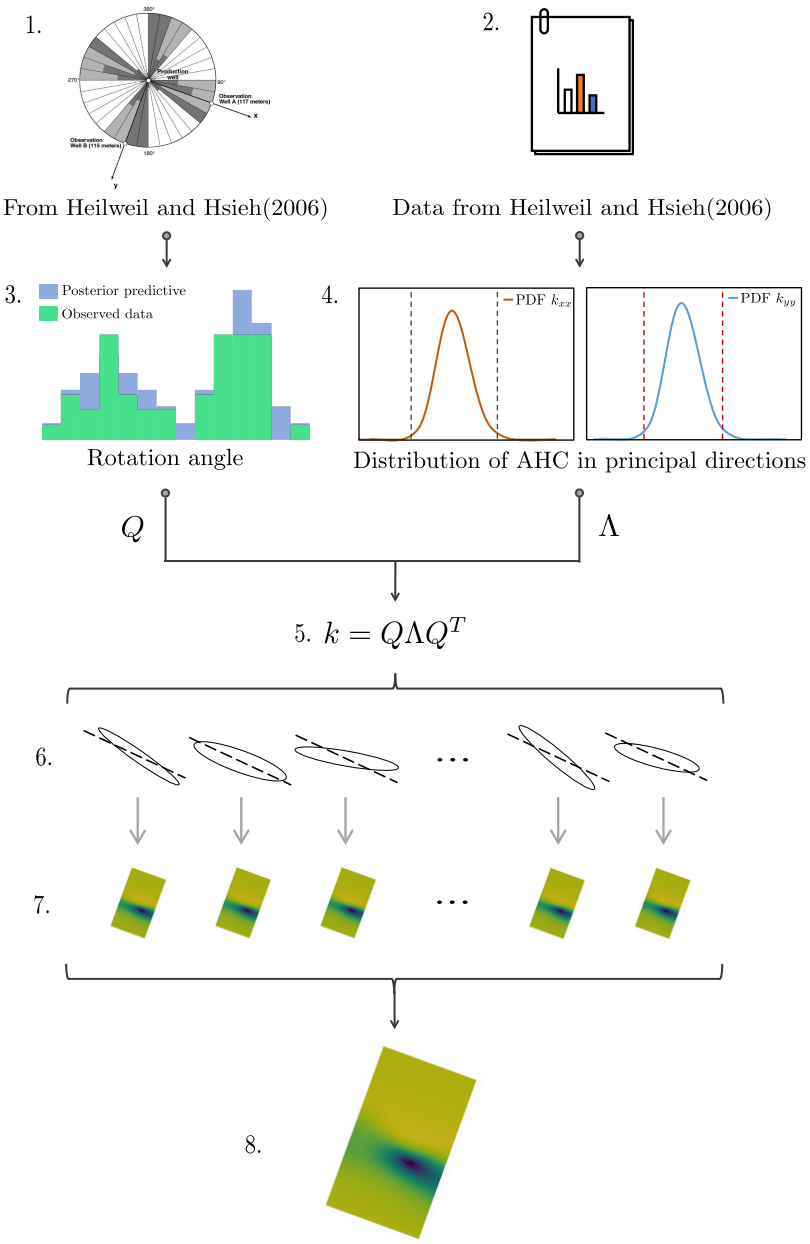

Figure 4.2: Overview of methodology. 1. Principal direction data from structural geological data; 2. Data on hydraulic conductivity in principal directions; 3. Calibration of Bayesian model for rotation angle from structural geological data; 4. Calibration of model on hydraulic conductivity in principal directions using hydraulic conductivity data; 5. and 6. Using calibrated models from 3. and 4. generate random SPD AHC tensors; 7. Propagate uncertainty induced by AHC tensor through the conceptual model of Anderson Junction aquifer system; 8. Summary statistics of the InSAR LOS displacement.

and the subset of positive definite tensors as

$$\mathrm{Sym}^+(d) := \{k \in \mathrm{Sym}(d) \mid z^T k z > 0,\ \forall z \in \mathbb{R}^d \setminus \{0\}\}. \tag{4.2}$$

To guarantee that Eq. (2.1) is well posed, the AHC tensor $\tilde{k}$ must be a member of $\mathrm{Sym}^+(3)$. We assume that one of the eigenvectors of $\tilde{k}$ is aligned with the z-axis and thus $k_{xz} = k_{yz} = 0$. In this case we have $\tilde{k}$

$$\tilde{k} = \left[\begin{array}{cc|c} k_{xx} & k_{xy} & 0 \\ k_{yx} & k_{yy} & 0 \\ \hline 0 & 0 & k_{zz} \end{array}\right], \tag{4.3}$$

where the lines in the tensor emphasize the natural block structure. The random modeling in our paper will focuses on the top left block of $\tilde{k}$, which we denote $k \in \mathrm{Sym}^+(2)$, and represents uncertainty in the AHC in the x–y plane. Alghamdi (2020) noted that InSAR displacement data provides little information for inferring k_{zz}. Therefore we treat k_{zz} as perfectly known (non-random).

The arguments presented in Shivanand et al. (2024) that lead to a natural parametrization of $k \in \mathrm{Sym}(2)$ in terms of a clockwise rotation angle ϕ in the $x - y$ plane about the z-axis and two positive eigenvalues λ_x and λ_y. We focus here on basic notions that apply in both the deterministic and random setting, and return to the specifics of the stochastic construction in Section 4.3.4. We begin by defining the space of diagonal tensors as

$$\mathrm{Diag}^+(d) := \left\{\Lambda \in \mathbb{R}^{d\times d} \mid \Lambda = \mathrm{diag}(\lambda_1, \lambda_2, \ldots, \lambda_d),\ \lambda_i \in \mathbb{R}^+_*\right\}, \tag{4.4}$$

where $\mathbb{R}^+_*$ is the space of strictly positive real numbers. The space of orthogonal tensors

$$\mathrm{O}(d) := \left\{Q \in \mathbb{R}^{d\times d} \mid Q^T Q = I\right\}, \tag{4.5}$$

the subset of special orthogonal tensors

$$\mathrm{SO}(d) := \{R \in \mathrm{O}(d) \mid \det(R) = 1\}, \tag{4.6}$$

and its Lie algebra of skew-symmetric tensors

$$\mathfrak{so}(d) := \left\{ W \in \mathbb{R}^{d \times d} \mid W^T = -W \right\}. \tag{4.7}$$

We also define the unit circle

$$\mathbb{S}^1 = \left\{ (\cos(\phi), \sin(\phi)) \mid \phi \in [0, 2\pi) \right\}. \tag{4.8}$$

Any $k \in \mathrm{Sym}^+(2)$ can be decomposed into a tensor $\Lambda := \mathrm{diag}(\lambda_x, \lambda_y) \in \mathrm{Diag}^+(2)$ of eigenvalues and an tensor of eigenvectors $Q \in \mathrm{O}(2)$

$$k = Q \Lambda Q^T. \tag{4.9}$$

We can further rotate the eigenvectors Q by applying a rotation tensor $R \in \mathrm{SO}(2)$

$$k = (RQ) \Lambda (RQ)^T, \tag{4.10}$$

It is this decomposition that forms the basis of the stochastic construction in Shivanand et al. (2024). Using the rotation angle ϕ about the z-axis we construct an infinitesimal rotation tensor $W \in \mathfrak{so}(2)$ as

$$W = \phi \begin{bmatrix} 0 & -1 \\ 1 & 0 \end{bmatrix}. \tag{4.11}$$

Following Hall (2015), it is possible to connect the space $\mathrm{SO}(d)$ with its Lie algebra $\mathfrak{so}(d)$ through the map $\exp : \mathfrak{so}(d) \to \mathrm{SO}(d)$, leading to

$$R = \exp(W). \tag{4.12}$$

As a consequence of the Cayley-Hamilton theorem (Axler, 2024), the Euler-Rodrigues formula gives

$$R = \exp(W) = I + \frac{\sin \phi}{\phi} W + \frac{1 - \cos \phi}{\phi^2} W^2, \tag{4.13}$$

which reduces to the standard result linking a rotation angle with a rotation matrix

$$R = \begin{bmatrix} \cos\phi & -\sin\phi \\ \sin\phi & \cos\phi \end{bmatrix}. \tag{4.14}$$

This construction can be extended to the more general three-dimensional case without the block structure in Eq. (4.3). By parametrizing R using two angles ϕ and η, the latter representing a tilt around the y-axis, we can incorporate uncertainty about an additional preferential direction, for example, in a bedding plane dip angle.

4.3.2 Rotation angle model

In this subsection we develop a hierarchical Bayesian model for the rotation angle ϕ used in Eqs. (4.10) to (4.12). Throughout the rest of the paper we use a hat $\hat{\cdot}$ to emphasize that a quantity is non-stochastic, i.e. is perfectly known.

To model potentially multi-modal directional data, a mixture of circular von Mises distributions is a suitable choice (Ley & Verdebout, 2017; Taghia et al., 2014). We write the joint random model for $n \geq 1$ mixtures on the latent parameters $\theta^n = (\mu_1, \kappa_1, c_1, w_1, m_1 \ldots, \mu_n, \kappa_n, c_n, w_n, m_n)$ and p independent and identically distributed (i. i. d.) rotation angles $\phi_1, \phi_2, \ldots, \phi_p$

$$\mu_1, \ldots, \mu_n \overset{\text{iid}}{\sim} \text{VonMises}(\hat{\mu}, \hat{\kappa}), \tag{4.15a}$$

$$\kappa_1, \ldots, \kappa_n \overset{\text{iid}}{\sim} \text{Gamma}(\hat{\alpha}, \hat{\beta}), \tag{4.15b}$$

$$c_1, \ldots, c_n \overset{\text{iid}}{\sim} \text{VonMises}(\mu_i, \kappa_i), \tag{4.15c}$$

$$w_1, \ldots, w_n \sim \text{Dirichlet}(\hat{a}_1, \ldots, \hat{a}_n), \quad n \geq 2, \tag{4.15d}$$

$$w_1 = 1, \quad n = 1, \tag{4.15e}$$

$$m_1, \ldots, m_n \sim \text{Categorical}(w_1, \ldots, w_n), \tag{4.15f}$$

$$\phi_1, \phi_2, ..., \phi_p \overset{\text{iid}}{\sim} \text{Mixture}((m_1, \ldots, m_n), (c_1, \ldots, c_n)), \tag{4.15g}$$

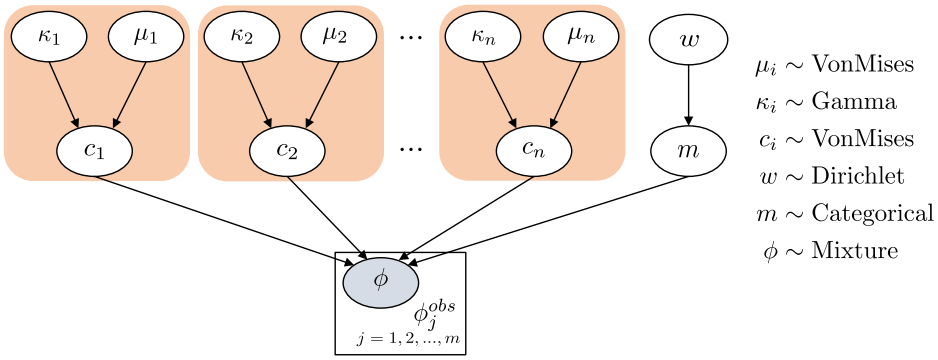

Figure 4.3: DAG of the mixture of von Mises model for $n \geq 2$ mixtures. The square boxes denote fixed or observed quantities, and the circles denote unknowns.

which in the case of $n = 1$ (i.e., no mixtures) reduces to

$$\begin{aligned} \mu_1 &\sim \text{VonMises}(\hat{\mu}, \hat{\kappa}), \\ \kappa_1 &\sim \text{Gamma}(\hat{\alpha}, \hat{\beta}), \\ \phi_1, \phi_2, ..., \phi_p &\overset{\text{iid}}{\sim} \text{VonMises}(\mu_1, \kappa_1). \end{aligned}$$

The hierarchical model for the $n \geq 2$ case is visualized as a directed acyclic graph (DAG) in Fig. 4.3. Here, we summarize the components, parameterization and structure of the model. We do not show explicit expressions for the probability density function (PDF) associated with each component, as these are relatively standard, and instead refer the reader to e.g. Mardia & Jupp (1999); Taghia et al. (2014). The VonMises distribution, parameterized by a mean μ and concentration κ is the natural extension of the normal distribution to the circle. For each von Mises component c_i in the mixture, we place a VonMises hyperprior on each μ_i, and a Gamma hyperprior on each κ_i, parameterized by shape $\hat{\alpha}$ and rate $\hat{\beta}$ parameters. The mixture weights w are selected from a Dirichlet prior with concentration parameters $\hat{a}_1, \ldots, \hat{a}_n$, fed into a Categorical prior to produce the latent component probabilities $m_1, \ldots, m_n$. Finally, the rotation angles are assumed i. i. d. from a Mixture of $c_1, \ldots, c_n$ weighted with $m_1, \ldots, m_n$.

Our model construction roughly follows that of Taghia et al. (2014) except that those authors choose to set the hyperprior μ_i concentration parameter as $\hat{\beta}\kappa_i$ with $\hat{\beta}$ a positive constant. We have experimented with both versions of the model and did not find any

issues with identifiability using our construction on the examples we present later.

After observing p iid samples of the rotation angle $\phi_1^{\text{obs}}, \ldots, \phi_p^{\text{obs}}$, we condition the joint model for a specific number of mixtures n in Eq. (4.15) on data to form the Bayesian posterior $\theta^n \mid \phi_1^{\text{obs}}, \phi_2^{\text{obs}}, \ldots \phi_p^{\text{obs}}$. We generate samples from the posterior using the No-U-Turn Sampler (NUTS) (Hoffman & Gelman, 2014), a gradient-based Hamiltonian Monte Carlo (HMC) method (Duane et al., 1987; Neal, 1996). In our numerical computations we use the parameterizations as defined in the probabilistic programming language NumPyro (Phan et al., 2019; Rønning et al., 2021).

Later, we will calibrate models with varying number of mixtures n to the observed rotation angle data. Consequently it will be necessary to select the number of mixtures that best represents the underlying data, while remaining conservative. This model selection problem can be tackled via a number of approaches, e.g. information theoretic approaches (Akaike, 1998; Spiegelhalter et al., 2002; van der Linde, 2005; Watanabe & Opper, 2010), Bayes factors (Friel & Pettitt, 2008) and cross-validation (CV) (Vehtari et al., 2017). Please see Gelman et al. (2014); Watanabe (2021); Zhang et al. (2023) for the relative merits of these different approaches.

In this study we use a CV approach, specifically Leave-one-out cross-validation (LOOCV) as described in (Vehtari et al., 2017) via the implementation in ArviZ (Kumar et al., 2019), a Python package for exploratory data analysis. LOOCV is widely used to obtain a reliable test for model performance estimation and less commonly used as a model selection criterion. Although LOOCV is significantly more computationally expensive than information theoretic approaches such as Akaike information criterion (AIC) (Akaike, 1998) and deviance information criteria (DIC) (Spiegelhalter et al., 2002; van der Linde, 2005), LOOCV offers greater flexibility and applicability to complex models like the mixture model we consider here (Vehtari et al., 2015, 2017).

4.3.3 Eigenvalue model

We model the eigenvalues as log-normal random variables

$$\lambda_x \sim \text{Lognorm}(\hat{\mu}_x, \hat{\sigma}_x^2), \tag{4.16a}$$

$$\lambda_y \sim \text{Lognorm}(\hat{\mu}_y, \hat{\sigma}_y^2). \tag{4.16b}$$

This representation ensures positivity thus guaranteeing $\Lambda \in \text{Diag}^+(2)$. [2]

The simplicity of the model and the available data allow us to calibrate our model with V. M. Heilweil & Hsieh (2006) by calibrating the four parameters $(\hat{\mu}_x, \hat{\sigma}_x^2, \hat{\mu}_y, \hat{\sigma}_y^2)$ manually. In the presence of richer data more complex models could be developed and formally calibrated using e.g. MLE or Bayesian approaches.

4.3.4 Anisotropic hydraulic conductivity model

Following the arguments in Shivanand et al. (2024), we extend the construction of k in Eqs. (4.10) and (4.14) to the stochastic setting. We treat k as a function of the random variable $\omega := (\phi, \lambda_x, \lambda_y)$ composed of the rotation angle and eigenvalues, i.e.

$$k(\omega) : [0, 2\pi) \times \mathbb{R}_*^+ \times \mathbb{R}_*^+ \to \text{Sym}^+(2), \tag{4.17}$$

on a probability space (triple) defined in the standard way, see e.g. Klenke (2020).

We now discuss the full stochastic extension of Eq. (4.10) and two special cases (Shivanand et al., 2024). In the full model, we will generate AHC tensors with randomness in both scaling and rotation

$$k(\omega) = R(\phi)\widehat{Q}\Lambda(\lambda_x, \lambda_y)\widehat{Q}^T R(\phi)^T. \tag{4.18}$$

In the first simplified model k_s we assume that ϕ is known perfectly and there is no rotation, i.e. $\hat{\phi} = 0$ and $R = I$. This means that the scaling is the only parameter that

[2] In Shivanand et al. (2024) precisely the same construction is derived via $\text{Diag}^+(2)$ having Lie algebra $\mathfrak{Diag}(2)$ and modeling $\log(\Lambda) \in \mathfrak{Diag}(2)$ with the two diagonal entries modeled as two normal random variables.

is varied, leading to

$$k_s(\omega) = \widehat{Q}\Lambda(\lambda_x, \lambda_y)\widehat{Q}^T. \tag{4.19}$$

In the second simplified model k_r we assume that both $\lambda_x = \hat{\lambda}_x$ and $\lambda_y = \hat{\lambda}_y$ are perfectly known, leading to randomness only in the rotations

$$k_r(\omega) = R(\phi)\widehat{Q}\widehat{\Lambda}(\hat{\lambda}_x, \hat{\lambda}_y)\widehat{Q}^T R(\phi)^T. \tag{4.20}$$

To produce samples $\{k(\omega_i)\}_{i=1}^N$ distributed according to k in Eqs. (4.17) and (4.18), we first generate rotation angle samples assumed i. i. d. $\{\phi_i\}_{i=1}^N$ according to the posterior predictive distribution $\phi \mid \phi_1^{\text{obs}}, \ldots, \phi_p^{\text{obs}}$ (Gelman et al., 2020, Section 6.1) induced by the model Eq. (4.15) at fixed n. We then generate eigenvalue samples $\{\lambda_x\}_{i=1}^N$ and $\{\lambda_y\}_{i=1}^N$ using a standard generator for the log-normal distribution, before finally passing each $\omega_i = (\phi_i, \lambda_{xi}, \lambda_{yi})$ through equation Eq. (4.18). The process for generating samples from the models with fixed parameters Eqs. (4.19) and (4.20) will be described in the following section.

4.3.5 Forward uncertainty propagation

To study how uncertainty in the AHC tensor induces uncertainty in the LOS surface displacement we calculate summary statistics of the LOS surface displacement using the Monte Carlo technique. Given N assumed i. i. d. samples $\{k_i\}_{i=1}^N$ we can calculate N solutions of $\{u_{\text{LOS}}(x, t, k_i)\}_{i=1}^N$ by solving the PDE system Eq. (2.1) and calculating the LOS displacement Eq. (3.1). The mean of the LOS displacement is then computed as

$$\mu(u_{\text{LOS}}(x,t)) := \frac{1}{N}\sum_{i=1}^{N} u_{\text{LOS}}(x, t, k_i), \tag{4.21}$$

and the unbiased estimation of standard deviation is calculated as

$$\text{Std}(u_{\text{LOS}}(x,t)) := \left[\frac{1}{N-1}\sum_{i=1}^{N}\left[u_{\text{LOS}}(x,t,k_i) - \mu(u_{\text{LOS}}(x,t))\right]^2\right]^{1/2}. \tag{4.22}$$

4.4 Results

We apply the methodology described in Section 4.3 to develop two models reflecting different states of subjective Bayesian belief (Jaynes, 2003) about the Anderson Junction site. The specification of the poroelastic finite element model can be found in Chapter 3 and Salehian Ghamsari, Dam, & Hale (2025).

In the first scenario, detailed in Sections 4.4.1 to 4.4.4 we use the fracture data Fig. 4.1 and the major and minor hydraulic conductivity estimates from the pump test in V. M. Heilweil & Hsieh (2006). Since the pump test determined the major principal direction of AHC using Papadopulus method, the rotation angle ϕ cannot lie along the fracture mode coinciding with well B. Consequently, we construct a model that captures the complexity in the rotation angle data only in the direction of well A.

In the second scenario, described briefly in Section 4.4.5, we assume no knowledge of the outcome of the pump test. Instead, we rely solely on the fracture data and the general understanding that the hydraulic conductivity may be anisotropic – this is the same state of knowledge as in V. M. Heilweil & Hsieh (2006) *prior* to the pump test. Without the pump test data, the major principal direction remains uncertain and could be aligned with either of the primary fracture directions in Fig. 4.1.

4.4.1 Calibrating the rotation angle model

Following the developments in Section 4.3.2 we calibrate the rotation angle model Eq. (4.15) for $n = 1, 2, 3$ mixtures against the fracture direction isolated around the direction of well A in Fig. 4.1. This leads to three calibrated models denoted VM1, VM2 and VM3.

Because fracture orientation data at the Anderson junction site is only available in summarized form Fig. 4.1, rather than raw rotation angle data $\left\{\phi_i^{\text{obs}}\right\}_{i=1}^{M}$, we generate $M = 1000$ synthetic rotation angle observations for use in the calibration. Our methodology is not limited to this setting and works well with raw rotation angle data.

The models Eq. (4.15) are implemented in NumPyro (Phan et al., 2019; Rønning et al., 2021). Samples are simulated from each posterior using the built-in implementation of NUTS. Standard MCMC chain convergence diagnosis is performed and pass (results not shown). Further exploratory analysis including the model selection via LOOCV–

Symbol	Description	Unit	Value
$\hat{\mu}$	measure of location	rad	0.0
$\hat{\kappa}$	measure of concentration	rad^{-2}	π
$\hat{\alpha}$	shape parameter	-	20.0
$\hat{\beta}$	rate parameter	rad^2	0.1
$\hat{a}_1, \ldots, \hat{a}_n$	concentration parameters	-	$1, 1, ..., 1.$

Table 4.1: Non-informative prior parameters for the rotation angle model.

Model	rank	`elpd_loo`	`p_loo`	`elpd_diff`	`SE`
3VM	1	276.80	23.41	0.00	20.63
2VM	2	260.81	4.95	15.99	21.52
1VM	3	44.48	1.41	232.32	13.98

Table 4.2: Model selection results. `rank`: The rank-order of the models based on `elpd_loo`. `elpd_loo`: Expected log pointwise predictive density. `p_loo`: Estimated effective number of parameters. `elpd_diff`: The difference in ELPD between models, computed relative to the top-ranked model, which always has an `elpd_diff` of 0. SE: Standard error of the ELPD estimate. 2VM is the preferred model; interpretation of the results is given in the text.

expected log pointwise predictive density (ELPD) is performed using ArviZ (Kumar et al., 2019).

The posterior predictive distributions of the three calibrated models are shown in Fig. 4.4. The blue histogram summarizes the posterior predictive rotation angle data, and the green histogram summarizes the rotation angle data used for calibration. 2VM and 3VM show a reasonable fit to the original data, while 1VM is, as expected, inadequate.

In Table 4.2 we show the results of the model selection. The models are ranked from best to worst based on the `elpd_loo` – a higher `elpd_loo` indicates a better out-of-sample predictive fit. The estimated effective number of parameters `p_loo` reflects the complexity of the model – a higher value indicating greater complexity. Following the guidelines in Vehtari et al. (2017), a model can be considered better than another only if the `elpd_diff` significantly exceeds the standard error `SE` of the ELPD estimate. The `elpd_diff` between 2VM and 3VM is 15.99, which is less than the standard error of 21.52, so we cannot conclude that 3VM is superior to 2VM. We then compare the complexity using `p_loo` and determine that 2VM is less complex than 3VM - consequently we choose 2VM and continue with 2VM through the following sections.

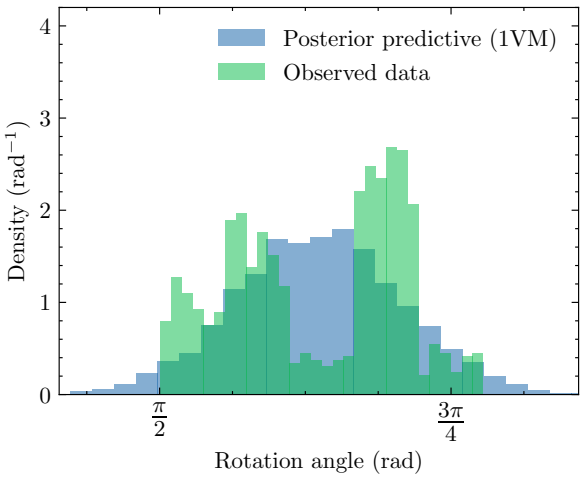

(a) Posterior predictive distribution of 1VM.

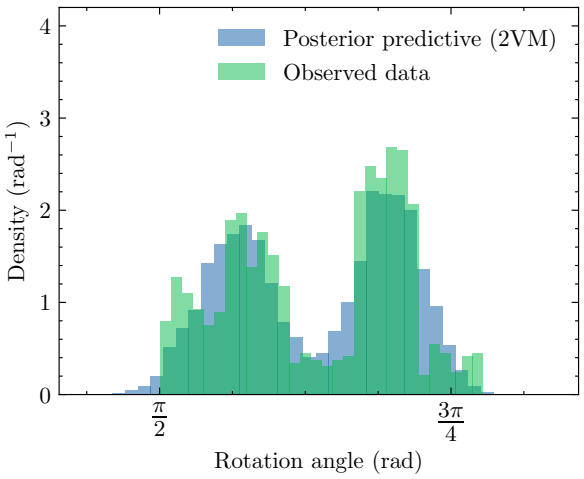

(b) Posterior predictive distribution of 2VM.

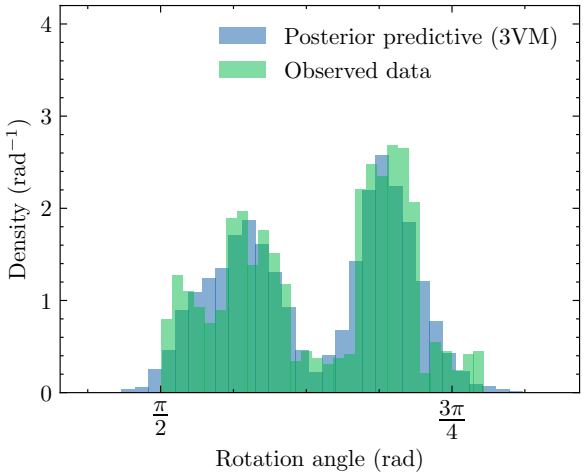

(c) Posterior predictive distribution of mixture of 3VM.

Figure 4.4: Posterior predictive checks: posterior predictive (green) and original training data (blue).

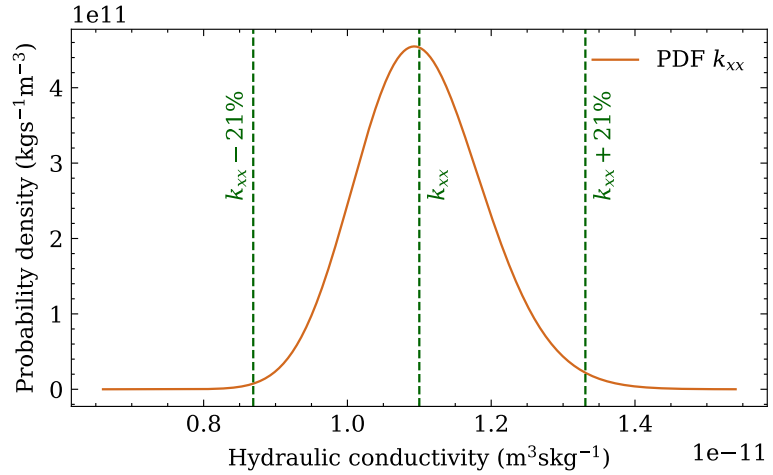

(a) Distribution of AHC magnitude in major axis.

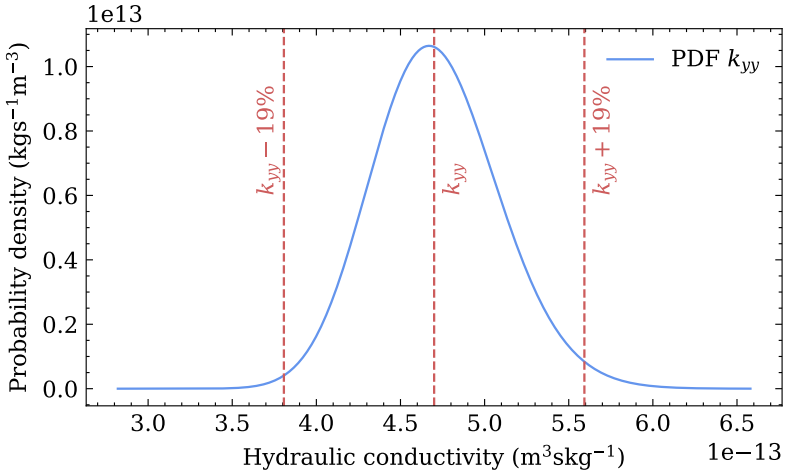

(b) Distribution of AHC magnitude in minor axis.

Figure 4.5: Probability density functions of the two eigenvalues.

4.4.2 Calibrating the eigenvalue model

We calibrate the four parameters $(\hat{\mu}_x, \hat{\mu}_y, \hat{\sigma}_x^2, \hat{\sigma}_y^2)$ of the stochastic model of the eigenvalues Eq. (4.16). As data we use the inferred values of the AHC $k_{xx} \pm 21\%$ and $k_{yy} \pm 19\%$ reported in V. M. Heilweil & Hsieh (2006) which corresponds to an anisotropy ratio of approximately 24 to 1. The values of k_{xx} and k_{yy} are provided in Table 3.2. In the original study no precise meaning is attached to the quoted $\pm$ statistic, so we choose to interpret this to mean that approximately 98 % of the probability mass of the Lognorm should lie between the $\pm$ limits. We set $\hat{\mu}_x = k_{xx}$, $\hat{\mu}_y = k_{yy}$ and iteratively adjust the variance. We find that $\hat{\sigma}_x^2 = \hat{\sigma}_y^2 = 0.0064$ approximately satisfies the 98 % condition. The PDF with these parameters are shown in Fig. 4.5.

4.4.3 Generation of AHC tensors

Using the calibrated models in Sections 4.4.1 and 4.4.2 we generate stochastic AHC tensors via Eqs. (4.18) to (4.20). Figure 4.6 provides a visualization of the random samples of the three different AHC models. The elliptical shape of the AHC tensor illustrates both the direction and magnitude of AHC along the principal directions. The direction of the ellipses indicates the principal major and minor directions of hydraulic conductivity, while the radii represent the magnitude of hydraulic conductivity in those principal directions.

4.4.4 Forward uncertainty analysis

Eqs. (4.18) to (4.20) we generate $N = 8000$ samples of the AHC tensor and propagate this uncertainty through the PDE model of the Anderson Junction. The evaluation of the model for each sample takes around 10 min on 32 MPI processes on a single node of the aion cluster at the University of Luxembourg (Varrette et al., 2022). The evaluations are parallelized and are distributed across 32 nodes of the high-performance computing (HPC), with 4 simultaneous evaluations per node. For each evaluation line-of-sight displacement u_{LOS} on the top surface Γ_t is written out to disk (around 35 MB) in the ADIOS2 format using adios4dolfinx (Dokken, 2024). The data is read back in on a single HPC job with 8 MPI processes to compute summary statistics Eqs. (4.21) and (4.22).

As a baseline for comparison in Fig. 4.7, we show the deterministic Anderson Junction hypothetical intermediate pumping scenario with rate $4 \times P_r$ after 8 d duration from (Salehian Ghamsari, Dam, & Hale, 2025). We remind the reader the effect of the LOS perspective in the outputs, which 'shifts' the observed displacement towards the east-south of the pumping well, assuming the satellite is positioned to the west-north of the aquifer.

The mean and standard deviation of the random scaling and rotation LOS displacement are shown in Fig. 4.8. When comparing the mean in Fig. 4.8a with Fig. 4.7, there is a more diffuse displacement response particularly in the west-north area. The standard deviation (Fig. 4.8b) in the west-north area supports this.

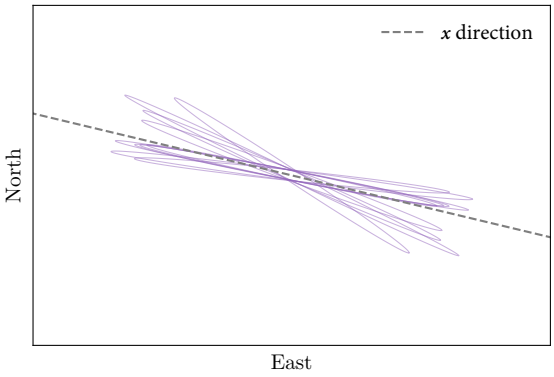

(a) Samples from scaling and rotation model Eq. (4.18).

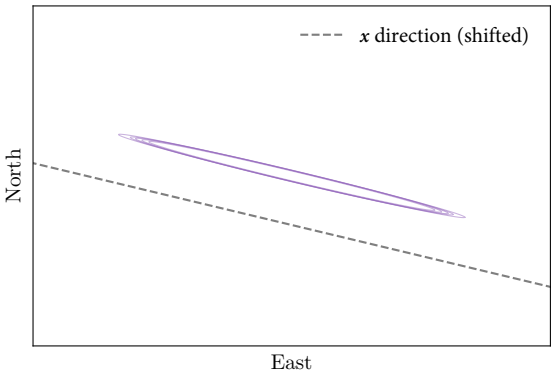

(b) Samples from scaling model Eq. (4.19). Line in x direction is shifted by a constant translation for easier visualization.

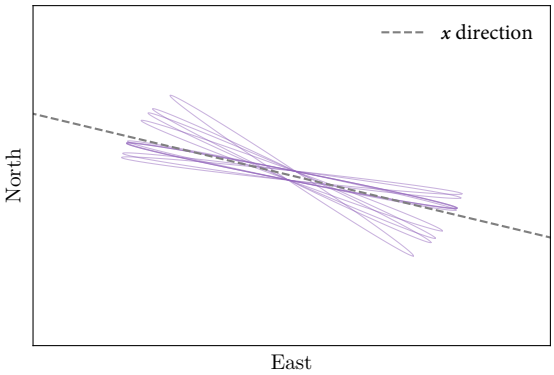

(c) Samples from rotation model Eq. (4.20).

Figure 4.6: Visualization of random samples from three models for stochastic AHC. Each random sample is plotted as an ellipse with the direction of the ellipse representing the principal directions and the radii representing the magnitude of the hydraulic conductivity in the principal directions.

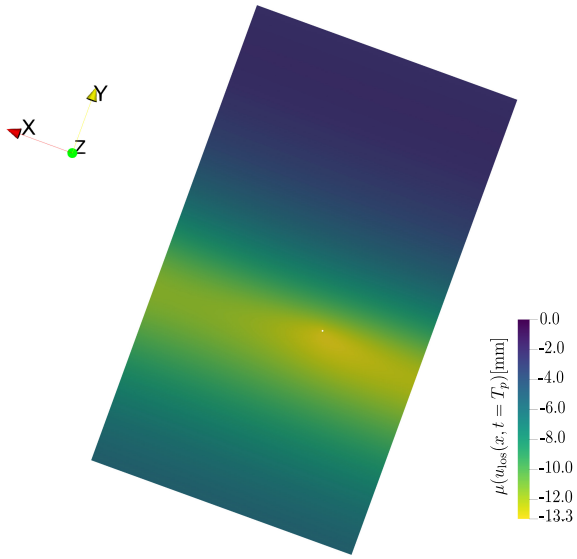

Figure 4.7: Simulated LOS surface displacement at the end of pumping for an hypothetical intermediate pumping with $4 \times P_r$ and 8 d duration. Used under CC BY 4.0 license from Salehian Ghamsari, Dam, & Hale (2025).

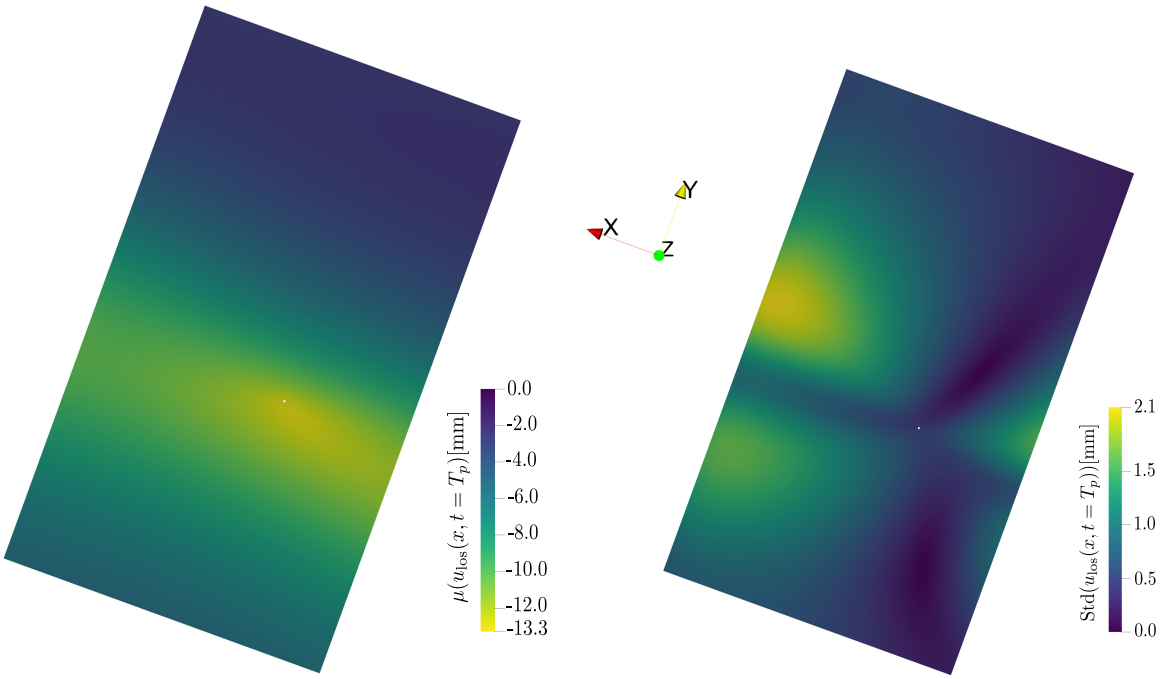

(a) Mean of LOS displacement (random scaling and rotation AHC).

(b) Standard deviation of LOS displacement (random scaling and rotation AHC).

Figure 4.8: Mean and standard deviation of the LOS displacement outputs from executing the poroelastic model using AHC with randomness in both scaling and rotation. T_p is the time when the pumping finished after 8 d of pumping. The mean values are truncated at zero from above.

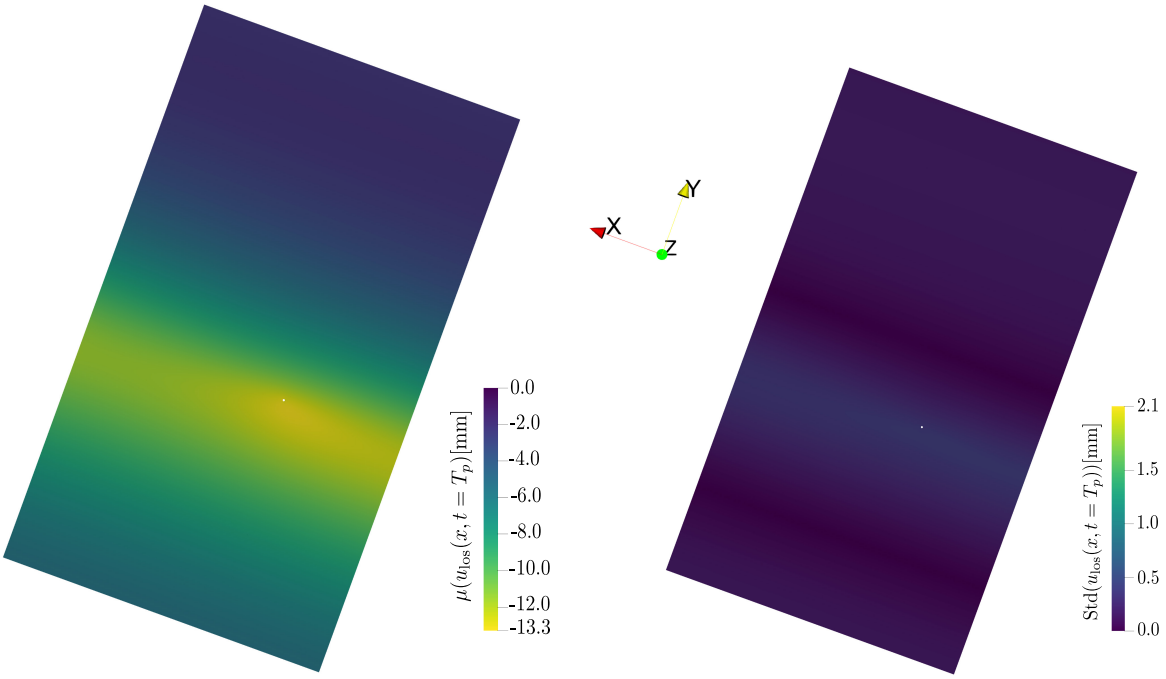

(a) Mean of LOS displacement (random scaling AHC).

(b) Standard deviation of LOS displacement (random scaling AHC).

Figure 4.9: Mean and standard deviation of the LOS displacement outputs from executing the poroelastic model using AHC with randomness in scaling. The mean values are truncated at zero from above.

In Fig. 4.9, we present the mean and standard deviation of LOS displacement calculated using AHC with random scaling alone. The mean Fig. 4.9a closely resembles the LOS displacement predicted at Anderson Junction using the hypothetical intermediate pumping test scenario (Fig. 4.7). The standard deviation indicates a very slight variation along a band aligned with the major principal direction.

Figure 4.10 shows the mean and standard deviation of the LOS displacement with random rotation applied. The results are similar to those observed in the random scaling and rotation scenario, implying that the randomness in rotation, induced by the structural geological data, has the dominant effect on the line-of-sight displacement here.

4.4.5 Second scenario

In this second modeling scenario, we assume that the AHC (from V. M. Heilweil & Hsieh (2006)) is unknown. Consequently the major principal direction could be coincident with

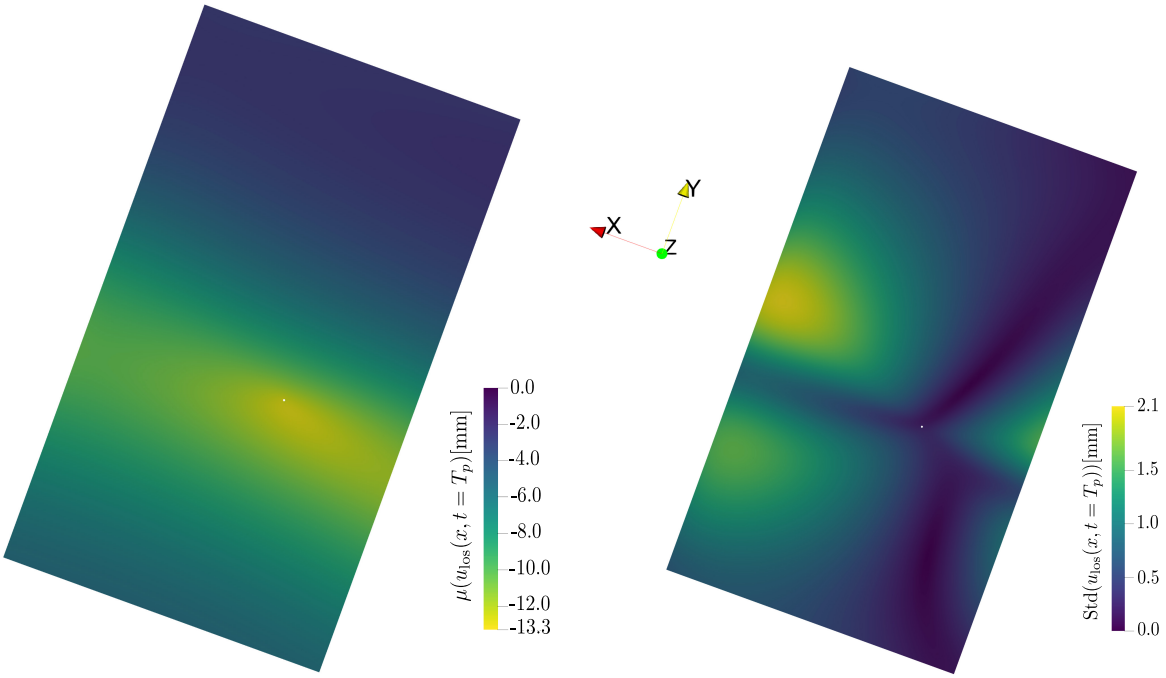

(a) Mean of LOS displacement (random rotation AHC).

(b) Standard deviation of LOS displacement (random rotation AHC).

Figure 4.10: Mean and standard deviation of the LOS displacement outputs from executing the poroelastic model using AHC with randomness in rotation. The very small mean values are truncated at zero from above.

either of the fracture modes Fig. 4.1. The lack of knowledge of the pump test also means that we need to express a greater degree of uncertainty about the anisotropy ratio between the principle directions.

Because of the additional mode to account for in the fracture data, we choose to calibrate 3VM and a new richer 4VM model for the rotation angle - the model selection process (full results not shown) selects 4VM. The posterior predictive distribution of this mixture model is shown in Fig. 4.11a.

Using Eq. (4.16), we generate eigenvalues applying a higher standard deviation, which leads to a anisotropy ratio from around 1:9 to 1:1. We then generate random AHC tensors with random scaling and rotation using Eq. (4.18). The elliptical shape of these random AHC tensors is shown in Fig. 4.11b. We can see that our parameterization using the angle and two eigenvectors supports the hypothesis that the major principal direction could lie along the direction of either well A or B.

Finally, we quantify AHC uncertainty in the LOS displacement outputs by solving our poroelastic finite element model for the generated random AHC tensors. A few sample LOS displacement outputs are presented in Fig. 4.11c, illustrating the variability in responses due to different AHC orientations and magnitudes. We remark how the mean shown in Fig. 4.11d exhibits an almost circular shape due to the AHC tensors having major direction approximately oriented along the direction of either well A or B.

4.5 Conclusions

In this study we presented a novel random model of AHC that can incorporate uncertain structural data. The model consists of three components; a Bayesian rotation angle model built from a mixture of circular von Mises distributions that encodes the principal direction of AHC, a model for positive eigenvalues that controls the magnitude of the AHC in the principal directions, both feeding into a Lie group construction for the AHC tensor. Our goal has been to design a model that could serve as a prior in a Bayesian inference setting where InSAR-derived line-of-sight data contain information about AHC. By calibrating the model against observed fracture orientations and pump test data from Anderson Junction, we were able to define two conceptual states of belief about the site.

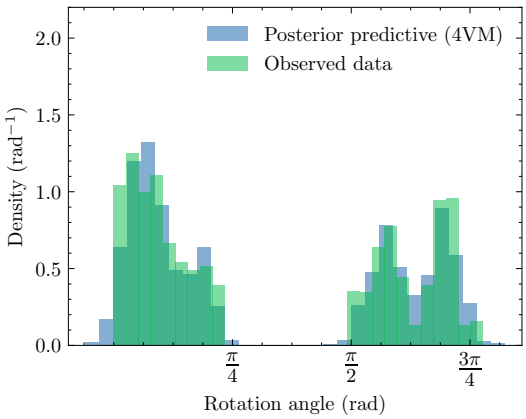

(a) Posterior predictive distribution of mixture of four von Mises model.

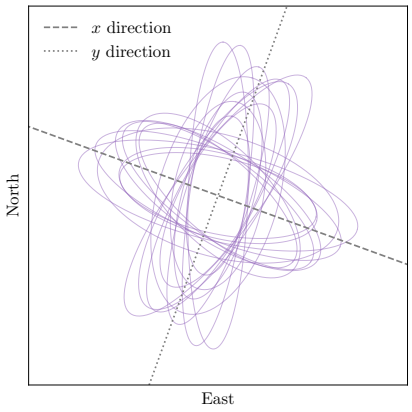

(b) AHC tensor with randomness in scaling and rotation.

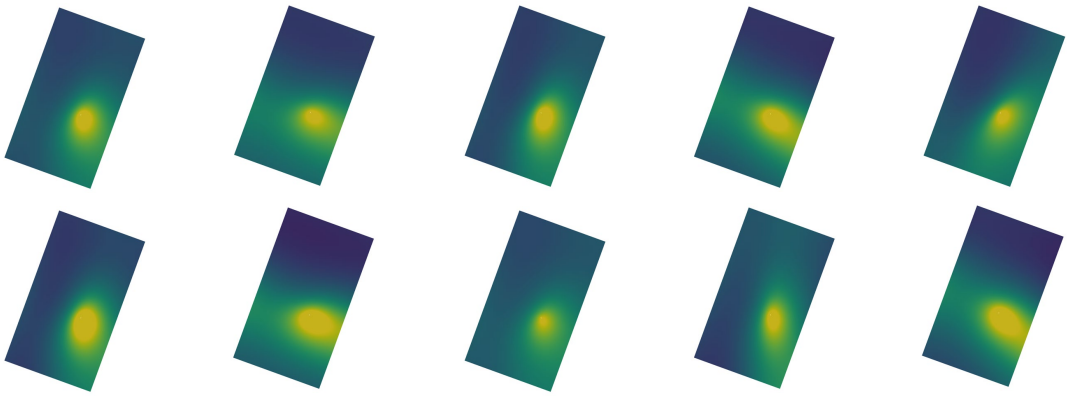

(c) Samples of LOS displacement.

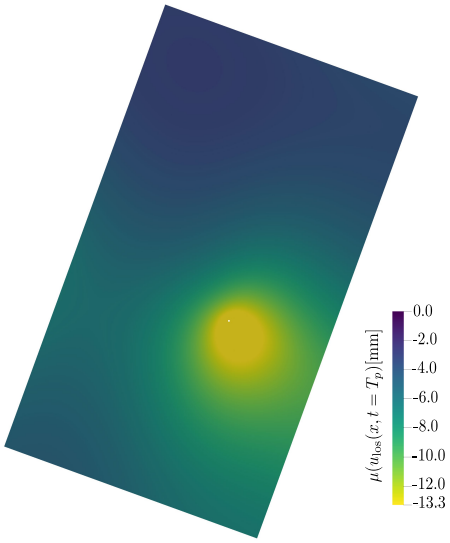

(d) Mean of LOS displacement.

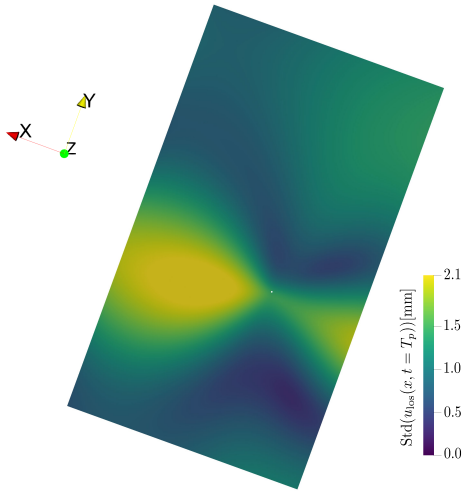

(e) Standard deviation of LOS displacement.

Figure 4.11: Results of second scenario. The scale and unit for samples Fig. 4.11c is the same as the mean Fig. 4.11d.

Our results show that the methodology provides a flexible tool for modeling uncertainty and that uncertainty in the AHC orientation has a larger impact on the LOS InSAR displacement predictions than the magnitudes of the principal directions.

In the future, we plan to explore the Bayesian calibration of the full model against real and synthetic InSAR data in order to explore parameter identifiability. The computational burden of the PDE solver presents some technological challenges. In particular, to minimize the number of model evaluations needed to create a Markov chain on the posterior we need to use a gradient-based sampling algorithm, e.g. NUTS, which requires the derivative of the log-posterior with respect to the model parameters. This can be calculated efficiently via the adjoint (back-propagation) technique. However, our full model is constructed from a complex mixture of NumPyro (probabilistic) and DOLFINx (PDE) components and although we can derive the adjoint model of each part individually and automatically using NumPyro/JAX (Phan et al., 2019; Bradbury et al., 2018) and pyadjoint (Mitusch et al., 2019), we are not currently able to write a NumPyro model containing a DOLFINx PDE solve and then derive the corresponding adjoint model. Some recent work (Bouziani & Ham, 2023) show coupling of PDE and machine-learning model graphs for gradient calculation, and we anticipate that this technique could be adapted to our model.

Supplementary material

The supplementary material (Salehian Ghamsari & Hale, 2024) includes input data, full code and further mathematical details of the finite element model.

Acknowledgments

We would like to thank Guendalina Palmirotta and Damian Mingo Ndiwago for their valuable comments on circular statistics and model selection, respectively.

The experiments presented in this paper were carried out using the HPC facilities of the University of Luxembourg (Varrette et al., 2022).

Funding

This work was funded in whole, or in part, by the Luxembourg National Research Fund (FNR), grant reference PRIDE/17/12252781. For the purposes of open access, and in fulfilment of the obligations arising from the grant agreement, the authors have applied a Creative Commons Attribution 4.0 International (CC BY 4.0) license to any Author Accepted Manuscript version arising from this submission.

Chapter 5

Automatic differentiation of models involving machine learning and PDE components

5.1 Introduction

In this chapter I will describe some ongoing work towards solving an inverse problem involving the models shown in the previous two chapters.

To specify an inverse problem where the AHC parameter will be estimated from observations of the aquifer system, there are two main approaches: deterministic inverse problems that ignore the uncertainty in the parameter and provide a point estimate, and probabilistic Bayesian inverse problems that account for uncertainty through construction and exploration of the full posterior distribution, that is, the probability of the parameters given the data.

Whether solving a deterministic optimization problem or sampling from the posterior, a critical component required for a tractable computation is the derivative of a functional of the model output with respect to its underlying parameters.

Derivatives are essential in gradient-based optimization methods, such as gradient descent, Newton's method, conjugate gradient, and quasi-Newton methods (e.g., BFGS). These techniques use derivatives to determine the direction in which the objective func-

tion decreases most rapidly. Typically, the first derivative (gradient) guides the direction of steepest descent, while the second derivative (Hessian matrix) provides curvature information in second-order methods.

Derivatives are also increasingly used in numerical algorithms for solving Bayesian inverse problems. Modern approaches typically employ gradient-based sampling algorithms such as HMC and its adaptive variant, the NUTS, to explote the posterior. These algorithms depend on computing the gradient of the log-probability (i.e., the log joint density) with respect to the model parameters.

Calculating the automatic differentiation (AD) is already challenging for PDE models—doing so for a coupled probabilistic and PDE model is even more difficult. Many scientific and engineering problems involve such coupling, such as subsurface aquifer modeling, seismic inversion, and weather and climate modeling. Fully integrating PDE frameworks like Firedrake and DOLFINx with machine learning tools such as JAX (Bradbury et al., 2018) and NumPyro (Phan et al., 2019) is challenging, as these systems are complex and developed independently. The goal is to enable end-to-end differentiable workflows that seamlessly combine PDEs with probabilistic components.

pyadjoint (Mitusch et al., 2019) is a Python framework for computing reverse-mode AD (adjoint method) for PDE models expressed in unified form language (UFL). JAX, on the other hand, provides automatic differentiation for models defined within its ecosystem. While we may have a PDE model and its differentiation handled by pyadjoint, we still need to interface it with JAX in order to integrate the PDE solve into NumPyro model. This integration would allow us to incorporate the AHC random model and perform probabilistic inference.

Bouziani et al. (2024) introduces a differentiable programming layer that bridges PDE solvers and machine learning (ML) frameworks, allowing researchers to combine PDEs and ML models with minimal code modifications. Using our approach, it becomes possible to integrate a probabilistic model informed by complex prior knowledge and automatically construct a Bayesian statistical model in NumPyro. This leverages JAX's speed and automatic differentiation capabilities for efficient Bayesian modeling and inference.

Several studies have explored PDE-constrained inverse problems using adjoint-based optimization, particularly in geophysical and environmental modeling. For instance, Pe-

tra et al. (2012) applied an inexact Gauss–Newton method to estimate basal sliding coefficients and rheological parameters in a nonlinear Stokes ice sheet model. Their approach formulates the inversion as a regularized nonlinear least-squares problem, using adjoint equations to efficiently compute gradients and Hessian-vector products. This method shares strong conceptual similarities with our work, where we estimate the anisotropic hydraulic conductivity (AHC) tensor in a time-dependent groundwater flow model. Both approaches rely on sparse observational data, exploit the structure of the forward PDE model, and use gradient-based methods enabled by automatic or algorithmic differentiation.

Our main contribution is the development of a differentiable programming abstraction that enables users to build models combining PDEs and probabilistic components, while maintaining full compatibility with tools such as `jax.grad`, `jax.jit`[1], and `jax.vmap`[2]. In our framework, gradients propagate correctly through both the PDE solver and the probabilistic model. This makes it possible to seamlessly integrate the PDE model into an automatic NumPyro workflow, allowing users to construct Bayesian statistical models and perform probabilistic inference using modern, scalable tools. The approach brings together the strengths of numerical PDE solvers and probabilistic modeling within a unified, gradient-based optimization framework.

To verify the correctness of AD, we apply the Taylor test to the gradient of the posterior in the NumPyro model. The results confirm that the coupling of Firedrake, pyadjoint, JAX, and NumPyro functions correctly. Specifically, the gradient of the posterior, resulting from the integration of the probabilistic model with the PDE model, is accurately computed.

From Chapter 2 and Chapter 3, based on Salehian Ghamsari, Dam, & Hale (2025), we have the forward PDE model of the aquifer system. Additionally, in Chapter 4, based on Salehian Ghamsari, van Dam, & Hale (2025), we defined the probabilistic model of the AHC tensor. In this chapter, we demonstrate the feasibility of integrating a PDE

[1] `jax.jit` is a JAX decorator that compiles a Python function into highly efficient XLA (Accelerated Linear Algebra) code, enabling faster execution by optimizing and fusing operations. It improves performance by just-in-time (JIT) compiling the function the first time it is called.

[2] `jax.vmap` is a JAX transformation that automatically vectorizes a function by mapping it over batch dimensions, allowing for efficient parallel computation without the need for explicit loops. It preserves the function's structure while applying it across inputs in a batched manner.

model implemented in Firedrake, a finite element computing library (Rathgeber et al., 2016), with a probabilistic model built in JAX and Numpyro.

Due to the expense of the PDE solver within the three-dimensional poroelastic model with three-field formulation of Biot's equations, we solve the inverse problem of a two-dimensional aquifer flow model in Firedrake to estimate the AHC tensor. To optimize the objective functional using a gradient-based method, we compute the gradient of the PDE aquifer flow model using pyadjoint. Although this is a simplified version of our poroelastic aquifer model, it retains many of the key challenges found in our PDE poroelastic model, such as time dependency and the presence of the AHC tensor. In the deterministic inversion, the AHC tensor k was parameterized directly by its matrix components rather than by angle and magnitude, providing a simplified and computationally efficient representation of the parameter space.

The results show that the estimated AHC tensor yields fluid pressure values that closely match the synthetic observations.

5.2 Methodology and implementation

In Fig. 5.1, we visualized the hierarchical structure of the NumPyro model as two DAGs. Figure 5.1a illustrates what we have accomplished so far, while Fig. 5.1b shows the overall NumPyro model and the remaining steps needed to fully automate Bayesian inversion. To implement the complete Bayesian inversion system in NumPyro, beyond developing an eigentensor NumPyro model and coupling Firedrake with NumPyro (as shown in Fig. 5.1a), we must determine how to handle multiple outputs in the NumPyro model to account for water level observations from several wells.

In this section, we discuss in detail how we implement various components of the NumPyro model to address the technological challenges. Additionally, we present our method for solving a non-probabilistic inverse problem for a 2D aquifer flow model.

5.2.1 Integration of Firedrake and NumPyro

On our path to solving the Bayesian inversion problem, we encounter several technological challenges, which we address by breaking the problem into smaller subproblems. First, we

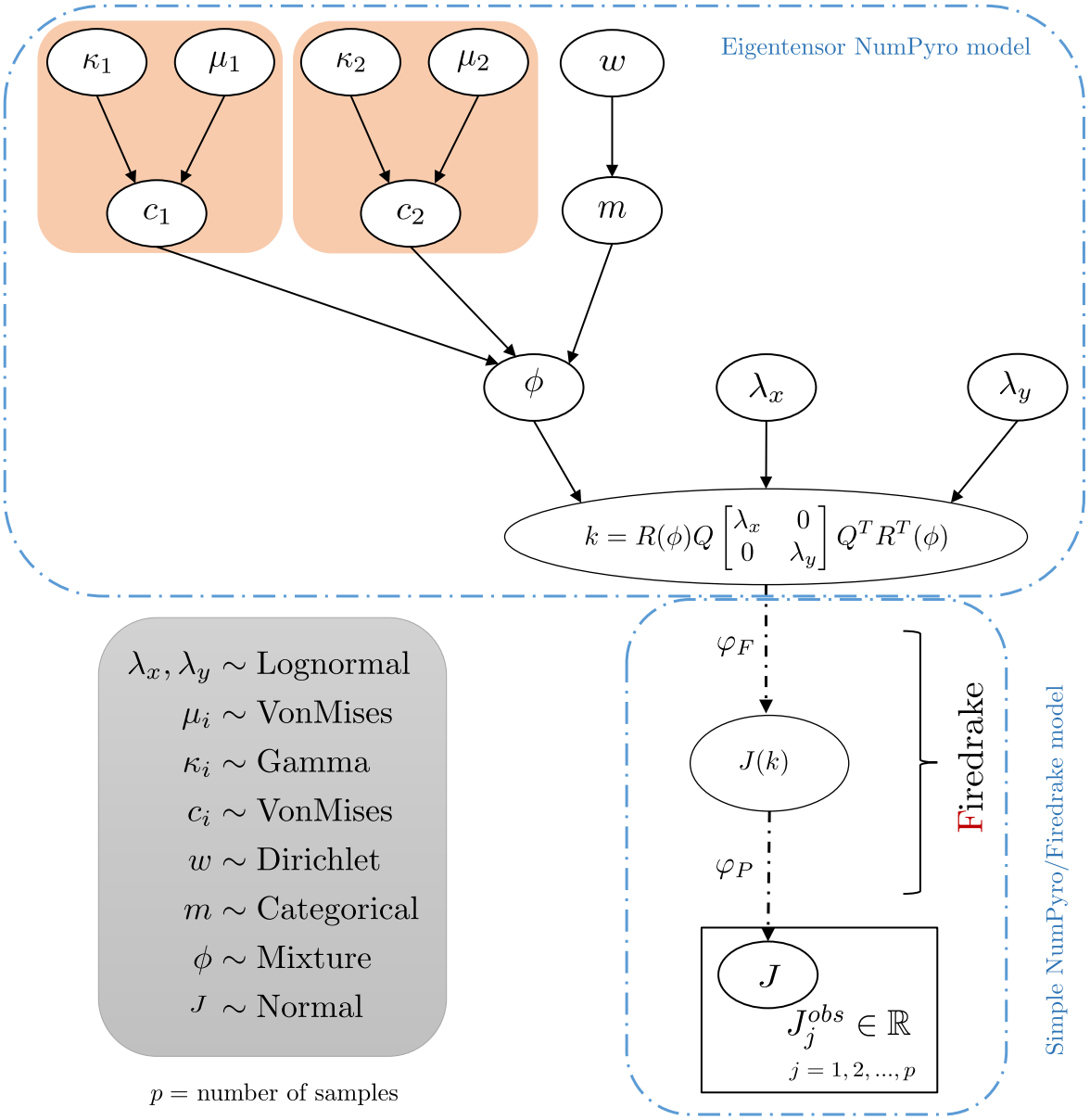

(a) DAG of the probabilistic model for AHC, along with the simplified NumPyro/Firedrake implementation validated in this chapter. J is the assembled objective functional (e.g., data misfit + regularization).

Figure 5.1: Overview of the NumPyro model (part 1).

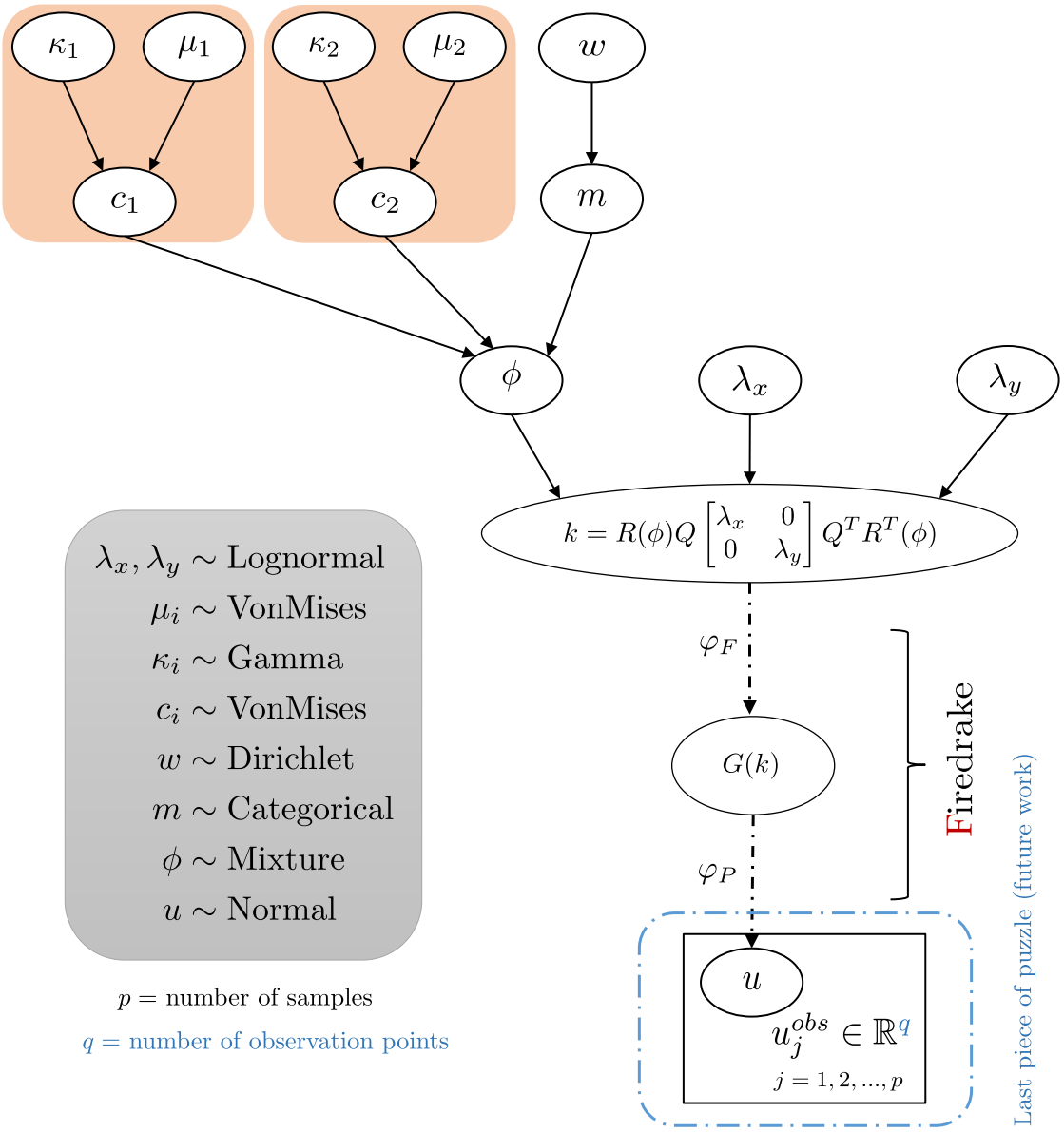

(b) DAG representing the overall structure of the NumPyro model.

Figure 5.1: Overview of the NumPyro model (continued). The process begins with a Bayesian stochastic model for the AHC random tensor, as described in Chapter 4, where ϕ, λ_x, and λ_y represent the rotation angle and eigenvalues in the x and y directions, respectively. The resulting conductivity tensor k is transformed from a JAX tensor to a Firedrake Function via φ_F, then used in a Firedrake FEM model to compute surface displacement on observation points. The displacement u is then mapped back to a JAX tensor using φ_P. This model can be embedded within an MCMC framework to infer ϕ, λ_x, and λ_y, and thus estimate k.

implement the probabilistic AHC model as a standalone component within a NumPyro model. Next, to couple Firedrake with NumPyro, we implement a simple model in Firedrake, embed it into the NumPyro framework, and verify its gradient using the Taylor test.

In Chapter 4, we constructed a NumPyro model for the rotation angle ϕ. To extend this, in this chapter, we add λ_x and λ_y as two separate log-normal distributions and generate k accordingly. However, using λ_x and λ_y directly to construct Λ can lead to label switching, a problem that arises from the symmetry in the model's parameter space. When the model (Λ) is symmetric, the sampler may randomly switch the roles of λ_x and λ_y across posterior samples, making the interpretation of individual parameters ambiguous. To avoid this, we define a difference term $\Delta\lambda$ such that $\lambda_x = \lambda_y + \Delta\lambda$, thereby breaking the symmetry and mitigating label switching.

To compute the AD (adjoint derivatives) for PDE models, we use pyadjoint. Since pyadjoint is not compatible with the updated DOLFINx backend used in FEniCSx, we transitioned to Firedrake, which provides native support for pyadjoint and thus enables adjoint-based PDE-constrained optimization.

The methodology presented in Farrell et al. (2013) introduces an efficient and automated approach for computing adjoint models of time-dependent PDE simulations by reversing the steps of the forward problem. Although the original implementation targets the FEniCS framework, the same conceptual foundation applies to Firedrake through its own integration with the pyadjoint library. Firedrake, like FEniCS, expresses PDEs using a high-level domain-specific language, allowing pyadjoint to record and differentiate the forward solution automatically. This enables users to compute gradients of objective functionals with respect to model parameters in a scalable and efficient way.

For the next subproblem, we aim to build an automated system that computes both the output of the PDE model from Firedrake and its derivative from pyadjoint, all within a NumPyro workflow. Since NumPyro is a probabilistic programming library built on top of JAX, we need to convert our standard Python function into a JAX-compatible one. To achieve this, we use callbacks, which allow Python code to be executed inside a JAX-transformed function. Specifically, `jax.pure_callback()` is suitable for pure

functions—that is, functions without side effects[3].

JAX does not understand the internals of non-JAX functions, but we can still use them by wrapping them with `jax.pure_callback()`. This allows JAX to call the non-JAX function during execution (not during tracing), enabling its use within `jit()` and `vmap()`. However, gradients will not work by default—since `pure_callback()` treats the wrapped function as a black box, JAX cannot compute `grad()` or higher-order derivatives. To address this, we define a custom gradient using `jax.custom_jvp`, which explicitly tells JAX how to compute the derivative. Once this is in place `jax.grad()` can be used.

It's important to note that this method can be slow on GPUs or TPUs because every call to `pure_callback()` involves transferring data from the device to the host to run the non-JAX function, and then sending the result back to the device. This device-host communication introduces overhead on accelerators. On CPUs, however, this cost is minimal since there's no such separation.

In the following, we present the code that implements this setup.

```
# Define the reduced functional:
# J can be the assembled objective functional (e.g., data misfit + regularization), and the controls are the parameters: k_11, k_12, and k_22.
# This sets up the objective in terms of just the control variables, implicitly accounting for the PDE constraints through the adjoint method.
J_reduced = firedrake.adjoint.ReducedFunctional(firedrake.assemble(J), [k_11_control, k_12_control, k_22_control])

# A function to define the inputs of the Firedrake function and calculate the results
def _J(k):
    k_11_firedrake = firedrake.Function(K)
    k_12_firedrake = firedrake.Function(K)
    k_22_firedrake = firedrake.Function(K)
    k_11_firedrake.vector()[:] = k[0]
    k_12_firedrake.vector()[:] = k[1]
```

[3]A side effect is anything your function does other than return a result — like printing, saving, or changing something outside itself.

```
    k_22_firedrake.vector()[:] = k[2]
    return jnp.array(J_reduced([k_11_firedrake, k_12_firedrake,
    k_22_firedrake]), dtype=jnp.float64)

# A function to calculate the derivative of the Firedrake function
    using pyadjoint
def _J_vjp(k, k_dot):
    _J(k)
    return jnp.array(J_reduced.derivative(adj_input=float(k_dot)),
    dtype=jnp.float64)

# Adding the function and its custom gradient using pure_function in
    custom_jvp
@jax.custom_vjp
def J_jax(k):
    result_shape = jax.ShapeDtypeStruct((), k.dtype)
    return jax.pure_callback(_J, result_shape, k)

def _J_fwd(k):
    return J_jax(k), (k)

def _J_vjp_jax(k, k_dot):
    result_shape = jax.ShapeDtypeStruct(k.shape, k.dtype)
    return (jax.pure_callback(_J_vjp, result_shape, k, k_dot),)

J_jax.defvjp(_J_fwd, _J_vjp_jax)
```

We can then use this JAX-transformed function within the NumPyro model, as shown below

```
def simple_model(y_obs):
    mu11 = numpyro.sample("mu11", dist.Normal(0.0, 1.0))
    mu12 = numpyro.sample("mu12", dist.Normal(0.0, 1.0))
    mu22 = numpyro.sample("mu22", dist.Normal(0.0, 1.0))
    mu = jnp.array([mu11, mu12, mu22])
    J = numpyro.deterministic("J", J_jax(mu))
    numpyro.sample("y", dist.Normal(J, 0.01), obs=y_obs)
```

For the final step, we aim to handle multiple outputs from the Firedrake function—specifically, the pressure observations at multiple observation wells—within the NumPyro model (represented by the blue dashed rectangle in Fig. 5.1b). To achieve this, we need to define a vector-valued output in the NumPyro model, replacing the previously used scalar-valued J.

5.2.2 Prototype inverse problem

In addition to our effort for the Bayesian inverse problem, we also implement a non-probabilistic inverse problem for a 2D time-dependent aquifer flow model involving the AHC tensor. After properly setting up the forward problem in Firedrake, we use the adjoint method to compute the AD of the PDE model. We then define a functional J (the loss function) and minimize it to estimate the optimal AHC tensor. In this section, we present the strong and weak forms of the forward problem, followed by the non-dimensionalization process and the formulation of the inverse problem.

Two-dimensional aquifer flow problem statement

We aim to solve the inverse problem for the following 2D aquifer flow model. Given a domain $\Omega_s \subset \mathbb{R}^2$ with boundary Γ_s and outward-pointing normal vector n, find the fluid pore pressure $p_s : \Omega_s \times (0, T] \to \mathbb{R}$ such that

$$S\frac{\partial p_s}{\partial t} - \nabla \cdot (k \nabla p_s) = f_p \text{ on } \Omega_s \times (0, T], \tag{5.1a}$$

with notations and units summarized in Table 5.1, plus boundary conditions

$$p_s = p_d \text{ on } \Gamma_d \times (0, T], \tag{5.1b}$$

$$(-k\nabla p_s) \cdot n = g_p \text{ on } \Gamma_n \times (0, T], \tag{5.1c}$$

and initial condition

$$p_s(x, 0) = p_s^0 \text{ on } \Omega_s. \tag{5.1d}$$

Symbol	Description	values	Units
p_s	fluid pore pressure	output	Pa
f_p	fluid source density	0	s^{-1}
p_r	pumping rate	1	$\mathrm{m}^3\,\mathrm{s}^{-1}$
r	radius of pumping well	0.01	m
g_p	boundary fluid flux	$p_r/\pi r^2$	$\mathrm{m}\,\mathrm{s}^{-1}$
S	Storage coefficient	1	Pa^{-1}
k_{11}	hydraulic conductivity	1	$\mathrm{m}^3\,\mathrm{s}\,\mathrm{kg}^{-1}$
k_{12}	hydraulic conductivity	0.5	$\mathrm{m}^3\,\mathrm{s}\,\mathrm{kg}^{-1}$
k_{22}	hydraulic conductivity	1	$\mathrm{m}^3\,\mathrm{s}\,\mathrm{kg}^{-1}$

Table 5.1: Model parameter used in the 2D aquifer flow model. We simplify the model by rescaling variables and parameters.

The AHC is modeled as a second-rank SPD tensor in the x-y plane.

$$k = \begin{bmatrix} k_{xx} & k_{xy} \\ k_{xy} & k_{yy} \end{bmatrix}.$$

The computational domain and the specified boundary conditions are illustrated in Fig. 5.2a. In practice, measuring pressure requires observation wells placed at specific locations to record water levels. The positions of the synthetic observation wells used in our setup are shown in Fig. 5.2b.

Weak formulation

Before performing the weak form calculation, we need to define a function space for p_s.

$$\mathcal{P}_f = \{p_s : \Omega_s \times [0, T] \to \mathbb{R} \mid p_s \in H^1(\Omega_s)\} \tag{5.2}$$

To derive the weak form, multiply the PDE by a test function $\tilde{p}_s \in \mathcal{P}_f$, and integrate over the domain Ω_s:

$$(S\frac{\partial p_s}{\partial t}, \tilde{p}_s)_{\Omega_s} - (\nabla \cdot (k\nabla p_s), \tilde{p}_s)_{\Omega_s} = (f_p, \tilde{p}_s)_{\Omega_s}, \quad \forall \tilde{p}_s \in \mathcal{P}_f. \tag{5.3}$$

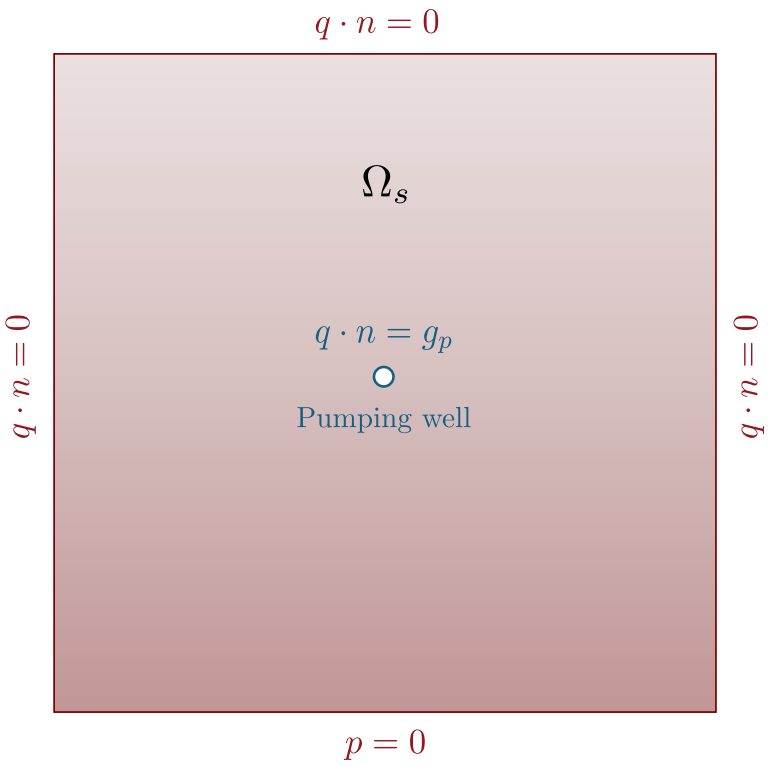

(a) 2D aquifer flow model showing the computational domain, the location of the pumping well, and the specified boundary conditions for both the aquifer boundaries and the pumping well boundaries.

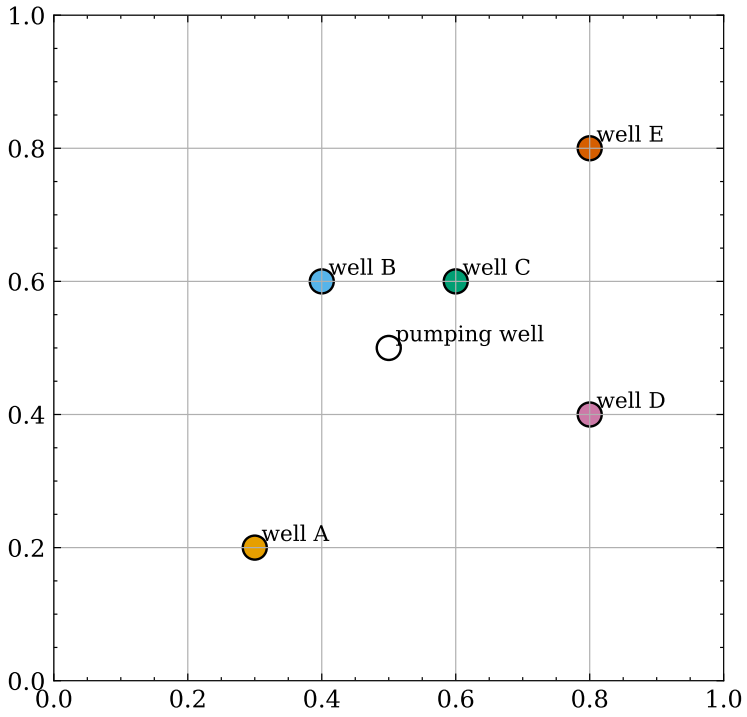

(b) Location of observation wells within the domain (Ω_s).

Figure 5.2: The domain and boundary conditions of the 2D aquifer flow model and the location of synthetic observation wells.

Using integration by parts

$$(\nabla \cdot (k\nabla p_s), \tilde{p}_s)_{\Omega_s} = -((k\nabla p_s), \nabla \tilde{p}_s)_{\Omega_s} + ((k\nabla p_s \cdot n), \tilde{p}_s)_{\Gamma_s}. \tag{5.4}$$

Then since $k\nabla p_s \cdot n = g_p$

$$(S\frac{\partial p_s}{\partial t}, \tilde{p}_s)_{\Omega_s} + ((k\nabla p_s), \nabla \tilde{p}_s)_{\Omega_s} = (f_p, \tilde{p}_s)_{\Omega_s} + (g_p, \tilde{p}_s)_{\Gamma_s}. \tag{5.5}$$

To discretize in time, we apply a first-order backwards Euler method, as described in Section 2.3.4. Considering $M+1$ time steps, the time derivative of the pressure p_s is approximated by

$$\frac{\partial p_s^{n+1}}{\partial t} \approx \frac{p_s^{n+1} - p_s^n}{\Delta t}, \quad \forall n \in 0, \ldots, M-1. \tag{5.6}$$

After time discretization, the problem becomes: for $n = 0, \ldots, M-1$, find $p_s^{n+1} \in \mathcal{P}_f$ such that

$$(S\frac{p_s^{n+1} - p_s^n}{\Delta t}, \tilde{p}_s)_{\Omega_s} + ((k\nabla p_s), \nabla \tilde{p}_s)_{\Omega_s} = (f_p, \tilde{p}_s)_{\Omega_s} + (g_p, \tilde{p}_s)_{\Gamma_s}. \tag{5.7}$$

for all test functions $\tilde{p}_s \in \mathcal{P}_f$.

Synthetic data

To generate synthetic pressure observations at specified observation wells, we adopt the methodology introduced by Nixon-Hill et al. (2024) for consistent point data assimilation in Firedrake. Instead of interpolating model outputs onto the mesh or using smoothed observation fields, we directly evaluate the finite element solution at predefined point locations corresponding to well positions. This is achieved by defining point observations as discontinuous fields supported on disconnected mesh vertices, enabling accurate and stable extraction of model values at arbitrary coordinates. The approach is fully compatible with Firedrake's automatic differentiation stack, allowing us to integrate point-based observations into the inverse problem framework without disrupting gradient computations.

By employing this technique, we ensure that the synthetic observations retain their physical and spatial fidelity, providing a consistent and reliable dataset for validating the inverse estimation of aquifer AHC parameters. This approach allows for precise extraction of simulated pressure values at the exact coordinates of observation wells, avoiding numerical artifacts that can arise from projection or interpolation. Moreover, the method is not limited to pressure data; it is general and versatile enough to be applied to other types of pointwise measurements, such as surface displacement data collected via Global Positioning System (GPS) instruments. This flexibility makes it a powerful tool for incorporating various observational datasets into PDE-constrained inverse problems while maintaining full compatibility with Firedrake's adjoint framework.

Adjoint problem

To solve the inverse problem using gradient-based optimization, we compute the gradient of the objective functional with respect to the control parameters, the components of the AHC tensor. This is efficiently achieved using the adjoint method, which avoids the need for finite differences or solving a sensitivity system for each parameter.

The objective functional is defined as:

$$J(k) = \sum_{n=1}^{N} \sum_{m=1}^{M} \int_{\Omega} \delta(x - x_m) \left(p_s^n(x) - p_{\text{obs},m}^n\right)^2 dx \; + \; \alpha^2 (k_{11}^2 + 2k_{12}^2 + k_{22}^2)\, dx, \tag{5.8}$$

where $p_{\text{obs},m}^n$ are synthetic pressure observations at M observation well locations x_m, $\delta(x - x_m)$ is the Dirac delta ensuring pointwise evaluation, and α is the regularization parameter.

To compute the gradient $\nabla_k J$, we introduce the adjoint variable λ_n, which satisfies the adjoint equation at each time step $n = N, N-1, \ldots, 1$:

$$\int_{\Omega} \frac{S}{\Delta t}(\lambda_n - \lambda_{n+1})\psi \, dx + \int_{\Omega} k \nabla \lambda_n \cdot \nabla \psi \, dx = \sum_{m=1}^{M} \int_{\Omega} 2\, \delta(x - x_m) \left(p_n(x) - p_{\text{obs},m}^n\right) \psi \, dx, \tag{5.9}$$

for all test functions $\psi \in V$, with terminal condition $\lambda_{N+1} = 0$.

The adjoint system runs backward in time and provides the sensitivity of the objective functional to changes in the forward solution. Once the adjoint variables $\{\lambda_n\}$ are computed, the gradient of the objective functional with respect to k is given by:

$$\frac{\delta J}{\delta k} = \sum_{n=1}^{N} \int_{\Omega} \nabla p_n \cdot \nabla \lambda_n \, dx + \frac{\delta J_{\text{reg}}}{\delta k}, \tag{5.10}$$

where $\frac{\delta J_{\text{reg}}}{\delta k}$ is the gradient of the regularization term.

This adjoint-based formulation significantly reduces computational cost and enables efficient solution of the inverse problem using optimization algorithms such as BFGS.

Inverse problem

The inverse problem aims to estimate the spatially constant components of the AHC tensor that best reproduce observed pressure data collected at discrete observation wells over time. While the forward problem computes the pressure field $p_s(x, t)$ based on known physical parameters, initial conditions, and boundary conditions, the inverse problem works in the opposite direction: given noisy pressure observations at specific spatial and temporal locations, the goal is to recover the unknown components of the AHC tensor, k_{11}, k_{12}, and k_{22}.

Building on the foundation of automated adjoint derivation, Funke & Farrell (2013) introduced a framework for PDE-constrained optimization that automates the entire workflow—from forward modeling to gradient evaluation and parameter updates—by leveraging the high-level abstractions of FEniCS and the adjoint capabilities of dolfin-adjoint. Their methodology emphasizes automation and reproducibility, reducing the manual burden on users. Although their implementation is based on FEniCS, the core concepts extend naturally to Firedrake, which shares the same underlying abstraction framework via UFL but employs a different execution backend. In this work, we adopt similar principles using Firedrake, utilizing `pyadjoint` (the successor of `dolfin-adjoint`) to compute derivatives of the PDE-constrained objective functional, enabling efficient gradient-based optimization.

The inverse problem is formulated as the following optimization problem

$$\min_{k} \; J(k) = \sum_{n=1}^{N} \sum_{m=1}^{M} \left(p_s^n(x_m) - p_{\text{obs},m}^n\right)^2 \; + \; \alpha^2 \left(k_{11}^2 + 2k_{12}^2 + k_{22}^2\right), \tag{5.11}$$

subject to the weak form Eq. (5.7).

The first term quantifies the data misfit between predicted and observed pressures, while the second term introduces Tikhonov regularization to promote stability and well-posedness.

5.3 Results

In this section, we apply the Taylor remainder test to verify the correctness of the gradient of the posterior in our simplified Firedrake/NumPyro model. Additionally, we estimate the AHC tensor by solving the inverse problem using synthetic pressure observations generated from the model.

5.3.1 Taylor test for derivative verification

The Taylor test is a numerical technique used to verify the correctness of computed derivatives, such as gradients or Jacobians. It is especially useful in contexts involving automatic differentiation or PDE-constrained optimization. The core idea is that if a function's derivative is correct, then small perturbations in the input should produce changes in the output that match the prediction from a Taylor series expansion.

Consider a scalar-valued function $f(x)$, where $x \in \mathbb{R}^n$, and suppose we want to test the correctness of its gradient $\nabla f(x)$. Let δx be a small perturbation direction and h a scalar step size. The first-order Taylor expansion of f around x gives:

$$f(x + h\,\delta x) = f(x) + h\,\nabla f(x)^\top \delta x + \mathcal{O}(h^2). \tag{5.12}$$

Subtracting the linear approximation yields the first-order Taylor remainder:

$$R(h) = f(x + h\,\delta x) - f(x) - h\,\nabla f(x)^\top \delta x. \tag{5.13}$$

If the gradient $\nabla f(x)$ is correct, then the remainder $R(h)$ should decrease quadratically as $h \to 0$, i.e.,

$$R(h) = \mathcal{O}(h^2). \tag{5.14}$$

This behavior indicates that the gradient correctly captures the local linear behavior of the function.

Zeroth-Order Taylor Test. A simpler baseline check is the zeroth-order Taylor test, which omits the gradient term and focuses solely on the function values

$$R_0(h) = f(x + h\,\delta x) - f(x). \tag{5.15}$$

This test is expected to show *linear* convergence with respect to h, i.e.,

$$R_0(h) = \mathcal{O}(h). \tag{5.16}$$

By comparing the zeroth- and first-order tests, we gain a useful diagnostic tool: if $R_0(h) \sim \mathcal{O}(h)$, the function is continuous, and if $R(h) \sim \mathcal{O}(h^2)$, the gradient is likely implemented correctly.

Figure 5.3 presents both the first-order and zeroth-order Taylor remainders of the simple Firedrake/NumPyro model. The observed convergence rates are 0.98 for the zeroth-order test and 1.99 for the first-order test. As expected, the zeroth-order error exhibits linear convergence—corresponding to a slope of 1 on a log-log plot—while the first-order error demonstrates quadratic convergence with a slope of 2. These results confirm the correctness of the computed gradient.

5.3.2 Estimation of AHC tensor

Figure 5.4 shows the simulated pressure field (p_s) from our 2D aquifer flow model after pumping. The elliptical shape of the pressure distribution reflects the underlying AHC oriented at a 45 deg angle to the x-axis. This figure illustrates how the forward model behaves and demonstrates the influence of the AHC tensor on the resulting pressure field.

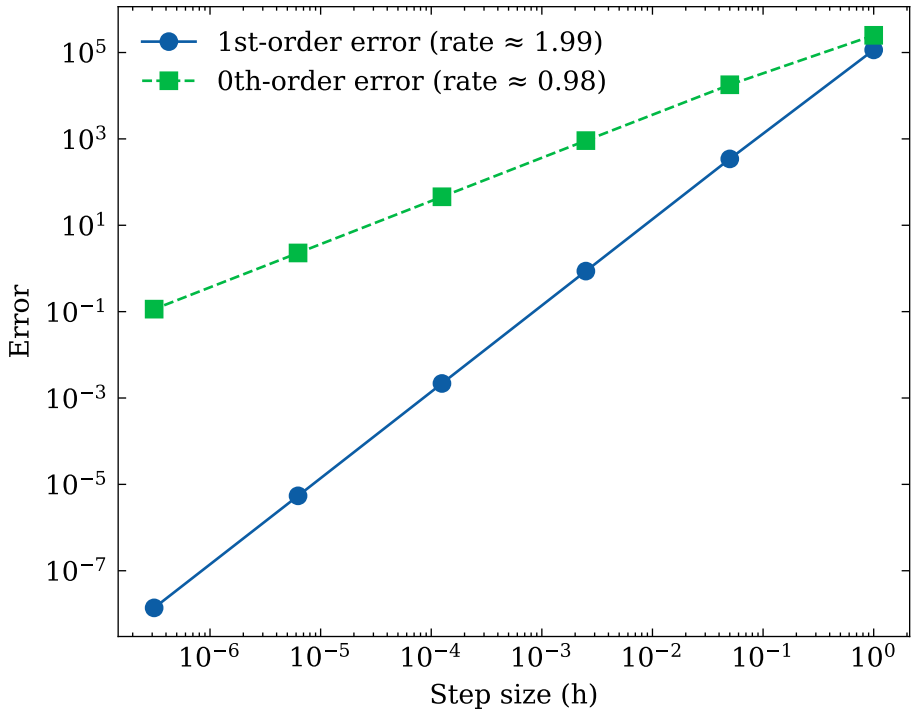

Figure 5.3: Taylor test results for the simple Firedrake model within the NumPyro framework. The zeroth-order (uncorrected) Taylor error is shown as the rectangular orange line, and the first-order (gradient-corrected) error is shown as the circled blue line. The observed error reduction rates are 0.98 for the zeroth-order and 1.99 for the first-order. As expected, the zeroth-order error decreases linearly (slope of 1 on a log-log plot), and the first-order error decreases quadratically (slope of 2), validating the correctness of the gradient implementation.

By minimizing the objective functional J, we obtain an estimate of the AHC tensor. Figure 5.5 illustrates the convergence trend of $J(k)$ over 33 iterations, while Table 5.2 compares the true and estimated values of the AHC tensor obtained by solving the inverse problem. The results indicate that the inverse approach yields an accurate estimation of the AHC tensor.

In Fig. 5.6, we present synthetic pressure observations alongside predicted pressures computed using the estimated AHC tensor from Table 5.2, shown over time at the observation wells. The close agreement between observed and predicted pressures validates the results of the inverse problem.

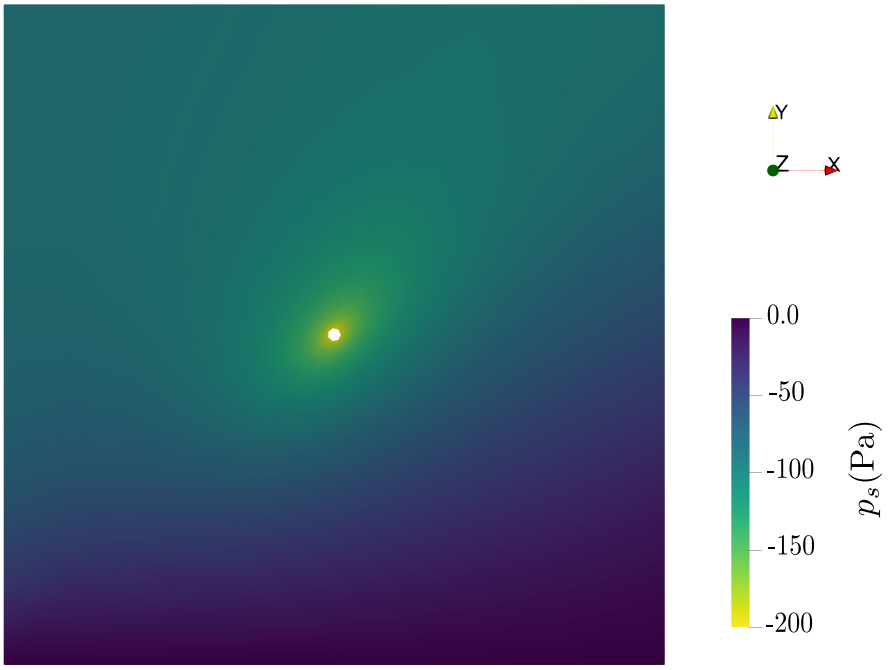

Figure 5.4: Pressure in a 2D aquifer flow model after pumping, computed for a groundwater flow problem. The elliptical pattern in the pressure field reflects the anisotropic behavior introduced by the AHC tensor in the aquifer.

Estimated parameter	True value	Estimated value
k_{11}	1.0	0.915
k_{12}	0.5	0.473
k_{22}	1.0	1.013

Table 5.2: Results of the inverse problem, showing a close estimation of the AHC tensor.

5.4 Conclusion

In this chapter, we addressed the technological and methodological challenges involved in integrating PDE-based models with probabilistic programming frameworks for Bayesian inversion. We demonstrated how the Firedrake and pyadjoint frameworks can be coupled with NumPyro through JAX's callback mechanisms, enabling automatic differentiation and gradient-based inference in complex physical models.

To validate the correctness of computed gradients, we applied the Taylor test and confirmed the expected convergence behavior, reinforcing the reliability of our gradient

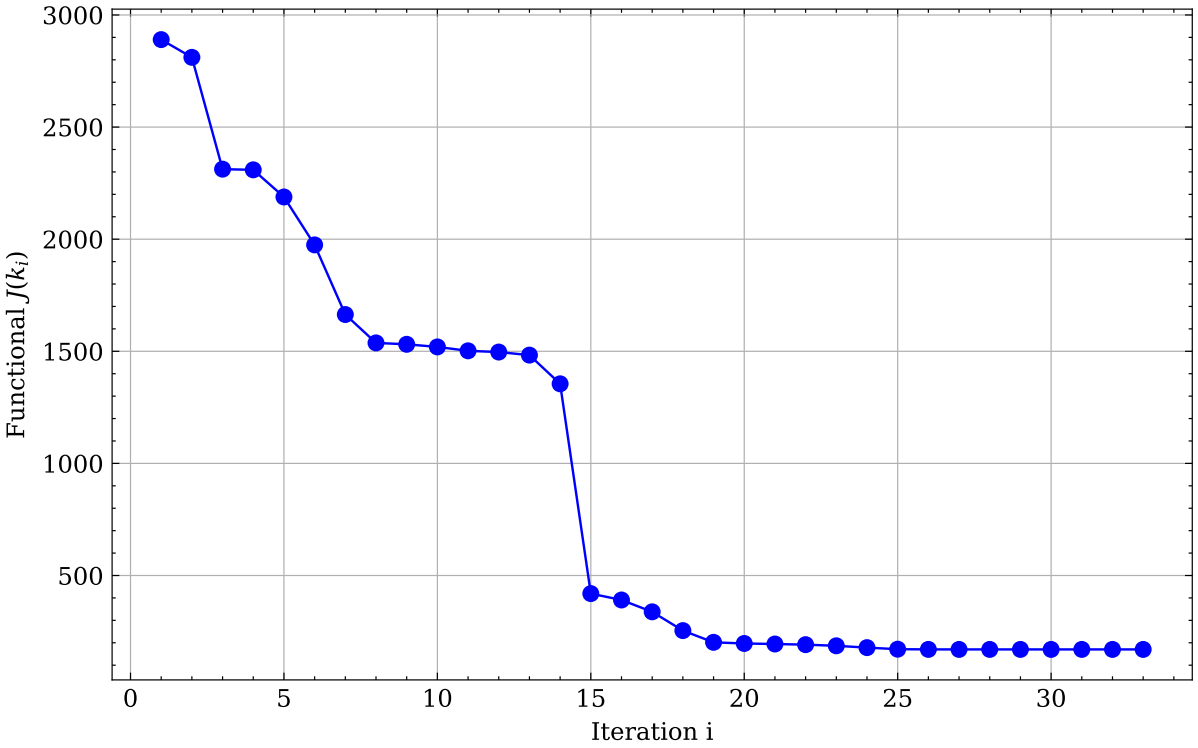

Figure 5.5: Convergence of objective function $J(k)$ over iterations.

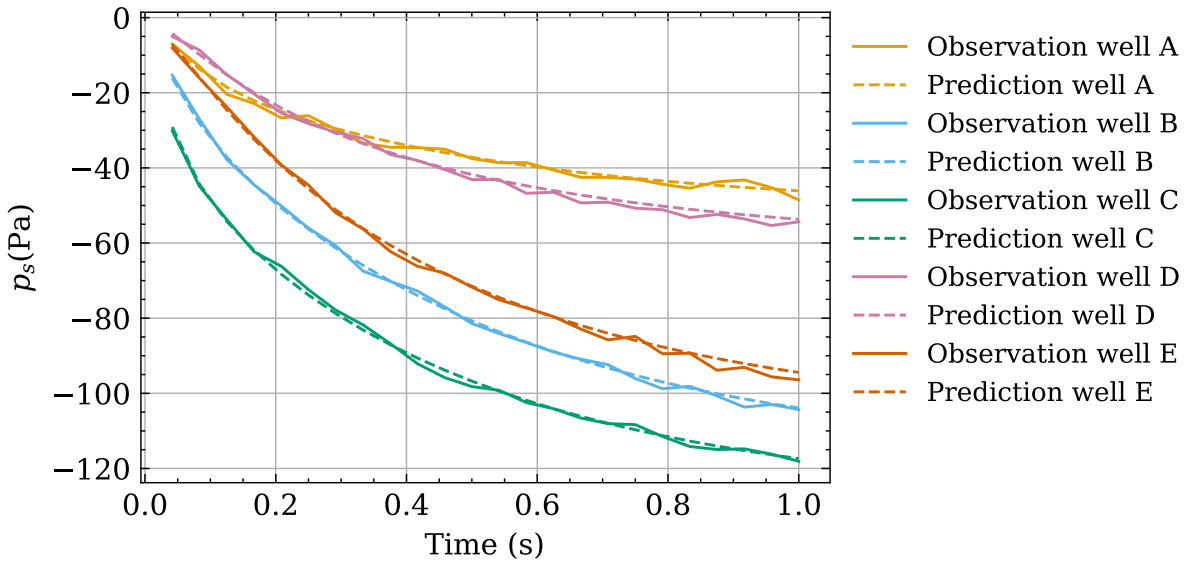

Figure 5.6: Comparison of synthetic pressure observations (solid lines) and predicted pressure using the estimated anisotropic hydraulic conductivity tensor (dashed lines). Each color corresponds to data from a different observation well. This figure demonstrates the effectiveness of the inverse modeling approach in reproducing observed data.

computations. Furthermore, we implemented a deterministic inverse problem for a time-dependent 2D aquifer flow model, successfully estimating the anisotropic hydraulic con-

ductivity (AHC) tensor using synthetic pressure data. The estimated parameters closely matched the true values, and the predicted pressure fields aligned well with synthetic observations, demonstrating the accuracy and effectiveness of the results.

Overall, this work provides a foundation for building scalable, differentiable, and probabilistically robust inverse modeling pipelines in computational hydrology and beyond. The methods developed here pave the way for fully automated Bayesian inversion workflows that integrate complex PDE solvers with modern probabilistic inference tools.

For future work, we plan to complete the implementation of the final component of the NumPyro model—support for vector-valued outputs—to enable fully automated Bayesian calibration. Additionally, we aim to explore the use of Stein Variational Gradient Descent (Stein variational gradient descent (SVGD)) as a means of accelerating posterior approximation within the MCMC framework.

Chapter 6

Conclusions and future work

6.1 Conclusions

This thesis aimed to explore how InSAR satellite data can enhance our understanding of aquifer system properties, with a particular focus on AHC. We began by discussing the motivation behind this research, reviewing relevant literature, and outlining our key contributions.

In Chapter 2, we provided a brief introduction to poroelasticity theory and the FEM framework, followed by a presentation of Biot's poroelasticity equations. We introduced an anisotropic poroelastic finite element model capable of simulating coupled fluid flow and solid displacements. Furthermore, we discretized the three-field Biot poroelasticity model in both space and time using finite element discretization and the backward Euler method, respectively.

In Chapter 3, we proposed an anisotropic poroelastic finite element model designed to replicate the key characteristics of the 1994 Anderson Junction aquifer test, incorporating a 24 to 1 anisotropy ratio. Using this model setup, the simulation shows that the surface displacement resulting from the original Anderson Junction aquifer test (V. M. Heilweil & Hsieh, 2006) was insufficient to be detected by InSAR. To further explore the relationship between AHC and surface displacement, we simulated different anisotropy ratios and analyzed the resulting displacement patterns. Our findings indicate that, even when assuming isotropic elasticity, the elastic response of the Earth's surface exhibits an elliptical displacement pattern. A key strength of our model is its adaptability, as it can be modi-

fied for different aquifer tests or alternative aquifer settings with varying hydrogeological properties. To assess the potential of InSAR data for calibrating anisotropic aquifer models, we examined three alternative scenarios involving extended pumping durations and/or higher pumping rates. Our results demonstrate that in two of these scenarios, the predicted LOS displacement would be detectable by Sentinel-1 InSAR data.

In Chapter 4, we developed a flexible stochastic prior model for the AHC tensor that maintains its inherent symmetry and positive definiteness. The model emphasizes the incorporation of AHC uncertainty in a way that allows independent control over both the scaling and directional properties of the tensor, while preserving the material's symmetry. To generate rotation angles for the direction of AHC tensor, we applied a mixture of two von Mises models, which effectively represent the bimodality observed in fracture outcrop data. We consider two states of belief: one that incorporates the findings of V. M. Heilweil & Hsieh (2006), and another that excludes them. These differing assumptions introduce uncertainty in the AHC, which we propagate through a PDE-based model of the Anderson Junction site. The results demonstrate that our approach serves as a flexible tool for capturing the effects of uncertain AHC on LOS surface displacements.

In Chapter 5, we developed and validated a computational framework that integrates a finite element PDE solver (Firedrake) with a probabilistic programming environment (JAX/NumPyro). We demonstrated the correctness of our PDE–probabilistic coupling using the Taylor test, ensuring accurate gradient propagation through the posterior. Additionally, we solved a deterministic inverse problem using adjoint-based optimization to estimate AHC components from synthetic pressure observations generated within the Firedrake environment. The close agreement between estimated and true values confirmed the reliability of the inversion. This work lays the foundation for future Bayesian inference with more complex models and real-world datasets, providing a scalable and extensible platform for uncertainty-aware groundwater modeling.

6.1.1 Future work

The primary limitation of this thesis lies in data availability. Below, we outline these constraints along with recommendations for future research, emphasizing opportunities

for further advancements.

1. There is no existing InSAR dataset for the Anderson Junction aquifer test with a 24:1 anisotropy ratio. To address this limitation and apply real data to our poroelastic finite element model, we propose two potential solutions:

   - Conducting a new aquifer pumping test: Performing a new aquifer pumping test at Anderson Junction, following one of the two recommended scenarios, could produce necessary data for validation.
   - Identifying an alternative site: Finding an existing aquifer pumping test in a region with a known anisotropic (fractured) aquifer with the considerations mentioned in Section 3.5.4 could provide suitable data for validation.

   By implementing either of these solutions, we can integrate InSAR data into our proposed aquifer model. This process involves collecting and processing multiple datasets, including field measurements, remote sensing data (InSAR, GPS), and hydrogeological information. Solving the proposed Bayesian inversion using these multidimensional datasets would enable the estimation of aquifer properties, as demonstrated in Alghamdi et al. (2020, 2021). These efforts have the potential to significantly improve our understanding of aquifers exhibiting AHC behavior, ultimately leading to more accurate predictive models for groundwater management.

2. Generating a time series of LOS displacement from InSAR data requires a long-duration pumping test to acquire a greater number of InSAR data pairs. A longer pumping test enables the collection of more InSAR images, which in turn improves the temporal resolution of surface displacement measurements. By leveraging InSAR time series, we can track surface displacement with higher accuracy (Li et al., 2022). Moreover, incorporating these time-series data into inverse modeling allows for a more precise estimation of aquifer properties.

3. Future work could also extend the model to account for inelastic deformation of the aquifer system by incorporating an inelasticity term, such as plasticity or viscoplasticity. Inelastic deformation develops over long timescales due to prolonged

groundwater extraction or increased water injection, whether artificial or natural. Investigating different constitutive models for inelastic behavior and validating them against field observations and geodetic data could significantly improve the predictive accuracy of aquifer deformation under long-term discharge and recharge conditions.

4. Another direction to explore is the impact of loading displacement caused by the weight of water (precipitation) or snow on the aquifer. This can be incorporated into Biot's poroelastic equations as boundary conditions or source terms. By modeling these effects, we could gain a better understanding of aquifer behavior under varying surface loads, such as seasonal variations or climate impacts. This approach would also improve the prediction of land subsidence, particularly in areas affected by heavy precipitation or snowmelt.

5. To increase the realism of our AHC stochastic model, we could introduce an additional rotation angle in the direction of the z axis. In this case, the AHC tensor would become a 3x3 tensor, extending the anisotropy into three dimensions. To account for the new rotation angle, we can develop another Bayesian model using a circular von Mises distribution for this angle. This model could then be integrated into the existing SPD tensor framework. By doing so, we would better capture the full anisotropic behavior of the aquifer, enabling a more accurate representation of the hydraulic conductivity tensor and its impact on the aquifer system.

6. By successfully coupling PDE-based models with probabilistic models, we move toward the development of an automated Bayesian inversion framework. With the final component—support for vector-valued outputs in the NumPyro model—addressed in Chapter 5, we complete the pipeline necessary for fully automated uncertainty quantification. This enables the use of MCMC methods to explore the posterior distribution of model parameters, providing a principled approach to quantify uncertainty in aquifer hydraulic conductivity estimates.

References

Adler, P. M., & Thovert, J.-F. (2013). *Fractures and fracture networks* (Vol. 15). Springer Science & Business Media. doi: 10.1007/978-94-017-1599-7

Akaike, H. (1998). Information theory and an extension of the maximum likelihood principle. In *Selected papers of Hirotugu Akaike* (pp. 199–213). Springer. doi: 10.1007/978-1-4612-1694-0_15

Alghamdi, A. (2020). *Bayesian inverse problems for quasi-static poroelasticity with application to ground water aquifer characterization from geodetic data* (Thesis, University of Texas at Austin). doi: 10.26153/tsw/13182

Alghamdi, A., Hesse, M. A., Chen, J., & Ghattas, O. (2020). Bayesian Poroelastic Aquifer Characterization From InSAR Surface Deformation Data. Part I: Maximum A Posteriori Estimate. *Water Resources Research*, *56*(10), e2020WR027391. doi: 10.1029/2020WR027391

Alghamdi, A., Hesse, M. A., Chen, J., & Ghattas, O. (2024). Advancing aquifer characterization through the integration of satellite geodesy, geomechanics, and bayesian inference. *Authorea Preprints*. doi: 10.22541/essoar.172988076.62528060/v1

Alghamdi, A., Hesse, M. A., Chen, J., Villa, U., & Ghattas, O. (2021). Bayesian Poroelastic Aquifer Characterization From InSAR Surface Deformation Data. 2. Quantifying the Uncertainty. *Water Resources Research*, *57*(11), e2021WR029775. doi: 10.1029/2021WR029775

Amitrano, D., Martino, G. D., Iodice, A., Mitidieri, F., Papa, M. N., Riccio, D., & Ruello, G. (2014). Sentinel-1 for monitoring reservoirs: A performance analysis. *Remote Sensing*, *6*(11), 10676–10693. doi: 10.3390/rs61110676

Aris, R. (2012). *Vectors, Tensors and the Basic Equations of Fluid Mechanics*. Courier Corporation.

Axler, S. (2024). *Linear algebra done right*. Springer Nature. doi: 10.1007/978-3-031-41026-0

Bamler, R., & Hartl, P. (1998). Synthetic aperture radar interferometry. *Inverse problems*, *14*(4), R1. doi: 10.1088/0266-5611/14/4/001

Baratta, I. A., Dean, J. P., Dokken, J. S., Habera, M., Hale, J. S., Richardson, C. N., ... Wells., G. N. (2023). Dolfinx: The next generation fenics problem solving environment. *Zenodo*. doi: 10.5281/zenodo.10447666

Basu, N. B., & Van Meter, K. (2014, January). 4.3 - Sustainability of Groundwater Resources. In S. Ahuja (Ed.), *Comprehensive Water Quality and Purification* (pp. 57–75). Waltham: Elsevier. doi: 10.1016/B978-0-12-382182-9.00062-1

Bathe, K.-J. (2006). *Finite element procedures*. Klaus-Jurgen Bathe.

Batzle, M., Duranti, L., Rector, J., & Pride, S. (2007, December). *Measurment and Interpretation of Seismic Attenuation for Hydrocarbon Exploration* (Tech. Rep.). Colorado School of Mines, Golden, CO (United States). doi: 10.2172/927592

Berre, I., Doster, F., & Keilegavlen, E. (2019, October). Flow in Fractured Porous Media: A Review of Conceptual Models and Discretization Approaches. *Transport in Porous Media*, *130*(1), 215–236. doi: 10.1007/s11242-018-1171-6

Biot, M. A. (1941, February). General Theory of Three-Dimensional Consolidation. *Journal of Applied Physics*, *12*(2), 155–164. doi: 10.1063/1.1712886

Bishop, C. M. (2006). *Pattern Recognition and Machine Learning* (1st ed.). Springer New York, NY. Retrieved 2025-01-13, from `https://link.springer.com/book/9780387310732`

Blei, D. M., Kucukelbir, A., & McAuliffe, J. D. (2017a). Variational inference: A review for statisticians. *Journal of the American Statistical Association*, *112*(518), 859–877. doi: 10.1080/01621459.2017.1285773

Blei, D. M., Kucukelbir, A., & McAuliffe, J. D. (2017b, April). Variational Inference: A Review for Statisticians. *Journal of the American Statistical Association*, *112*(518), 859–877. doi: 10.1080/01621459.2017.1285773

Bonì, R., Cigna, F., Bricker, S., Meisina, C., & McCormack, H. (2016, September). Characterisation of hydraulic head changes and aquifer properties in the London Basin using Persistent Scatterer Interferometry ground motion data. *Journal of Hydrology*, *540*, 835–849. doi: 10.1016/j.jhydrol.2016.06.068

Bonì, R., Meisina, C., Cigna, F., Herrera, G., Notti, D., Bricker, S., ... Ezquerro, P. (2017). Exploitation of Satellite A-DInSAR Time Series for Detection, Characterization and Modelling of Land Subsidence. *Geosciences*, *7*(2). doi: 10.3390/geosciences7020025

Bonì, R., Meisina, C., Teatini, P., Zucca, F., Zoccarato, C., Franceschini, A., ... Herrera, G. (2020). 3d groundwater flow and deformation modelling of madrid aquifer. *Journal of Hydrology*, *585*, 124773. doi: https://doi.org/10.1016/j.jhydrol.2020.124773

Bouziani, N., & Ham, D. A. (2023). Physics-driven machine learning models coupling PyTorch and Firedrake. In *ICLR 2023 Workshop on Physics for Machine Learning*. doi: 10.48550/arXiv.2303.06871

Bouziani, N., Ham, D. A., & Farsi, A. (2024). *Differentiable programming across the pde and machine learning barrier.* doi: 10.48550/arXiv.2409.06085

Bovenga, F., Nitti, D. O., Fornaro, G., Radicioni, F., Stoppini, A., & Brigante, R. (2013). Using c/x-band sar interferometry and gnss measurements for the assisi landslide analysis. *International Journal of Remote Sensing*, *34*(11), 4083-4104. doi: 10.1080/01431161.2013.772310

Bradbury, J., Frostig, R., Hawkins, P., Johnson, M. J., Leary, C., Maclaurin, D., ... Zhang, Q. (2018). *JAX: composable transformations of Python+NumPy programs.* Retrieved from `http://github.com/jax-ml/jax`

Brenner, S. C., & Scott, L. R. (2008). *The Mathematical Theory of Finite Element Methods* (Vol. 15; J. E. Marsden, L. Sirovich, & S. S. Antman, Eds.). New York, NY: Springer. doi: 10.1007/978-0-387-75934-0

Brezzi, F., Douglas, J., & Marini, L. D. (1985). Two families of mixed finite elements for second order elliptic problems. *Numerische Mathematik*, *47*, 217–235. doi: 10.1007/BF01389710

Burbey, T. J. (2006, November). Three-dimensional deformation and strain induced by municipal pumping, Part 2: Numerical analysis. *Journal of Hydrology*, *330*(3), 422–434. doi: 10.1016/j.jhydrol.2006.03.035

Burbey, T. J., Warner, S. M., Blewitt, G., Bell, J. W., & Hill, E. (2006, March). Three-dimensional deformation and strain induced by municipal pumping, part 1: Analysis of field data. *Journal of Hydrology*, *319*(1), 123–142. doi: 10.1016/j.jhydrol.2005.06.028

Caretta, M., Mukherji, A., Arfanuzzaman, M., Betts, R., Gelfan, A., Hirabayashi, Y., ... Supratid, S. (2022). *Water. In: Climate Change 2022: Impacts, Adaptation and Vulnerability* (Tech. Rep.). Cambridge University Press, Cambridge, UK and New York, NY, USA. doi: 10.1017/9781009325844.006

Carrera, J., Alcolea, A., Medina, A., Hidalgo, J., & Slooten, L. J. (2005, March). Inverse problem in hydrogeology. *Hydrogeology Journal*, *13*(1), 206–222. doi: 10.1007/s10040-004-0404-7

Chaussard, E., Bürgmann, R., Shirzaei, M., Fielding, E. J., & Baker, B. (2014). Predictability of hydraulic head changes and characterization of aquifer-system and fault properties from InSAR-derived ground deformation. *Journal of Geophysical Research: Solid Earth*, *119*(8), 6572-6590. doi: 10.1002/2014JB011266

Cheng, C. H., & Toksöz, M. N. (1979). Inversion of seismic velocities for the pore aspect ratio spectrum of a rock. *Journal of Geophysical Research: Solid Earth*, *84*(B13), 7533–7543. doi: 10.1029/JB084iB13p07533

Chouly, F., Hild, P., & Renard, Y. (2015). Symmetric and non-symmetric variants of Nitsche's method for contact problems in elasticity: theory and numerical experiments. *Mathematics of Computation*, *84*(293), 1089–1112. doi: 10.1090/S0025-5718-2014-02913-X

Cigna, F., Esquivel Ramírez, R., & Tapete, D. (2021). Accuracy of Sentinel-1 PSI and SBAS InSAR Displacement Velocities against GNSS and Geodetic Leveling Monitoring Data. *Remote Sensing*, *13*(23). doi: 10.3390/rs13234800

Cook, E. (1960). *Geologic map of Washington county, Utah.* Utah Geological and Mineralogical Survey. Retrieved from `https://www.utahmapstore.com/`

Cowin, S. C., & Doty, S. B. (2007). *Tissue mechanics*. Springer. doi: 10.1007/978-0-387-49985-7

Davis, J. C. (2002). *Statistics and Data Analysis in Geology* (Third ed.). Wiley New York.

Dehghani, H., Penta, R., & Merodio, J. (2018, dec). The role of porosity and solid matrix compressibility on the mechanical behavior of poroelastic tissues. *Materials Research Express*, *6*(3), 035404. doi: 10.1088/2053-1591/aaf5b9

Dokken, J. S. (2024, April). ADIOS4DOLFINx: A framework for checkpointing in FEniCS. *Journal of Open Source Software*, *9*(96), 6451. Retrieved from `https://joss.theoj.org/papers/10.21105/joss.06451` doi: 10.21105/joss.06451

Duan, W., Zhang, H., Wang, C., & Tang, Y. (2020). Multi-temporal insar parallel processing for sentinel-1 large-scale surface deformation mapping. *Remote Sensing*, *12*(22). doi: 10.3390/rs12223749

Duane, S., Kennedy, A. D., Pendleton, B. J., & Roweth, D. (1987, September). Hybrid Monte Carlo. *Physics Letters B*, *195*(2), 216–222. doi: 10.1016/0370-2693(87)91197-X

Earle, S. (2019, sep). *14.1 Groundwater and Aquifers.* Retrieved 2023-11-29, from `https://opentextbc.ca/physicalgeology2ed/chapter/14-1-groundwater-and-aquifers/`

Erkens, G., Bucx, T., Dam, R., de Lange, G., & Lambert, J. (2015). Sinking coastal cities. *Proceedings of the International Association of Hydrological Sciences*, *372*, 189–198. doi: 10.5194/piahs-372-189-2015

European Space Agency (ESA). (2023). *User Guides - Sentinel-1 SAR - Interferometric Wide Swath - Sentinel Online.* ESA Sentinel Online. Retrieved 2023-07-03, from `https://sentinels.copernicus.eu/web/sentinel/user-guides`

Famiglietti, J. S., Lo, M., Ho, S. L., Bethune, J., Anderson, K. J., Syed, T. H., ... Rodell, M. (2011). Satellites measure recent rates of groundwater depletion in California's Central Valley. *Geophysical Research Letters*, *38*(3). doi: 10.1029/2010GL046442

Farrell, P., Ham, D., Funke, S., & Rognes, M. (2013, January). Automated Derivation of the Adjoint of High-Level Transient Finite Element Programs. *SIAM Journal on Scientific Computing*, *35*(4), C369–C393. doi: 10.1137/120873558

Fernández-Martínez, J. L., Fernández-Muñiz, Z., Pallero, J. L. G., & Pedruelo-González, L. M. (2013, November). From Bayes to Tarantola: New insights to understand uncertainty in inverse problems. *Journal of Applied Geophysics*, *98*, 62–72. doi: 10.1016/j.jappgeo.2013.07.005

Ferronato, M., Castelletto, N., & Gambolati, G. (2010, June). A fully coupled 3-D mixed finite element model of Biot consolidation. *Journal of Computational Physics*, *229*(12), 4813–4830. doi: 10.1016/j.jcp.2010.03.018

Fienen, M. N., Kitanidis, P. K., Watson, D., & Jardine, P. (2004, January). An Application of Bayesian Inverse Methods to Vertical Deconvolution of Hydraulic Conductivity in a Heterogeneous Aquifer at Oak Ridge National Laboratory. *Mathematical Geology*, *36*(1), 101–126. doi: 10.1023/B:MATG.0000016232.71993.bd

Food and Agriculture Organization of the United Nations (FAO). (2022). *Water.* Retrieved 2022-09-09, from `http://www.fao.org/water/en/`

Friel, N., & Pettitt, A. N. (2008, July). Marginal Likelihood Estimation via Power Posteriors. *Journal of the Royal Statistical Society Series B: Statistical Methodology*, *70*(3), 589–607. Retrieved 2024-12-17, from `https://doi.org/10.1111/j.1467-9868.2007.00650.x` doi: 10.1111/j.1467-9868.2007.00650.x

Fuhrmann, T., & Garthwaite, M. C. (2019, January). Resolving Three-Dimensional Surface Motion with InSAR: Constraints from Multi-Geometry Data Fusion. *Remote Sensing*, *11*(3), 241. doi: 10.3390/rs11030241

Funke, S. W., & Farrell, P. E. (2013, February). A framework for automated PDE-constrained optimisation. *arXiv:1302.3894 [cs]*. Retrieved 2014-11-28, from `http://arxiv.org/abs/1302.3894` (arXiv: 1302.3894)

Galloway, D. L., & Burbey, T. J. (2011, December). Review: Regional land subsidence accompanying groundwater extraction. *Hydrogeology Journal*, *19*(8), 1459–1486. doi: 10.1007/s10040-011-0775-5

Galloway, D. L., & Hoffmann, J. (2007, February). The application of satellite differential SAR interferometry-derived ground displacements in hydrogeology. *Hydrogeology Journal*, *15*(1), 133–154. doi: 10.1007/s10040-006-0121-5

Galloway, D. L., Jones, D. R., & Ingebritsen, S. E. (1999). *Land subsidence in the United States* (Vol. 1182). Geological Survey (USGS). doi: 10.3133/cir1182

Gambolati, G., & Teatini, P. (2015). Geomechanics of subsurface water withdrawal and injection. *Water Resources Research*, *51*(6), 3922-3955. doi: 10.1002/2014WR016841

Gelman, A., Hwang, J., & Vehtari, A. (2014). Understanding predictive information criteria for bayesian models. *Statistics and Computing*, *24*, 997–1016. doi: 10.1007/s11222-013-9416-2

Gelman, A., Vehtari, A., Simpson, D., Margossian, C. C., Carpenter, B., Yao, Y., ... Modrák, M. (2020, November). *Bayesian Workflow* (Tech. Rep.). arXiv. doi: 10.48550/arXiv.2011.01808

George, N., Akpan, A., George, A., & Obot, I. (2010, January). Determination of elastic properties of the overburden materials in parts of Akamkpa, southeastern Nigeria using seismic refraction studies. *Archives of Physics Research*, *1*, 58–71. (ISSN: 0976-0970)

Geuzaine, C., & Remacle, J.-F. (2009). Gmsh: A 3-D finite element mesh generator with built-in pre- and post-processing facilities. *International Journal for Numerical Methods in Engineering*, *79*(11), 1309-1331. doi: 10.1002/nme.2579

Guilleminot, J., & Soize, C. (2012). Stochastic modeling of anisotropy in multiscale analysis of heterogeneous materials: A comprehensive overview on random matrix approaches. *Mechanics of Materials*, *44*(SI), 35–46. doi: 10.1016/j.mechmat.2011.06.003

Guo, L., Gong, H., Zhu, F., Zhu, L., Zhang, Z., Zhou, C., ... Sun, Y. (2019). Analysis of the spatiotemporal variation in land subsidence on the Beijing Plain, china. *Remote Sensing*, *11*(10). doi: 10.3390/rs11101170

Guo, Q., Huang, J., Zhou, Z., & Wang, J. (2019). Experiment and Numerical Simulation of Seawater Intrusion under the Influences of Tidal Fluctuation and Groundwater Exploitation in Coastal Multilayered Aquifers. *Geofluids*. doi: 10.1155/2019/2316271

Gupta, H. K. (2002). A review of recent studies of triggered earthquakes by artificial water reservoirs with special emphasis on earthquakes in koyna, india. *Earth-Science Reviews*, *58*(3), 279-310. doi: 10.1016/S0012-8252(02)00063-6

Guzy, A., & Malinowska, A. A. (2020). State of the art and recent advancements in the modelling of land subsidence induced by groundwater withdrawal. *Water*, *12*(7). doi: 10.3390/w12072051

Haagenson, R., Rajaram, H., & Allen, J. (2020). A generalized poroelastic model using fenics with insights into the noordbergum effect. *Computers & Geosciences*, *135*, 104399. doi: 10.1016/j.cageo.2019.104399

Haghighi, M. H., & Motagh, M. (2019). Ground surface response to continuous compaction of aquifer system in Tehran, Iran: Results from a long-term multi-sensor

InSAR analysis. *Remote Sensing of Environment*, *221*, 534–550. doi: 10.1016/j.rse.2018.11.003

Hall, B. C. (2015). *Lie Groups, Lie Algebras, and Representations: An Elementary Introduction* (Vol. 222). Cham: Springer International Publishing. doi: 10.1007/978-3-319-13467-3

Harbaugh, A. W. (2005). *MODFLOW-2005 : the U.S. Geological Survey modular ground-water model–the ground-water flow process* (Report No. 6-A16). doi: 10.3133/tm6A16

Harbaugh, A. W., Banta, E. R., Hill, M. C., & McDonald, M. G. (2000). *MODFLOW-2000, The U.S. Geological Survey modular ground-water model: User guide to modularization concepts and the ground-water flow process* (Report No. 00-92). doi: 10.3133/ofr200092

Heilweil, V., Freethey, G. W., Wilkowske, C., Stolp, B. J., & Wilberg, D. E. (2000). *Geohydrology and numerical simulation of groundwater flow in the central Virgin River Basin of Iron and Washington Counties, Utah* (Other Government Series No. 116). Salt Lake City, UT: Utah Department of Natural Resources, Division of Water Rights. Retrieved from `http://pubs.er.usgs.gov/publication/70179116`

Heilweil, V. M., & Hsieh, P. A. (2006). Determining Anisotropic Transmissivity Using a Simplified Papadopulos Method. *Groundwater*, *44*(5), 749–753. doi: 10.1111/j.1745-6584.2006.00210.x

Helm, D. (1986). Compac: a field-tested model to simulate and predict subsidence due to fluid withdrawal. *Austral Geomechan Comput Newslett*, *10*, 18–20. Retrieved from `http://hdl.handle.net/102.100.100/272626?index=1`

Herod, M. (2013). *Reading: Porosity and Permeability | Geology.* Retrieved 2023-11-29, from `https://courses.lumenlearning.com/geo/chapter/reading-porosity-and-permeability/`

Herrera-García, G., Ezquerro, P., Tomás, R., Béjar-Pizarro, M., López-Vinielles, J., Rossi, M., ... Ye, S. (2021). Mapping the global threat of land subsidence. *Science*, *371*(6524), 34-36. doi: 10.1126/science.abb8549

Hesse, M. A., & Stadler, G. (2014). Joint inversion in coupled quasi-static poroelasticity. *Journal of Geophysical Research: Solid Earth*, *119*(2), 1425-1445. doi: 10.1002/2013JB010272

Hinnell, A. C., Ferré, T. P. A., Vrugt, J. A., Huisman, J. A., Moysey, S., Rings, J., & Kowalsky, M. B. (2010). Improved extraction of hydrologic information from geophysical data through coupled hydrogeophysical inversion. *Water Resources Research*, *46*(4). doi: 10.1029/2008WR007060

Hintze, L. (1980). *Geologic map of Utah: Utah Geological and Mineral Survey.* Retrieved 2023-05-05, from `https://mrdata.usgs.gov/geology/state/map-us.html`

Hoffman, M. D., & Gelman, A. (2014). The no-u-turn sampler: Adaptively setting path lengths in hamiltonian monte carlo. *Journal of Machine Learning Research*, *15*(47), 1593–1623. Retrieved from `http://jmlr.org/papers/v15/hoffman14a.html`

Hoffmann, J., Leake, S. A., Galloway, D. L., & Wilson, A. M. (2003). *MODFLOW-2000 ground-water model-user guide to the Subsidence and Aquifer-System Compaction (SUB) Package* (Tech. Rep. No. 2003-233). U.S. Geological Survey. doi: 10.3133/ofr03233

Hsieh, P. A. (1996). Deformation-Induced Changes in Hydraulic Head During Ground-Water Withdrawal. *Groundwater*, *34*(6), 1082–1089. doi: 10.1111/j.1745-6584.1996.tb02174.x

Hu, J., Li, Z. W., Ding, X. L., Zhu, J. J., Zhang, L., & Sun, Q. (2014, June). Resolving three-dimensional surface displacements from InSAR measurements: A review. *Earth-Science Reviews*, *133*, 1–17. doi: 10.1016/j.earscirev.2014.02.005

Hu, X., & Bürgmann, R. (2020, October). Aquifer deformation and active faulting in Salt Lake Valley, Utah, USA. *Earth and Planetary Science Letters*, *547*, 116471. doi: 10.1016/j.epsl.2020.116471

Hu, X., Lu, Z., & Wang, T. (2018). Characterization of Hydrogeological Properties in Salt Lake Valley, Utah, using InSAR. *Journal of Geophysical Research: Earth Surface*, *123*(6), 1257-1271. doi: 10.1029/2017JF004497

Huang, J., & Ghassemi, A. (2015). A poroelastic model for evolution of fractured reservoirs during gas production. *Journal of Petroleum Science and Engineering*, *135*, 626-644. doi: https://doi.org/10.1016/j.petrol.2015.10.007

Hughes, T. J. (2012). *The finite element method: Linear static and dynamic finite element analysis*. Dover Publications.

Hurlow, H. A. (1998). *The geology of the central Virgin River Basin, southwestern Utah, and its relation to ground-water conditions* (No. 26). Salt Lake City, UT: Utah Geological Survey, Utah Dept. of Natural Resources. (ISBN: 978-1-55791-614-3)

Iglesias, M. A., Lin, K., & Stuart, A. M. (2014, October). Well-posed bayesian geometric inverse problems arising in subsurface flow. *Inverse Problems*, *30*(11), 114001. doi: 10.1088/0266-5611/30/11/114001

Jaynes, E. T. (2003). *Probability theory: The logic of science*. Cambridge University Press. doi: 10.1017/CBO9780511790423

Karl Terzaghi, G. M., Ralph B. Peck. (1967). *Soil mechanics in engineering practice*. John Wiley & Sons, New York, NY.

Klenke, A. (2020). *Probability Theory: A Comprehensive Course*. Cham: Springer International Publishing. doi: 10.1007/978-3-030-56402-5

Kumar, R., Carroll, C., Hartikainen, A., & Martin, O. (2019). ArviZ a unified library for exploratory analysis of Bayesian models in Python. *Journal of Open Source Software*, *4*(33), 1143. doi: 10.21105/joss.01143

Langtangen, H. P., & Logg, A. (2016). *Solving PDEs in Python*. Springer International Publishing. doi: 10.1007/978-3-319-52462-7

Lark, R., Clifford, D., & Waters, C. (2014). Modelling complex geological circular data with the projected normal distribution and mixtures of von Mises distributions. *Solid Earth*, *5*(2), 631–639. doi: 10.5194/se-5-631-2014

Ley, C., & Verdebout, T. (2017). *Modern directional statistics*. Chapman and Hall/CRC. doi: 10.1201/9781315119472

Ley, C., & Verdebout, T. (2018). *Applied Directional Statistics: Modern Methods and Case Studies* (First ed.). New York: Chapman and Hall/CRC. doi: 10.1201/9781315228570

Li, S., Xu, W., & Li, Z. (2022). Review of the SBAS InSAR Time-series algorithms, applications, and challenges. *Geodesy and Geodynamics*, *13*(2), 114-126. doi: 10.1016/j.geog.2021.09.007

Lochbühler, T., Doetsch, J., Brauchler, R., & Linde, N. (2013, May). Structure-coupled joint inversion of geophysical and hydrological data. *GEOPHYSICS*, *78*(3), ID1–ID14. doi: 10.1190/geo2012-0460.1

Loope, D. B., Loope, G. R., Burberry, C. M., Rowe, C. M., & Bryant, G. C. (2020). Surficial fractures in the Navajo sandstone, south-western USA: the roles of thermal cycles, rainstorms, granular disintegration, and iterative cracking. *Earth Surface Processes and Landforms*, *45*(9), 2063–2077. doi: 10.1002/esp.4866

Manunta, M., De Luca, C., Zinno, I., Casu, F., Manzo, M., Bonano, M., ... Lanari, R. (2019). The parallel sbas approach for sentinel-1 interferometric wide swath deformation time-series generation: Algorithm description and products quality assessment. *IEEE Transactions on Geoscience and Remote Sensing*, *57*(9), 6259-6281. doi: 10.1109/TGRS.2019.2904912

Mao, W., Mu, X., Zheng, Y., & Yan, G. (2014, February). Leave-one-out cross-validation-based model selection for multi-input multi-output support vector machine. *Neural Computing and Applications*, *24*(2), 441–451. doi: 10.1007/s00521-012-1234-5

Mardia, K. V., & Jupp, P. E. (1999). *Directional Statistics*. John Wiley & Sons, Ltd. Retrieved 2024-12-12, from `https://onlinelibrary.wiley.com/doi/abs/10.1002/9780470316979.fmatter`

Marston, T. M., & Heilweil, V. M. (2012). *Numerical simulation of groundwater movement and managed aquifer recharge from Sand Hollow Reservoir, Hurricane Bench area, Washington County, Utah* (USGS Numbered Series No. 2012-5236). Reston, VA: U.S. Geological Survey. doi: 10.3133/sir20125236

Massonnet, D., & Feigl, K. L. (1998). Radar interferometry and its application to changes in the Earth's surface. *Reviews of Geophysics*, *36*(4), 441–500. doi: 10.1029/97RG03139

Mitusch, S. K., Funke, S. W., & Dokken, J. S. (2019, June). dolfin-adjoint 2018.1: automated adjoints for FEniCS and Firedrake. *Journal of Open Source Software*, *4*(38), 1292. doi: 10.21105/joss.01292

Molina, O., Vilarrasa, V., & Zeidouni, M. (2017, July). Geologic Carbon Storage for Shale Gas Recovery. *Energy Procedia*, *114*, 5748–5760. doi: 10.1016/j.egypro.2017.03.1713

Mulder, K., Jongsma, P., & Klugkist, I. (2020, June). Bayesian inference for mixtures of von Mises distributions using reversible jump MCMC sampler. *Journal of Statistical Computation and Simulation*, *90*(9), 1539–1556. doi: 10.1080/00949655.2020.1740997

Neal, R. M. (1996). Monte Carlo Implementation. In *Bayesian Learning for Neural Networks* (pp. 55–98). New York, NY: Springer. doi: 10.1007/978-1-4612-0745-0_3

Neal, R. M. (2012). *Bayesian learning for neural networks* (Vol. 118). Springer Science & Business Media. doi: 10.1007/978-1-4612-0745-0

Nixon-Hill, R. W., Shapero, D., Cotter, C. J., & Ham, D. A. (2024, July). Consistent point data assimilation in Firedrake and Icepack. *Geoscientific Model Development*, *17*(13), 5369–5386. doi: 10.5194/gmd-17-5369-2024

Oliver, D. S., Reynolds, A. C., & Liu, N. (2008). *Inverse theory for petroleum reservoir characterization and history matching.*

Osborne, P. S. (1993). *Suggested operating procedures for aquifer pumping tests. Ground water issue (15th in series)* (Tech. Rep.). Environmental Protection Agency, Ada, Oklahoma (United States). Robert S. Kerr Environmental Research Laboratory Ada, Oklahoma. Retrieved from `https://www.epa.gov/remedytech`

Papadopulos, I. S. (1965, August). Nonsteady flow to a well in an infinite anisotropic aquifer. In *Proceedings of the symposium on hydrology of fractured rocks.* Retrieved 2024-04-17, from `https://unesdoc.unesco.org/ark:/48223/pf0000141973`

Petra, N., Zhu, H., Stadler, G., Hughes, T. J., & Ghattas, O. (2012, September). An inexact Gauss–Newton method for inversion of basal sliding and rheology parameters in a nonlinear Stokes ice sheet model. *Journal of Glaciology*, *58*(211), 889–903. doi: 10.3189/2012JoG11J182

Pewsey, A., & García-Portugués, E. (2021, March). Recent advances in directional statistics. *TEST*, *30*(1), 1–58. doi: 10.1007/s11749-021-00759-x

Phan, D., Pradhan, N., & Jankowiak, M. (2019). Composable effects for flexible and accelerated probabilistic programming in numpyro. *arXiv preprint arXiv:1912.11554*.

Poland, J. F. (1984). *Guidebook to studies of land subsidence due to ground-water withdrawal.* Retrieved from `https://unesdoc.unesco.org/ark:/48223/pf0000065167`

Pollard, D. D., & Fletcher, R. C. (2005). *Fundamentals of Structural Geology.*

Qi, Y., Ju, Y., Yu, K., Meng, S., & Qiao, P. (2022, January). The effect of grain size, porosity and mineralogy on the compressive strength of tight sandstones: A case study from the eastern Ordos Basin, China. *Journal of Petroleum Science and Engineering*, *208*, 109461. doi: 10.1016/j.petrol.2021.109461

Quin, G., & Loreaux, P. (2013). Submillimeter accuracy of multipass corner reflector monitoring by ps technique. *IEEE transactions on geoscience and remote sensing*, *51*(3), 1775-1783. doi: 10.1109/TGRS.2012.2206600

Rad, N. N., Bekker, A., & Arashi, M. (2022, July). Enhancing wind direction prediction of South Africa wind energy hotspots with Bayesian mixture modeling. *Scientific Reports*, *12*(1), 11442. doi: 10.1038/s41598-022-14383-8

Rathgeber, F., Ham, D. A., Mitchell, L., Lange, M., Luporini, F., Mcrae, A. T. T., ... Kelly, P. H. J. (2016, December). Firedrake: Automating the Finite Element Method by Composing Abstractions. *ACM Transactions on Mathematical Software (TOMS)*, *43*(3), 24:1–24:27. doi: 10.1145/2998441

Raucoules, D., Bourgine, B., de Michele, M., Le Cozannet, G., Closset, L., Bremmer, C., ... Engdahl, M. (2009, July). Validation and intercomparison of Persistent Scatterers

Interferometry: PSIC4 project results. *Journal of Applied Geophysics*, *68*(3), 335–347. doi: 10.1016/j.jappgeo.2009.02.003

Reddy, J. (2019). *An introduction to the finite element method* (4th ed.). McGraw-Hill Education.

Ren, F., Ma, G., Fu, G., & Zhang, K. (2015). Investigation of the permeability anisotropy of 2d fractured rock masses. *Engineering Geology*, *196*, 171-182. doi: 10.1016/j.enggeo .2015.07.021

Riley, F. S. (1970). Analysis of borehole extensometer data from central california. *Land subsidence: proceedings of the Tokyo Symposium*, 423–431. Retrieved from `https://unesdoc.unesco.org/ark:/48223/pf0000014816`

Rønning, O., Ley, C., Mardia, K. V., & Hamelryck, T. (2021, September). Time-efficient Bayesian Inference for a (Skewed) Von Mises Distribution on the Torus in a Deep Probabilistic Programming Language. In *2021 IEEE International Conference on Multisensor Fusion and Integration for Intelligent Systems (MFI)* (pp. 1–8). Retrieved from `https://ieeexplore.ieee.org/abstract/document/9591184` doi: 10.1109/MFI52462.2021.9591184

Salehian Ghamsari, S., Dam, T. v., & Hale, J. S. (2025, June). Can the anisotropic hydraulic conductivity of an aquifer be determined using surface displacement data? A case study. *Applied Computing and Geosciences*, *26*, 100242. doi: 10.1016/j.acags .2025.100242

Salehian Ghamsari, S., & Hale, J. S. (2024). *Supplementary material for "a random model of hydraulic conductivity based on structural geological data".* doi: 10.5281/zenodo.14170026

Salehian Ghamsari, S., & Hale, J. S. (2025). *Supplementary material for "Can the anisotropic hydraulic conductivity of an aquifer be determined using surface displacement data? A case study".* doi: 10.5281/zenodo.10890121

Salehian Ghamsari, S., van Dam, T., & Hale, J. (2025). A random model of anisotropic hydraulic conductivity tailored to the InSAR-based analysis of aquifers. *University*

of Luxembourg. Retrieved 2025-07-23, from `https://orbilu.uni.lu/handle/10993/65440`

Sanderson, D. J., & Peacock, D. C. P. (2020, February). Making rose diagrams fit-for-purpose. *Earth-Science Reviews*, *201*, 103055. Retrieved 2024-12-12, from `https://www.sciencedirect.com/science/article/pii/S001282521930594X` doi: 10.1016/j.earscirev.2019.103055

Schwartzman, A. (2006). *Random ellipsoids and false discovery rates: Statistics for diffusion tensor imaging data* (Unpublished doctoral dissertation). Stanford University.

Shivanand, S. K., Rosić, B., & Matthies, H. G. (2024). Stochastic modelling of symmetric positive definite material tensors. *Journal of Computational Physics*, *505*, 112883. doi: 10.1016/j.jcp.2024.112883

Singh, A. (2014, November). Groundwater resources management through the applications of simulation modeling: A review. *Science of The Total Environment*, *499*, 414–423. doi: 10.1016/j.scitotenv.2014.05.048

Soize, C. (2000). A nonparametric model of random uncertainties for reduced matrix models in structural dynamics. *Probabilistic Engineering Mechanics*, *15*(3), 277-294. doi: 10.1016/S0266-8920(99)00028-4

Spiegelhalter, D. J., Best, N. G., Carlin, B. P., & Van Der Linde, A. (2002, October). Bayesian Measures of Model Complexity and Fit. *Journal of the Royal Statistical Society Series B: Statistical Methodology*, *64*(4), 583–639. doi: 10.1111/1467-9868.00353

Taghia, J., Ma, Z., & Leijon, A. (2014). Bayesian estimation of the von-mises fisher mixture model with variational inference. *IEEE Transactions on Pattern Analysis and Machine Intelligence*, *36*(9), 1701-1715. doi: 10.1109/TPAMI.2014.2306426

Tarantola, A. (2005). *Inverse Problem Theory and Methods for Model Parameter Estimation*. Society for Industrial and Applied Mathematics. doi: 10.1137/1.9780898717921

Teixeira Parente, M., Bittner, D., Mattis, S. A., Chiogna, G., & Wohlmuth, B. (2019, August). Bayesian calibration and sensitivity analysis for a karst aquifer model using active subspaces. *Water Resources Research*, *55*(8), 7086–7107. doi: 10.1029/2019wr024739

Terzaghi, K. (1925). *Erdbaumechanik auf bodenphysikalischer grundlage.* Leipzig: Deuticke. (In German)

Tomás, R., Romero, R., Mulas, J., Marturià, J. J., Mallorquí, J. J., Lopez-Sanchez, J. M., ... Blanco, P. (2014, January). Radar interferometry techniques for the study of ground subsidence phenomena: a review of practical issues through cases in Spain. *Environmental Earth Sciences*, *71*(1), 163–181. doi: 10.1007/s12665-013-2422-z

Torabi, A., Gabrielsen, R., Fossen, H., Ringrose, P., Skurtveit, E., Andò, E., ... Sokoutis, D. (2015, July). Strain localization in sandstone and its implications for CO2 storage. *First Break*, *33*, 81–92. doi: 10.3997/1365-2397.33.7.81788

U.S. Geological Survey. (2016). National Water Information System data available on the World Wide Web (USGS Water Data for the Nation) [Computer software manual]. Retrieved from `http://waterdata.usgs.gov/nwis/` (Accessed 31-05-2023)

van der Linde, A. (2005). DIC in variable selection. *Statistica Neerlandica*, *59*(1), 45-56. doi: 10.1111/j.1467-9574.2005.00278.x

Varrette, S., Cartiaux, H., Peter, S., Kieffer, E., Valette, T., & Olloh, A. (2022, October). Management of an Academic HPC & Research Computing Facility: The ULHPC Experience 2.0. In *Proceedings of the 2022 6th High Performance Computing and Cluster Technologies Conference* (pp. 14–24). New York, NY, USA: Association for Computing Machinery. doi: 10.1145/3560442.3560445

Vehtari, A., Gelman, A., & Gabry, J. (2017). Practical bayesian model evaluation using leave-one-out cross-validation and WAIC. *Statistics and computing*, *27*, 1413–1432. doi: 10.1007/s11222-016-9696-4

Vehtari, A., Simpson, D., Gelman, A., Yao, Y., & Gabry, J. (2015). Pareto smoothed importance sampling. *arXiv preprint arXiv:1507.02646*. (arXiv preprint arXiv:1507.02646)

Verruijt, A. (1969). Elastic Storage of Aquifers. In *Flow through Porous Media* (pp. 331–376). New York, NY, USA: Academic Press.

Walker, G., Wang, Q. J., Horne, A. C., Evans, R., & Richardson, S. (2020). Estimating groundwater-river connectivity factor for quantifying changes in irrigation return flows in the Murray–Darling Basin. *Australasian Journal of Water Resources*, *24*(2), 121-138. doi: 10.1080/13241583.2020.1787702

Watanabe, S. (2021). WAIC and WBIC for mixture models. *Behaviormetrika*, *48*(1), 5–21. doi: 10.1007/s41237-021-00133-z

Watanabe, S., & Opper, M. (2010). Asymptotic equivalence of bayes cross validation and widely applicable information criterion in singular learning theory. *Journal of machine learning research*, *11*(12). Retrieved from `https://www.jmlr.org/papers/volume11/watanabe10a/watanabe10a.pdf`

Zhang, J., Yang, Y., & Ding, J. (2023). Information criteria for model selection. *Wiley Interdisciplinary Reviews: Computational Statistics*, *15*(5), e1607. doi: 10.1002/wics.1607

Zhou, C., Gong, H., Zhang, Y., Warner, T. A., & Wang, C. (2018). Spatiotemporal Evolution of Land Subsidence in the Beijing Plain 2003–2015 Using Persistent Scatterer Interferometry (PSI) with Multi-Source SAR Data. *Remote Sensing*, *10*(4). doi: 10.3390/rs10040552

Zienkiewicz, O. C., Taylor, R. L., & Zhu, J. Z. (2005). *The finite element method: Its basis and fundamentals*. Elsevier. doi: 10.1016/C2009-0-24909-9